CHALMERS
UNIVERSITY OF TECHNOLOGY

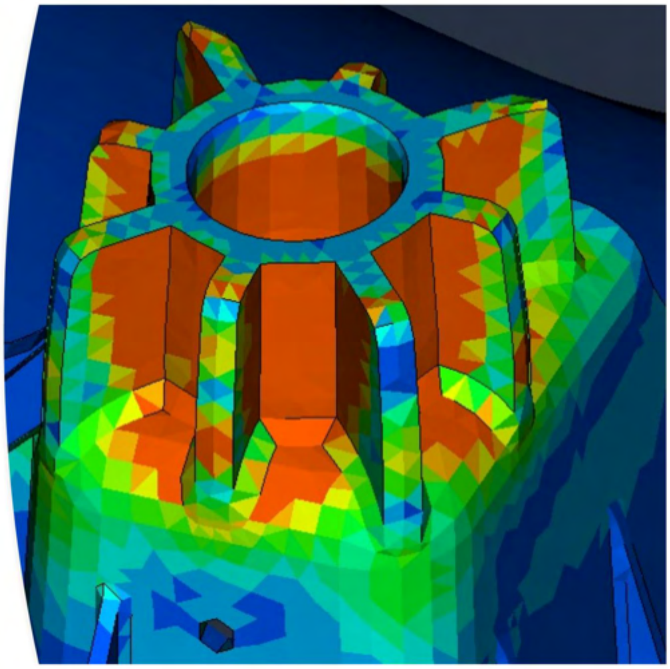

Bridging Design and Standardization: Structural Analysis and Optimization of Direct Screw Fastening in Automotive Thermoplastic Panels

Combining Optimization Framework Development, Finite Element Analysis, and Experimental Validation for Automotive Thermoplastic Joint Design

Master's thesis in Master Programme Mobility Engineering

Rishi Dineshwar & Modi El Masri

DEPARTMENT OF INDUSTRY AND MATERIALS SCIENCE
CHALMERS UNIVERSITY OF TECHNOLOGY
Gothenburg, Sweden 2026
www.chalmers.se

MASTER'S THESIS 2026

Bridging Design and Standardization: Structural Analysis and Optimization of Direct Screw Fastening in Automotive Thermoplastic Panels

Combining Optimization Framework Development, Finite Element Analysis, and Experimental Validation for Automotive Thermoplastic Joint Design

Rishi Dineshwar & Modi El Masri

DEPARTMENT OF INDUSTRY AND MATERIALS SCIENCE
CHALMERS UNIVERSITY OF TECHNOLOGY
Gothenburg, Sweden 2026

An Investigation of Viscoelastic Creep, Geometric Optimization, and Long-Term Durability in Insert-Free Thermoplastic Joints.
RISHI DINESHWAR & MODI EL MASRI

Supervisor: Zanko Azarniya, Volvo Cars AB
Examiner: Peter Hammersberg, Department of Industry and Material Science

Master's Thesis 2026
Department of Industry and Materials Science
Chalmers University of Technology
SE-412 96 Gothenburg
Telephone +46 31 772 1000

Cover: Finite element model of a screw-fastened thermoplastic doghouse interface.

Typeset in LaTeX
Printed by Chalmers Reproservice
Gothenburg, Sweden 2026

An Investigation of Viscoelastic Creep, Geometric Optimization, and Long-Term Durability in Insert-Free Thermoplastic Joints.
RISHI DINESHWAR & MODI EL MASRI
Department of Industry and Materials Science
Chalmers University of Technology

Abstract

The automotive industry aggressively pushes for lightweighting. This accelerates the transition toward direct screw fastening into thermoplastic components. The primary goal aims to eliminate heavy, costly metal compression limiters. Applying legacy metallic fastening standards to viscoelastic polymers introduces a critical engineering conflict. High assembly torques risk immediate localized yielding under the screw head. Overly conservative torques jeopardize long-term joint stability. This thesis investigates and optimizes the structural limits of insert-free thermoplastic joints within automotive A-pillar and IC-ramp assemblies developed in collaboration with Volvo Cars.

A fully integrated engineering workflow challenges existing conservative torque practices. The methodology synthesizes physical friction characterization, an evolutionary optimization framework, high-fidelity nonlinear finite element analysis (FEM), and destructive physical validation. The FEM incorporates 1000-hour viscoelastic creep. Feeding experimental friction data directly into the computational loop significantly enhances the predictive accuracy of the long-term structural models.

A unifying structural principle emerges across the computational optimization, virtual simulations, and physical testing. Contact geometry dictates joint survivability entirely more than bulk material stiffness. Captive washers fundamentally transform the mechanical load path. They reduce localized contact pressure and drastically increase ultimate torque capacity. This geometric optimization allows all evaluated thermoplastic joints to safely withstand the strict 10 Nm Volvo Cars internal standard without requiring metal inserts. Transitioning from elongated oval clearance holes to minimized, circular geometries proves critical. This maximizes continuous bearing area and actively prevents macroscopic deformation.

Significant variations in long-term durability exist across the tested material matrix. Rigid amorphous blends (PC-ABS) demonstrate excellent structural stability at ambient temperatures. They exhibit severe clamp load decay under elevated thermal conditions (60°C). Glass-fibre reinforced matrices (PP-GF) provide superior long-term preload retention. The internal glass fibers mechanically arrest viscoelastic flow. Unreinforced polypropylene (PP) exhibits critical sensitivity to massive creep and structural collapse across all configurations. The algorithmic DOE confirms that standard M5 fasteners lack sufficient bearing area for structural interior trim. This establishes M6 hardware as the absolute necessary baseline.

This research directly challenges internal company standards, exposing a broader disciplinary gap between complex polymer mechanics and rigid mechanical standardization. The absence of a shared technical language across engineering, standards, and production functions represents a systemic barrier, not unique to this case, that prevents evidence-based design rules from reaching the factory floor. By translating viscoelastic behaviour and algorithmic optimization into actionable design guidance, this work demonstrates how silo-breaking, cross-functional frameworks can bridge that gap, offering a replicable model for insert-free thermoplastic fastening beyond the automotive context studied here.

Keywords: Thermoplastic fastening, preload retention, viscoelastic creep, finite element analysis, structural optimization, genetic algorithms, Design of Experiments, surrogate modelling, automotive joints, contact mechanics.

Acknowledgements

We would first like to express our sincere gratitude to our supervisor at Volvo Cars, Zanko Azarniya, for his continuous support, technical expertise, and valuable guidance throughout this thesis project. His knowledge and engagement have been highly appreciated during the entire research process.

We would also like to thank Charlotta Källqvist, Kevin Ståhl, and Anders Enwall for their support and for making this thesis project possible. Their contributions, insights, and involvement have been greatly appreciated throughout the work.

We extend a special thanks to our examiner and supervisor at Chalmers University of Technology, Peter Hammersberg, for all valuable help, guidance, and academic support provided throughout the thesis.

Finally, we want to thank our families, friends, and all our supporters at Chalmers. Your continuous encouragement, patience, and motivation made this entire achievement possible.

Rishi Dineshwar and Modi El Masri, Gothenburg, June 2026

List of Acronyms

Below is the list of acronyms that have been used throughout this thesis listed in alphabetical order:

ABS	Acrylonitrile Butadiene Styrene
CAD	Computer-Aided Design
CNORMF	Average Contact Normal Force
CPRESS	Average Contact Pressure
DOE	Design of Experiments
FEA	Finite Element Analysis
FEM	Finite Element Method
GA	Genetic Algorithm
OLS	Ordinary Least Squares
PC-ABS	Polycarbonate/Acrylonitrile Butadiene Styrene
PP	Polypropylene
PP-GF	Glass-Fibre Reinforced Polypropylene
PP-T	Talc-filled Polypropylene
RMSE	Root Mean Square Error
RSM	Response Surface Methodology
SLS	Serviceability Limit State
SRC	Standardized Regression Coefficient
UCS	Ultimate Compressive Strength

Nomenclature

Below is the nomenclature of indices, sets, parameters, and variables that have been used throughout this thesis.

Indices

i, j, k	Indices for polynomial response surface variables and structural constraints
x, y, z	Indices for Cartesian coordinate directions
1, 2, 3	Indices for principal stress directions

Parameters

A	Cross-sectional area / Effective annular contact area / Material creep coefficient
D_i	Inner clearance hole diameter
D_o	External bearing (flange or washer) diameter
E	Young's modulus
G	Shear modulus
K_t	Theoretical stress concentration factor
L_0	Original length of the material element
P	Thread pitch
Q_c	Activation energy for creep
$\overline{R}$	Universal gas constant
T	Absolute temperature / Target tightening torque
T_g	Glass transition temperature
T_m	Melting temperature
X_c	Degree of crystallinity
a_0, a_i, a_{ij}	Polynomial response surface coefficients
d	Fastener diameter
d_2	Thread pitch diameter
h	Height of the material element
k_p	Penalty stiffness for contact formulation
m	Stress sensitivity exponent
n	Creep exponent / Time exponent
r_m	Mean bearing radius

x_L	Design variable boundaries
$\beta_0, \beta_i, \beta_{ii}, \beta_{ij}$	General quadratic response surface coefficients
ΔH_m	Measured heat of melting
ΔH_m°	Theoretical heat of melting for a 100% crystalline sample
$\dot{\epsilon}_0$	Material-specific creep rate constant
η	Fluid viscosity
μ_b	Bearing friction coefficient
μ_t, μ_g	Thread friction coefficient
σ_0	Material-specific stress constant / Initial stress immediately after tightening
σ_y	Uniaxial yield strength
τ_r	Relaxation time constant

Variables

C	Stress-dependent creep coefficient
F	Applied force
F_0	Initial clamp force (preload)
F_t, F_{1000h}	Retained clamping force over time / after 1000 hours
F_{ax}	Axial preload force
F_c	Contact force
M_b	Bearing torque
M_g	Thread torque
M_{tot}	Total applied torque
R	Long-term preload retention ratio
Y	Predicted engineering response (surrogate model)
$f(x)$	Objective function
$g_i(x)$	Structural constraint functions
x	Vector of design variables
x_p	Contact penetration distance
$\{F\}$	External force vector
$[K]$	Global stiffness matrix
$\{U\}$	Unknown nodal displacement vector
ϵ	Normal strain
$\dot{\epsilon}_{ss}$	Steady-state secondary creep rate
σ	Normal stress / Theoretical uniform contact stress
σ_{max}	Absolute peak stress
σ_{nom}	Nominal background stress
σ_r	Normalized stress ratio
σ_v	von Mises equivalent stress
$\sigma(t)$	Time-dependent stress decay
τ	Shear stress

Contents

List of Figures

List of Tables

1
Introduction

1.1 Background

The automotive industry is currently undergoing one of the most significant technological transitions in its history. Driven by electrification, sustainability targets, and increasing global competition, vehicle manufacturers are under constant pressure to reduce weight, lower production costs, and simplify manufacturing processes. For electric vehicles in particular, mass reduction directly contributes to improved energy efficiency, extended driving range, and reduced lifecycle emissions. As a result, lightweighting has become a central engineering objective throughout the automotive sector.

To achieve these targets, manufacturers are increasingly replacing traditional metallic components with lightweight polymer solutions. Thermoplastics such as polypropylene (PP), ABS, and PC-ABS have become dominant materials in modern vehicle interiors due to their low density, design flexibility, corrosion resistance, and ability to integrate multiple functions into a single component [1]. Beyond material substitution, plastics also enable part consolidation, reducing both manufacturing complexity and assembly operations.

As the use of thermoplastics continues to expand, attention is shifting towards the fastening systems used to assemble these components. While many interior trim components are manufactured entirely from plastic, the fastening interfaces often still rely on metallic reinforcement elements such as threaded inserts, compression limiters, or steel sleeves. These components increase weight, introduce additional manufacturing steps, and add cost to both suppliers and vehicle manufacturers [13, 14].

Consequently, there is growing industrial interest in direct screw fastening, where standard machine screws are tightened directly against the thermoplastic structure without metallic inserts. Eliminating these reinforcements offers attractive benefits in terms of reduced mass, lower material consumption, simplified assembly, and reduced production cost [14]. However, this shift introduces a fundamentally different engineering challenge.

Traditional fastening standards and design methodologies were largely developed for metallic structures, where materials exhibit high stiffness, predictable yielding behaviour, and minimal time-dependent deformation under normal service conditions [7, 16]. Thermoplastics behave differently. Their mechanical response is strongly influenced by temperature, time, stress level, and material architecture. Under sustained loading, polymers experience viscoelastic phenomena such as creep and stress relaxation, resulting in a gradual loss of clamp force over time [3, 1].

For this reason, the automotive industry has historically relied on metal inserts and compression limiters to protect thermoplastic components from excessive compressive stresses while ensuring long-term joint integrity. Although these solutions provide a robust and well-understood load path, they simultaneously reduce many of the lightweighting, cost, and manufacturing benefits that make thermoplastics attractive in the first place. As vehicle manufacturers continue to pursue lighter and more cost-efficient designs, understanding the true structural limits of insert-free thermoplastic fastening becomes increasingly important.

1.2 Problem Description

Volvo Cars is actively investigating opportunities to reduce weight, cost, and manufacturing complexity in future vehicle platforms. One potential solution is the elimination of metallic inserts and compression limiters from selected interior fastening applications. However, removing these reinforcements requires a deeper understanding of how thermoplastic joints behave during assembly and throughout their service life.

A particular challenge arises from the interaction between lightweight component design and existing corporate fastening standards. Volvo Cars maintains internal assembly standards that specify tightening torques for commonly used fasteners, including a recommended tightening torque of 10 Nm for both M5 and M6 screw joints. While these requirements have proven successful for insert-supported joints, their suitability for insert-free thermoplastic assemblies remains uncertain.

Applying the full standard torque may generate excessive local stresses beneath the screw head, resulting in permanent deformation or failure of the plastic structure during assembly. Conversely, reducing the torque may prevent immediate damage but can compromise long-term clamp force retention due to creep and stress relaxation. Determining the balance between assembly robustness and long-term durability therefore becomes a critical challenge.

The problem is further complicated by the fact that investigating insert-free fastening requires engineers to move beyond established design practices. Existing standards have largely been developed around proven concepts utilizing metallic inserts and standardized assembly torques. Removing the insert and evaluating lower torque levels therefore means deviating from solutions that have been validated over decades of vehicle development. As a result, engineers must operate in an area where validated data is limited and where decisions are often influenced by engineering judgement and differing opinions regarding acceptable risk.

This creates a natural tension between lightweighting ambitions and standardization requirements. Design engineers seek to reduce weight, cost, and manufacturing complexity, while standardization engineers are responsible for ensuring robust and repeatable solutions throughout the vehicle lifetime. Bridging this gap requires a scientific understanding of the structural limits of insert-free thermoplastic fastening.

The central question addressed in this thesis is therefore whether thermoplastic joints can safely withstand Volvo Cars' existing 10 Nm fastening requirement without metallic inserts. To answer this question, the influence of material selection, fastening geometry, preload level, temperature, and long-term viscoelastic behaviour must be systematically investigated. The ultimate objective is to provide the engineering foundation required to bridge the gap between practical lightweight component design and corporate fastening standardization.

1.3 Aim and Objectives

The primary aim of this thesis is to investigate the structural limits of direct screw fastening in automotive thermoplastic components. Through the evaluation of material behaviour, fastening geometry, and long-term preload retention, the research seeks to assess the feasibility of reducing or eliminating metal compression limiters in A-pillar and IC-ramp assemblies. Furthermore, the work aims to contribute to a common engineering foundation that supports informed decision-making between design engineers and standardization functions when evaluating insert-free fastening concepts.

Rather than simply mapping localized stress, the investigation focuses on the underlying mechanics governing preload retention and structural integrity. The specific objectives are to:

- Investigate the influence of interface geometry on the torque capacity and structural response of A-pillar and IC-ramp fastening interfaces, with particular emphasis on the role of bearing contact area.
- Evaluate the relationship between commonly used interior thermoplastics (PC-ABS, PP, and PP-GF) and their long-term resistance to creep, stress relaxation, and preload loss under elevated temperatures.
- Develop and validate a predictive structural modelling framework capable of estimating long-term preload retention and assessing the performance of alternative fastening configurations, including captive washer concepts.
- Establish a data-driven engineering framework that supports the evaluation of insert-free fastening solutions and facilitates alignment between component design requirements and corporate fastening standards.

1.4 Delimitations

The original project scope intended to capture a massive spectrum of fastening phenomena, dynamic loading conditions, and environmental evaluations. Strict project timeframes and available resources restricted the final execution to the absolute most critical static mechanical variables. The following intended investigations define the strict boundaries of the current study and transition directly into future work:

- **Expanded Application Areas:** The study successfully maps interior trim panels (A-pillar, C-pillar, and D-pillar). The scope entirely excludes exterior components, high-load structural chassis mountings, and crash-critical joints.
- **Alternative Fastening Concepts:** The mechanical evaluation locks exclusively onto direct screw fastening with standard M6 hardware. The scope explicitly excludes alternative joining concepts like snap-fits, structural adhesives, and thread-forming screws.
- **Dynamic and Fatigue Simulations:** The computational framework evaluates static viscoelastic creep across a strict 1000-hour duration. The scope excludes dynamic operating environments, continuous thermal cycling, and long-term fatigue loading.
- **Extended Physical Validation:** The current physical experiments map progressive torque-to-failure limits and short-term initial preload relaxation. The scope strictly excludes long-term physical durability testing. Future work must execute severe vibration testing to evaluate joint stability and structural degradation across varying assembly torque levels. Physical testing campaigns must also evaluate the assemblies under different extreme temperatures. Finally, physical test joints demand long-term environmental exposure followed by direct, physical measurement of both the residual tightening torque and the absolute retained clamping force.
- **Economic and Cost Analysis:** The current methodology evaluates materials and geometries strictly based on structural performance and preload retention. The scope completely excludes financial metrics. Factoring piece price, material volume, and hardware costs into the optimization equation changes everything. Quantifying the absolute cost savings of eliminating metallic inserts, or comparing inexpensive PP configurations against premium PC-ABS materials, remains a strict target for future financial integration.
- **Life Cycle Assessment (LCA):** The current study strictly evaluates structural and mechanical viability. The scope excludes a complete LCA. Quantifying the exact environmental impact and carbon reduction achieved by eliminating metallic compression limiters remains a critical target for future execution.

1.5 Thesis Outline

The thesis structure systematically answers the formulated research objectives:

- **Chapter 2: Theoretical Framework** establishes the underlying solid mechanics of bolted joints. It maps the viscoelastic properties of polymers, explicitly covering creep and relaxation. It defines the mathematical fundamentals driving optimization algorithms and finite element analysis.
- **Chapter 3: Methodology** details the integrated engineering workflow. It breaks down the experimental friction characterization and the algorithmic Design of Experiments (DOE). It outlines the exact setup of the dynamic Finite Element models and the physical test rig configurations.
- **Chapter 4: Results** delivers the empirical data extracted directly from the physical joint tests. It presents the quantitative stress, deformation, and long-term creep predictions generated by the numerical simulations.
- **Chapter 5: Discussion** interprets the raw findings. It compares the physical testing directly against the virtual models. It evaluates the structural importance of optimized contact geometry and discusses the long-term viability of insert-free joints.
- **Chapter 6: Conclusion and Future Work** summarizes the primary engineering discoveries. It presents engineering design recommendations and identifies opportunities for future research and development.

1.6 Confidentiality Statement

This Master's thesis operates in close collaboration with Volvo Cars. The automotive industry remains highly competitive. The research and development contained here relies heavily on proprietary data. A strict Non-Disclosure Agreement (NDA) legally bounds this entire document.

The public report intentionally omits or obfuscates specific technical, commercial, and strategic details. This complies directly with the active confidentiality requirements. The text conceals the exact strategic engineering and business motivations driving this research. The specific financial and architectural interests of Volvo Cars remain completely classified.

Classification protocols protect all precise proprietary intellectual property. Generic identifiers (e.g., PC-ABS 1, PP-GF 2, PP-T 1) replace exact material designations, supplier information, and chemical trade names throughout the text. The document heavily generalizes, crops, or excludes detailed CAD models. It hides the precise geometrical dimensions of the tested interior panels. It removes specific part numbers and internal corporate testing protocols entirely.

1.7 Ethics, Sustainability, and Code of Conduct

This thesis strictly adheres to the Volvo Cars Code of Conduct and the academic ethical guidelines of Chalmers University of Technology. All physical testing, data handling, and engineering evaluations followed established corporate and academic standards regarding ethics and environmental sustainability.

The core engineering objective directly supports large-scale automotive sustainability targets. Eliminating metallic compression limiters from thermoplastic assemblies completely removes a massive volume of high-density steel from the vehicle architecture. This absolute weight reduction lowers the global climate footprint of the active vehicle fleet. Transitioning to insert-free plastic joints also drastically improves end-of-life recycling efficiency. Shredding and processing pure polymer panels requires significantly less energy and logistical sorting when embedded steel inserts no longer contaminate the material stream.

1.7.1 Artificial Intelligence Usage

Artificial Intelligence (AI) tools supported the administration and drafting of this thesis report. AI models provided direct language correction and acted as an exploratory resource for brainstorming initial concepts and resolving general technical queries during the research phase.

Strict boundaries controlled this digital integration. AI did not generate the raw engineering data, physical test results, or the core computational methodology. All structural conclusions, finite element validations, and physical test interpretations were critically reviewed and verified by the authors, remaining our exclusive, original work.

2

Theory

This chapter establishes the theoretical foundation for direct screw fastening in thermoplastic components. The analysis heavily targets the exact relationship between material properties, joint mechanics, and the time-dependent effects controlling preload retention.

The text introduces fundamental concepts in solid mechanics first. It transitions into a review of polymer behavior, explicitly covering viscoelasticity, creep, and stress relaxation. It then maps bolted joint theory to explain load transfer and torque-preload dynamics before outlining numerical modeling through the finite element method.

2.1 Solid Mechanics

Stress and strain describe the mechanical behavior of materials under load. These quantities define exactly how internal forces develop and how materials deform. They form the absolute core basis for evaluating structural integrity.

2.1.1 Fundamental Concepts: Stress and Strain

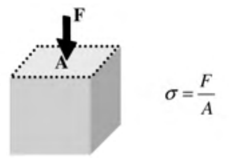

Figure 2.1: Definition of normal stress as force per unit area.

External forces strike a body. Internal forces develop to establish mechanical equilibrium and resist deformation (Figure 2.1). Engineers define the intensity of these resisting forces as stress. A force acting perpendicular to a surface creates normal stress. The constitutive relation defines this value mathematically [18, 4]:

$$\sigma = \frac{F}{A} \tag{2.1}$$

where:

- σ is the normal stress
- F is the applied force
- A is the cross-sectional area over which the force is distributed

Shear stress develops when the applied force acts parallel to a surface:

$$\tau = \frac{F_{shear}}{A} \tag{2.2}$$

where:

- τ is the shear stress
- F_{shear} is the tangential force acting along the surface

Strain describes the physical deformation resulting from applied stress. Normal strain defines the response for normal loading:

$$\varepsilon = \frac{\Delta L}{L_0} \tag{2.3}$$

where:
- ε is the normal strain
- ΔL is the change in length
- L_0 is the original length

Shear strain defines the response for shear deformation:

$$\gamma = \frac{\Delta x}{h} \tag{2.4}$$

where:
- γ is the shear strain
- Δx is the lateral displacement
- h is the height of the material element

Many engineering materials exhibit a linear relationship between stress and strain under small deformations. Hooke's law describes this behavior [21, 1]. For uniaxial loading:

$$\sigma = E\varepsilon \tag{2.5}$$

and for shear loading:

$$\tau = G\gamma \tag{2.6}$$

where:
- E is the Young's modulus
- G is the shear modulus

Basic engineering analysis relies heavily on these linear elastic relationships. Their applicability remains strictly limited to small deformations. They require materials with stable, time-independent behavior. Thermoplastic components exhibit intense viscoelastic and time-dependent responses. Engineers must account for massive deviations from linear elasticity.

2.1.2 Equivalent Stress and Yield Criteria

An increasing load pushes a ductile material toward its elastic limit. The yield strength (σ_y) defines this exact boundary. Permanent plastic deformation occurs immediately beyond this point.

Physical assemblies rarely experience simple uniaxial tension. The material beneath a fastener absorbs a complex multiaxial stress state. It sustains simultaneous compressive, radial, and circumferential stresses. The von Mises yield criterion predicts the exact onset of yielding under multiaxial loading [1, 4]. The equivalent stress (σ_v) calculates directly from the general Cauchy stress tensor components:

$$\sigma_v = \sqrt{\frac{1}{2}\left[(\sigma_x - \sigma_y)^2 + (\sigma_y - \sigma_z)^2 + (\sigma_z - \sigma_x)^2 + 6(\tau_{xy}^2 + \tau_{yz}^2 + \tau_{zx}^2)\right]} \tag{2.7}$$

where σ_x, σ_y, and σ_z are the normal stresses in the three Cartesian directions, and τ_{xy}, τ_{yz}, and τ_{zx} are the corresponding shear stresses. Alternatively, expressed in terms of the principal stresses ($\sigma_1, \sigma_2, \sigma_3$):

$$\sigma_v = \sqrt{\frac{1}{2}\left[(\sigma_1 - \sigma_2)^2 + (\sigma_2 - \sigma_3)^2 + (\sigma_3 - \sigma_1)^2\right]} \tag{2.8}$$

Yielding initiates when the equivalent stress (σ_v) breaches the material's uniaxial yield strength (σ_y) [1]. The von Mises criterion assumes the material remains perfectly isotropic. Its properties must remain identical in all directions. This holds true for metallic inserts. It acts as a strict mathematical simplification when analyzing composite polymers. Reinforcing fibers introduce distinct anisotropic behavior.

2.2 Polymer Mechanics

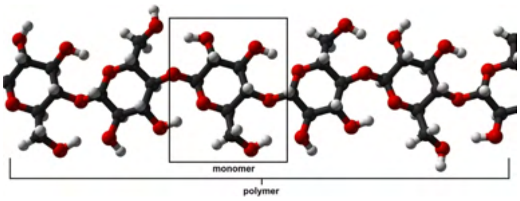

Figure 2.2: Schematic representation of polymer chains formed from monomers.

Thermoplastic polymers defy the linear elastic rules governing metals [1]. Molecular mechanics dictate their long-term failure mechanisms. Time, temperature, and environmental conditions strictly govern their structural response. Predicting failure in direct-screwed joints absolutely requires understanding this exact molecular architecture.

2.2.1 Molecular Architecture

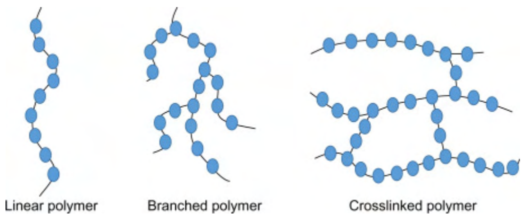

Figure 2.3: Different polymer chain architectures influencing molecular mobility.

Thermoplastics consist of long macromolecular chains. Strong covalent bonds connect these molecules internally. Much weaker intermolecular forces, like Van der Waals forces, govern the interactions between adjacent chains [1]. This architecture permits massive chain mobility under mechanical loading. The absolute degree of molecular entanglement dictates the material's stiffness. It explicitly controls the resistance to long-term deformation.

2.2.2 Thermal and Environmental Sensitivities

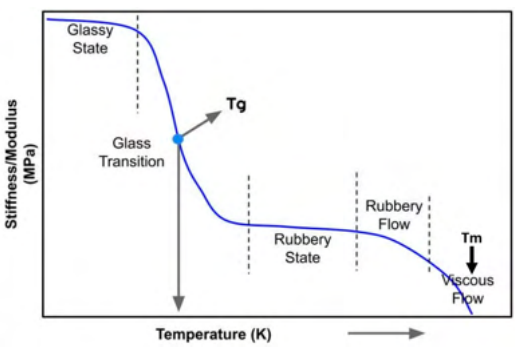

Figure 2.4: Typical relationship between glass transition (T_g), melting temperature (T_m), and specific volume in polymers.

Operating environments heavily manipulate polymer chain mobility. Temperature and humidity act as the primary drivers. The glass transition temperature (T_g) provides the critical thermal boundary. The amorphous regions of the polymer exist in a rigid, glassy state below T_g. The material transitions into a rubbery, highly compliant state above T_g. This causes a massive drop in mechanical stiffness. It violently accelerates creep behavior [1].

Moisture absorption acts as a powerful plasticizer in many polymers. Absorbed water molecules physically spread the polymer chains apart. This lowers the T_g and reduces the overall yield strength. Semi-crystalline polymers rely on highly ordered internal regions to mitigate these thermal sensitivities. The degree of crystallinity (X_c) provides massive additional stiffness. It calculates directly as [20]:

$$X_c = \frac{\Delta H_m}{\Delta H_m^\circ} \tag{2.9}$$

where ΔH_m is the measured heat of melting from the sample, and ΔH_m° is the theoretical heat of melting for a 100% crystalline sample of the exact same material.

2.2.3 Viscoelasticity Fundamentals

Figure 2.5: Classical spring-dashpot representation (Maxwell Model) of viscoelastic behavior.

Thermoplastic polymers exhibit intense viscoelasticity driven by chain mobility. Their mechanical response consists of an instantaneous elastic component combined with a time-dependent viscous component [22]. A Hookean spring ($\sigma = E\varepsilon$) approximates the elastic behavior. A Newtonian dashpot ($\sigma = \eta\frac{d\varepsilon}{dt}$) approximates the viscous flow [22]. Fluid viscosity maps to η. This fundamental viscoelasticity drives two critical physical phenomena in a bolted joint: creep and stress relaxation [3, 1].

2.2.4 Creep

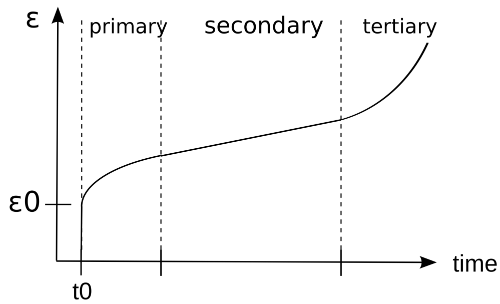

Figure 2.6: Typical creep curve illustrating primary, secondary (steady-state), and tertiary stages leading to failure.

Creep defines the progressive, continuous physical deformation of a material subjected to a constant applied stress [19]. A tightened screw exerts a constant compressive stress on the plastic. The entangled polymer chains gradually disentangle and slide past one another under this sustained load. The material physically flows outward, escaping the high-pressure zone entirely [3].

This deformation process occurs across three distinct stages [19]:

- **Primary Creep:** An initial period of rapid deformation. The rate gradually decreases as the polymer chains align and strain hardening activates.
- **Secondary (Steady-State) Creep:** A prolonged phase where deformation proceeds at a constant, highly predictable rate. This exact stage dominates the lifespan of the joint and dictates long-term preload loss.
- **Tertiary Creep:** A final phase characterized by rapidly accelerating deformation. It leads directly to macroscopic material rupture.

Engineering calculations focus entirely on the steady-state secondary creep rate ($\dot{\varepsilon}_{ss}$). This secondary stage dictates the total service life of the component. It models out through a power-law relationship combined directly with an Arrhenius temperature dependence [17, 1]:

$$\dot{\varepsilon}_{ss} = \dot{\varepsilon}_0 \left(\frac{\sigma}{\sigma_0}\right)^n \exp\left(-\frac{Q_c}{\bar{R}T}\right) \tag{2.10}$$

where $\dot{\varepsilon}_0$ and σ_0 are material-specific constants, σ is the applied equivalent stress, n is the creep exponent, Q_c is the activation energy, $\bar{R}$ is the universal gas constant, and T is the absolute temperature. High localized stress combined with elevated temperature will exponentially accelerate plastic deformation [17].

2.2.5 Stress Relaxation

Thermoplastic materials creep and deform. This physically reduces the clamped panel thickness. The tightened steel fastener acts as a stiff tension spring. The loss of clamped thickness forces the screw to contract. This contraction physically reduces the stretch in the steel. The joint transitions directly into a state of stress relaxation [14].

Stress relaxation defines the reduction in internal stress under a constant applied strain. A standard exponential decay model calculates this time-dependent stress decay ($\sigma(t)$) in a simplified linear viscoelastic material [1]:

$$\sigma(t) = \sigma_0 e^{-t/\tau_r} \tag{2.11}$$

where σ_0 is the initial stress immediately after tightening, t is the elapsed time, and τ_r is the specific relaxation time constant. Over months of service, this molecular relaxation destroys the axial clamping force. It compromises the absolute structural integrity of the assembly without any physical unthreading of the screw [3, 14].

2.2.6 Ductile vs. Brittle Behavior and Fiber Reinforcement

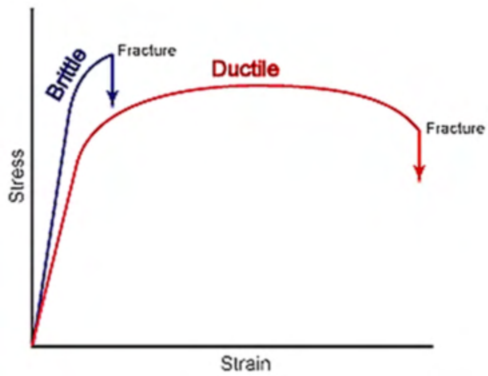

Figure 2.7: Typical stress-strain response contrasting ductile and brittle material behavior. The integral (area) under each curve represents the material's toughness, defining the total mechanical energy absorbed prior to fracture.

The macroscopic response of a polymer falls broadly into either ductile or brittle categories. The area under the stress-strain curve represents absolute toughness. This defines the total mechanical energy a material can absorb before catastrophic fracture [1].

PP materials are highly ductile. They yield and elongate massively before breaking. They absorb large amounts of energy. The polymer undergoes extensive plastic flow rather than sudden fracture in a screwed joint if localized stresses exceed the yield limit. This behavior prevents catastrophic cracking. The resulting deformation ruins dimensional stability and accelerates clamping force loss [1].

PP-GF materials exhibit a stiffer, highly brittle behavior. The elastic modulus spikes. This effectively retards creep, but the maximum strain-to-failure plummets [1]. The total energy the material can absorb before breaking decreases rapidly. PP-GF materials resist compressive embedding inside a screw boss. Their complete inability to yield makes them highly vulnerable to radial cracking when overloaded. The injection molding process aligns the internal glass fibers. This introduces severe structural anisotropy and makes the joint's mechanical properties completely direction-dependent [1].

2.2.7 Screw Boss Geometry

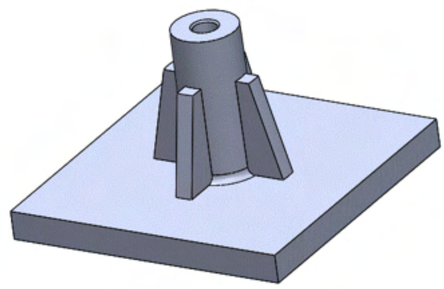

Figure 2.8: Standard geometric parameters of a thermoplastic screw boss designed for direct fastening.

The theoretical material mechanics play out directly within a molded feature known as a screw boss. A screw boss is a cylindrical protrusion designed specifically to receive the fastener. Critical geometric parameters define its performance. These include its outer diameter, inner pilot hole diameter, wall thickness, and the top contact area available to support the fastener head [14].

2.2.8 Implications for Fastened Joints

The boss geometry dictates exactly how the initial solid mechanics transition into long-term polymer degradation. The restricted contact area concentrates the massive compressive clamping force during initial tightening. This induces elevated equivalent stresses [12]. The radial stresses generated by the thread engagement will cause longitudinal cracking if the boss wall is insufficiently thick [14].

The localized stresses leave the material highly vulnerable to temperature-dependent creep and stress relaxation if the boss survives initial assembly. Successful direct-screwed thermoplastic joints demand a precise engineering balance. The design must apply classical solid mechanics to optimize the boss geometry. Engineers must calculate the exact torque required to generate sufficient initial clamping force. They must also ensure that the resulting contact pressure remains low enough to withstand the polymer's inherent long-term viscoelastic decay [12, 14].

2.3 Bolted Joint Theory

A mechanically fastened joint clamps components together. This ensures they act as a single, rigid structural unit under operational loads [4]. Applying a tightening torque to the fastener elastically stretches the steel screw. This generates a massive compressive clamping force, or preload, directly across the joint members. This preload remains highly stable in traditional metal joints. Thermoplastic joints break this rule entirely. The interaction between a stiff steel fastener and a time-dependent polymer matrix creates a highly volatile mechanical system [12, 1].

2.3.1 Torque-Preload Relationship

Tightening a threaded fastener generates an axial preload force (F_{ax}) to clamp the joint members. Only a minor fraction of the applied rotational torque actually stretches the screw. In a standard threaded joint, under-head friction dissipates approximately **50%** of the applied input energy. Thread friction consumes an additional **40%**. Only the remaining **10%** of the applied rotational torque actually translates into axial clamping force [12]. This heavy reliance on frictional energy dissipation makes accurate friction coefficients absolutely critical for calculating the final joint clamping force.

The total applied torque (M_{tot}) consists of a thread contribution (M_g) and a bearing friction contribution isolated under the screw head (M_b) [12, 4]:

$$M_{tot} = M_g + M_b \tag{2.12}$$

The thread torque (M_g) accounts for both the thread pitch geometry and the internal thread friction. It calculates as [12]:

$$M_g = F_{ax}\left(0.16P + 0.58\mu d_2\right) \tag{2.13}$$

The bearing torque (M_b) represents the friction between the underside of the screw head and the clamped material. It calculates as [12]:

$$M_b = F_{ax}\mu_b r_m \tag{2.14}$$

Substituting these individual components (Equation 2.13 and Equation 2.14) into Equation 2.12 establishes the standard engineering relationship for tightening an ISO metric thread [12, 4]:

$$M_{tot} = F_{ax}\left(0.16P + 0.58\mu d_2 + \mu_b r_m\right) \tag{2.15}$$

where P is the thread pitch, μ is the thread friction coefficient, d_2 is the pitch diameter, μ_b is the bearing friction coefficient, and r_m is the mean bearing radius. For an annular contact area, the mean radius calculates as [12]:

$$r_m = \frac{D_o + D_i}{4} \tag{2.16}$$

where D_o and D_i are the outer and inner diameters of the contact area, respectively.

Equation 2.15 relies entirely on severe fundamental assumptions. It presumes the joint members act as perfectly rigid bodies. It assumes uniformly distributed contact pressure. It treats the friction coefficients as absolute constants throughout the entire tightening process [12]. These assumptions work perfectly for rigid metallic joints. They represent a massive mathematical limitation when applied to thermoplastics. Polymers dynamically yield and deform during assembly [1].

2.3.2 Friction Under the Screw Head

Bearing friction under the screw head dominates the torque-preload relationship. This specific friction component accounts for roughly 50 percent of the total applied torque in practical assembly operations [12].

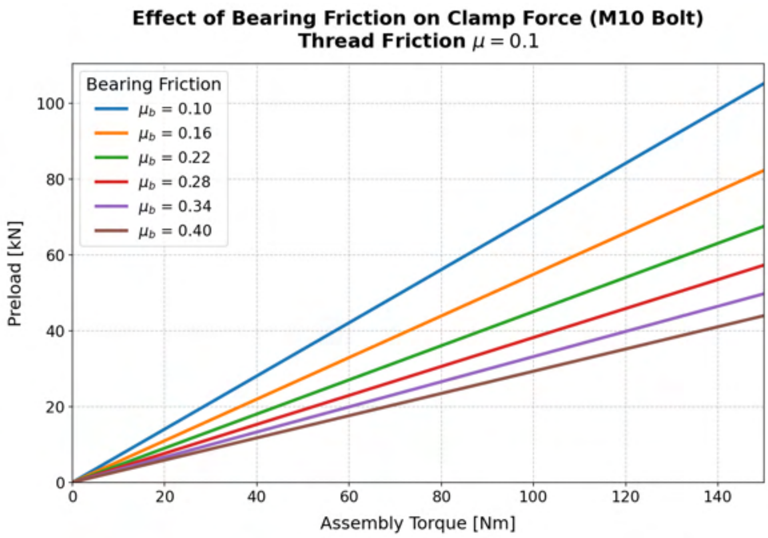

Figure 2.9: The effect of varying bearing friction coefficients (μ_b) on the generated clamping force for an M10 bolt at a constant thread friction ($\mu = 0.10$).

The gradient of the preload curve collapses as the bearing friction coefficient increases (Figure 2.9). A joint with high bearing friction demands a substantially larger assembly torque to achieve the exact same target clamping force [12]. This friction reacts violently to localized surface conditions. Macroscopic surface roughness, residual mold release agents, and local plastic yielding alter the true friction coefficient entirely [12, 4].

2.3.3 Assembly Variations

Transitioning from theoretical joint design to physical mass production introduces severe manufacturing variables. These variables directly threaten the structural integrity of the clamped plastic component. Automated assembly tooling is typically programmed to shut off upon reaching a predefined target tightening torque. This strictly assumes that a constant target torque always yields a constant axial clamping force [12].

Rearranging Equation 2.15 exposes the fatal flaw in this assumption. The achievable preload (F_{ax}) is inversely proportional to the friction coefficients. The automated tool measures rotational resistance rather than direct axial tension. Localized friction conditions on the assembly line entirely dictate the final clamping force [4]. Natural variations in surface friction regularly cause the true clamping force to fluctuate by ± 25 percent [12]. Automated tightening tools introduce their own mechanical and sensor tolerances. This adds another ± 15 percent variation to the applied torque. The total variation in the final clamping force easily reaches ± 30 percent under standard torque-controlled production tightening [12].

Joint design must completely account for this extreme production volatility. A $+30$ percent spike in clamping force generates heavy localized stress. This easily yields the polymer boss [4]. A -30 percent drop leaves the joint severely under-clamped from the very moment of assembly. This low initial load accelerates catastrophic joint failure driven entirely by long-term viscoelastic stress relaxation [12].

2.3.4 Compression Limiters

Thermoplastics exhibit terrible compressive strength compared to metals. They yield easily and relax constantly over time. Metallic inserts, commonly called compression limiters, mitigate this degradation while keeping the overall component lightweight [4]. Figure 2.10 shows a standard example. This specific figure illustrates a threaded insert. Simple unthreaded clearance sleeves are also widely deployed [12].

A compression limiter acts as a rigid metallic sleeve pressed directly into the thermoplastic component. Engineers design the length of this sleeve to be slightly shorter than the thickness of the surrounding plastic. The washer initially compresses the plastic as the screw tightens. The rigid washer eventually hits the top of the metal limiter once the plastic compresses past that small dimensional gap. This creates a massive physical stop [12].

Figure 2.10: Embedded metal compression limiter

The load path shifts instantly once this hard contact occurs. The strong metallic sleeve absorbs the absolute majority of the clamping force instead of the compliant thermoplastic matrix [4]. The metallic insert does not creep over time. It holds the target clamping force indefinitely. The surrounding plastic remains protected from high stress and stays safely trapped with a predetermined amount of compression.

2.4 Finite Element Method (FEM)

The Finite Element Method (FEM) provides a massive numerical technique for solving complex solid mechanics problems. It divides a continuous physical domain into a discrete mesh of geometric elements. Mathematical equations calculate the structural response at specific points known as nodes. This discretization transforms complex partial differential equations into solvable algebraic systems.

2.4.1 Element Formulation and Volumetric Locking

The specific choice of element formulation dictates the ultimate accuracy of a structural simulation. First-order linear elements often fail entirely under heavy plastic deformation. They exhibit a severe mathematical flaw known as volumetric locking. This locking occurs when the material behaves incompressibly during massive plastic yielding. The linear element becomes artificially stiff. It resists volume changes and generates highly inaccurate stress values.

Second-order quadratic elements resolve this excessive stiffness. A standard 10-node tetrahedral element uses a higher-order polynomial to capture complex bending and curved geometry. Standard quadratic elements still face severe contact stability issues during extreme localized deformation.

Modified 10-node tetrahedral solid elements (C3D10M) provide a strict mathematical solution to this problem. This specific formulation adjusts the internal integration scheme. It explicitly prevents volumetric locking during massive plastic embedding. These modified elements handle complex nonlinear contact interactions perfectly. They maintain robust convergence even when the thermoplastic matrix undergoes intense localized crushing directly beneath a fastener head.

2.4.2 Nonlinear Assembly Mechanics

Thermoplastic bolted joints operate entirely within the nonlinear domain. Linear FEA assumes small deformations and constant material stiffness. Thermoplastic assemblies violate both assumptions entirely. The solver must account for three distinct sources of physical nonlinearity.

Material nonlinearity captures the transition from elastic behaviour into plastic yielding and time-dependent viscoelastic creep. Geometric nonlinearity tracks large deformations as the physical shape of the plastic boss distorts under the massive clamping load. Contact nonlinearity updates the rapidly changing interaction surfaces as the fastener physically embeds into the plastic substrate.

2.4.3 Contact Mechanics and The Penalty Method

Numerical contact mechanics prevent structural bodies from passing through one another during a simulation. The solver mathematically enforces boundary conditions at the exact interfaces where components touch. Importing complete, fully detailed screw CAD geometries introduces severe geometric intersection errors. The complex helical threads create millions of microscopic contact interactions. These extreme geometric details destroy contact convergence. They drastically inflate computational time without improving the macroscopic preload accuracy.

Engineers replace these complex threads with simplified geometric representations to stabilize the mathematical model. The Penalty Method enforces the normal contact behaviour between these simplified surfaces. This method allows a microscopic amount of mathematical penetration (p) between the interacting bodies. It applies an opposing contact force (F_c) proportional to this penetration depth. It calculates this force through a predefined contact stiffness (k):

$$F_c = k \cdot p \tag{2.17}$$

This formulation acts as a stiff numerical spring. It forces the contact surfaces apart and maintains rigid physical boundaries. This approach bypasses the extreme computational cost of exact Lagrange multiplier enforcement. It permits minor reversible elastic slip long before macroscopic sliding occurs, securing total contact stability across the joint interface.

2.5 Structural Optimization and Surrogate Modelling

Finite Element Analysis (FEA) serves purely as an evaluative tool. It calculates the structural response of a predefined geometry. Improving a design using standalone FEA requires heavy iterative manual modification. This manual process runs computationally expensive and becomes highly inefficient for complex assemblies. Computational structural optimization automates this exact workflow. It couples mathematical search algorithms directly with analytical or numerical evaluation methods. This allows an engineer to systematically explore massive multi-variable design spaces. It locates high-performance configurations satisfying strict structural constraints [11].

Optimization operates as an absolute necessity for thermoplastic fastening systems. The initial preload generation, localized contact stress, friction, and long-term viscoelastic relaxation all interact in a highly nonlinear manner.

2.5.1 Analytical Contact Stress and Yield Criteria

Analytical stress estimations screen out structurally infeasible designs long before running high-fidelity nonlinear FEA. The standard torque-preload relationship (Equation 2.15) calculates the initial clamp force (F_{ax}) generated by the assembly torque [12]. This analytical approach estimates clamping forces across thousands of configurations in seconds. It bypasses the need for repeated, computationally heavy finite element evaluations entirely.

The generated clamp force converts directly into a localized interface stress (σ) beneath the fastener flange or washer.

$$\sigma = \frac{F_{ax}}{A} \tag{2.18}$$

where the effective annular contact area (A) calculates as:

$$A = \pi \left[\left(\frac{D_o}{2} \right)^2 - \left(\frac{D_i}{2} \right)^2 \right] \tag{2.19}$$

This simple geometric approach accounts for the specific external bearing diameters (D_o) and internal clearance holes (D_i) across every evaluated configuration [12].

Purely elastic metallic joints differ entirely from thermoplastic assemblies. Plastics exhibit localized embedding and micro-yielding right at the exact moment of initial tightening [1]. Enforcing a strict elastic limit ($\sigma \leq \sigma_y$) produces overly conservative design boundaries. Optimization frameworks for polymers rely heavily on a controlled plasticity allowance. Permitting an isolated stress exceedance (e.g., $\sigma \leq 1.25\sigma_y$) captures realistic physical seating behavior. It safely penalizes catastrophic punch-through failure modes.

2.5.2 Viscoelastic Creep and Preload Retention

The loss of clamping force over time drives massive failures in thermoplastic joints (Section 2.2.4). Empirical time-hardening formulations model this degradation analytically. This avoids the severe computational burden of full transient FEA [1].

The analytical stress converts into a normalized stress ratio (σ_r). This scales the varying material strengths against the applied loads:

$$\sigma_r = \frac{\sigma}{\sigma_y} \tag{2.20}$$

Viscoelastic decay rates react violently to this specific stress state. A stress-dependent creep coefficient (C) captures this behavior:

$$C = A\left(\sigma_r^{|m|}\right) \tag{2.21}$$

where A is the foundational material creep coefficient and m is the stress sensitivity exponent. Physical material testing defines both parameters [1].
A time-hardening formulation calculates the long-term preload retention ratio (R):

$$R = \exp\left(-C \cdot t^n\right) \tag{2.22}$$

Time (t) operates typically in hours, while n represents the material-specific time exponent. Multiplying the initial preload by this retention ratio determines the absolute retained clamping force at any future point in time (F_t):

$$F_t = F_0 \cdot R \tag{2.23}$$

This mathematical framework enables the optimization algorithm to work on two fronts at once. It evaluates the initial clamp force generation. It simultaneously checks the absolute structural stability of that clamp force over an extended service life.

2.5.3 Evolutionary Genetic Algorithms (GA)

A constrained engineering optimization problem follows a standard mathematical formulation [11]:

$$\begin{aligned} &\text{Minimize/Maximize} && f(x) \\ &\text{Subject to} && g_i(x) \le 0, \quad i = 1, 2, \ldots, m \\ &&& x_L \le x \le x_U \end{aligned} \tag{2.24}$$

The objective function maps to $f(x)$. Structural constraints map to $g_i(x)$. The design variables sit within the vector x, perfectly bounded by x_L and x_U.

Conventional gradient-based optimization applies derivative calculations to find the steepest path to a solution. These algorithms work exceptionally well for smooth, linear problems. They fail completely when applied to highly nonlinear systems like thermoplastic bolted joints. They easily become trapped in local optima.

Evolutionary Algorithms bypass this limitation. Genetic Algorithms (GAs) specifically provide a highly robust alternative [11]. GAs operate as stochastic, population-based search methods inspired directly by natural selection. The algorithm initializes a massive, diverse population of candidate designs instead of calculating analytical gradients. Biological operators act on this population over iterative generations:

- **Selection:** Configurations with the highest fitness values breed the next generation.
- **Crossover:** Design variables from the parent configurations recombine to produce new offspring.
- **Mutation:** Random perturbations inject into the population. This preserves genetic diversity and prevents premature convergence on local optima.

Penalty functions manage the strict structural constraints within the Genetic Algorithm. The penalty mathematically destroys the fitness score if a configuration violates a defined physical limit.

2.5.4 Design of Experiments (DOE) Generation

A Design of Experiments (DOE) establishes a rigid systematic mathematical framework. It identifies the direct relationship between input parameters and physical outputs. A DOE matrix essentially maps the hard boundaries of the entire design space [10].

Traditional DOE methods include full factorial or Latin Hypercube sampling. These approaches distribute sample points uniformly across the entire variable grid. Constrained structural problems break this approach entirely. Blind random sampling generates a massive percentage of physically impossible configurations.

An evolutionary DOE approach leverages the stored search history of the Genetic Algorithm instead. The algorithm evaluates thousands of configurations during an expanded run. Extracting the cumulative, structurally feasible designs builds a highly refined dataset. This evolutionary dataset avoids physically unrealistic combinations entirely. It provides a high-density mapping concentrated exactly on the high-performance design regions.

2.5.5 Polynomial Response Surface Modelling (RSM)

Evaluating thousands of joint configurations using high-fidelity simulations requires massive computational resources. Surrogate modelling bypasses this absolute computational bottleneck. A discrete DOE dataset trains a continuous analytical approximation. Engineers refer to this as a Response Surface Model (RSM) [10].

The second-order polynomial formulation represents a standard surrogate technique for mapping structural interactions [10]. It accurately captures nonlinear coupled effects. It safely avoids the severe overfitting risks linked directly to complex, higher-order mathematical models:

$$Y = \beta_0 + \sum_{i=1}^{k} \beta_i x_i + \sum_{i=1}^{k} \beta_{ii} x_i^2 + \sum_{i=1}^{k-1} \sum_{j=i+1}^{k} \beta_{ij} x_i x_j + \epsilon \tag{2.25}$$

The predicted engineering response equates to Y. The independent design variables map to x_i. The β terms define the exact linear, quadratic, and interaction coefficients. The approximation error remains entirely contained within ϵ.

Ordinary Least Squares (OLS) regression calculates the optimal coefficients [10]. This mathematical process minimizes the sum of squared residuals between the surrogate predictions and the raw DOE dataset. Statistical metrics confirm the absolute accuracy of the final model. The Coefficient of Determination (R^2) and Root Mean Square Error (RMSE) deliver the primary evaluation criteria.

2.6 Fastening Standardization and Design Philosophy

Both global automotive standards and Volvo Cars internal practices enforce strict regulations on threaded fasteners. Standard M5 and M6 Class 8.8 machine screws demand a 10 Nm assembly torque. This massive preload ensures the structural joint withstands intense dynamic operational forces and heavy vibrations without separating.

A fundamental design philosophy governs all automotive bolted joints: the clamped components must never fail before the fastener. If a critical overload occurs, the steel screw must yield and fracture before the surrounding material crushes. Global design standards, such as VDI 2230 [16], explicitly dictate that surface bearing pressures must never exceed the compressive yield strength of the clamped material. This rule exists specifically to prevent time-dependent material flow and subsequent preload loss. The design dictates that the joint must remain completely stable and intact throughout the entire life of the vehicle. Replacing a sheared standard M6 bolt is significantly cheaper and easier. Conversely, replacing a crushed, structurally compromised thermoplastic interior panel requires extensive labor and highly expensive replacement parts.

2.6.1 Polymer Viscoelasticity and the Metal Insert Bypass

Thermoplastics possess significantly lower compressive yield strengths than steel. Applying a 10 Nm torque directly to a bare plastic panel generates bearing stresses that instantly violate the VDI 2230 standard. Polymers are highly viscoelastic. When subjected to severe, sustained compression, the material physically flows away from the stress zone. This creep phenomenon causes immediate settlement and rapid preload decay. The joint eventually goes completely slack, leading to structural failure.

To solve this structural conflict, the automotive industry universally relies on metallic compression limiters [14]. These metal inserts act as an industrial cheat code. They absorb the heavy compressive clamp load and transfer the forces entirely metal-to-metal [13]. This effectively protects the weaker polymer matrix from overstressing and completely bypasses the complex reality of plastic creep. Standard engineering practice treats the metal insert as the only guaranteed method to survive a 10 Nm torque application.

2.6.2 The Knowledge Edge and Standard Deviation

Eliminating metallic limiters represents a radical shift in engineering practice. Removing metal inserts offers massive potential benefits, including cutting vehicle weight, reducing manufacturing costs, and drastically simplifying end-of-life recycling. However, executing this change requires a direct deviation from established corporate standards. Proposing this deviation inherently causes internal disagreements. Standardization boards mandate the continued use of metal limiters to guarantee joint safety and strictly resist insert-free applications.

This resistance exists because a massive knowledge gap remains. The scientific fact that polymers creep is well established. However, virtually zero validated engineering knowledge exists regarding how extreme 10 Nm torque levels combined with fluctuating vehicle temperatures accelerate plastic creeping in structural screw joints. Standard handbooks do not cover this precise condition. Existing published research strictly focuses on low-torque thread-forming screws or composite materials. Consequently, absolute guidelines for clamping bare structural thermoplastics with high-strength machine screws do not exist in the global manufacturing sector, and they do not exist internally at Volvo Cars.

This thesis operates exactly on this knowledge edge. The true gap in modern engineering is the absolute lack of predictive models for temperature-dependent, high-torque, insert-free thermoplastic joints in mass production. By mapping the exact viscoelastic decay under varying thermal and clamping conditions, this research directly confronts decades of conservative design rules. It replaces the reliance on metal inserts with an optimized, data-driven approach, providing the exact scientific proof required to safely manage standard deviations and align modern design potential with strict corporate safety requirements.

3
Methodology

This chapter presents the multi-scale methodology developed to evaluate, optimize, and validate direct screw-fastened thermoplastic joints. The workflow bridges industrial product development with high-fidelity engineering analysis. It contains four interconnected phases:

1. **Experimental Tribological Characterization:** Physical testing to establish true friction coefficients and initial relaxation behaviour.
2. **Computational Optimization and Surrogate Modelling:** A data-driven framework utilizing analytical models to rapidly screen fastening configurations and generate design boundaries.
3. **Nonlinear Finite Element Analysis (FEA):** High-fidelity simulations incorporating 1000-hour viscoelastic creep to evaluate long-term joint stability.
4. **Experimental Structural Validation:** Destructive physical testing on production components to correlate and validate the computational predictions.

Integrating experimentally validated friction data directly into the analytical equations and finite element contact definitions significantly improved the physical realism of the numerical models.

3.1 Fastener Selection

The internal standard engineering team at Volvo Cars guided the selection of fastening hardware. The standardization department established a strict criterion. All evaluated fasteners had to be existing, validated components currently active in vehicle production. They needed to be readily available within the corporate standard selection. This constraint guaranteed that any computational findings could map directly into future vehicle programs. It avoided the costly development of novel fastening hardware.

Three primary fastener configurations met these industrial requirements:

- **M5 Flange Screw:** A standard metric machine screw featuring an integrated solid flange.
- **M6 Flange Screw:** A larger standard metric machine screw featuring an integrated solid flange, intended for applications requiring higher initial clamping forces.
- **M6 Washer Screw:** A standard M6 machine screw equipped with a captive, freely rotatable washer. The captive washer design was specifically selected to decouple rotational bearing friction from the underlying thermoplastic substrate during the tightening process.

3.2 Materials

Nine thermoplastic material systems were investigated. These represent the primary polymer groups common in automotive interiors. A classified material naming system protects supplier confidentiality (Table 3.1). The engineering team at Volvo Cars provided all evaluated materials.

Table 3.1: List of investigated thermoplastic material systems.

Material Type	Classified Material Grade
PC-ABS	PC-ABS 1
PC-ABS	PC-ABS 2
ABS	ABS 1
ABS	ABS 2
PP-T	PP-T 1
PP-T	PP-T 2
PP-GF	PP-GF 1
PP-GF	PP-GF 2
PP-GF	PP-GF 3

3.3 Computational Optimization, DOE Development, and Surrogate Engineering Framework

A computational optimization and data-driven engineering framework was developed in Python [15]. This framework operated alongside the nonlinear finite element simulations and experimental validation procedures. It systematically evaluated how material selection, fastener geometry, friction behavior, and tightening torque influence structural integrity. It also mapped long-term preload retention in thermoplastic bolted joints.

The primary objective centered on establishing a generalized engineering methodology capable of rapidly exploring large multi-variable design spaces. Physical realism and structural feasibility had to be preserved. The developed workflow functioned as an intermediate engineering layer. It bridged simplified analytical modeling and high-fidelity nonlinear finite element analysis.

The computational methodology integrated experimentally validated friction data, analytical preload modeling, and viscoelastic creep prediction. It also incorporated evolutionary optimization, Design of Experiments (DOE) generation, polynomial surrogate modeling, and sensitivity analysis. This unified workflow enabled the rapid screening of fastening configurations before running expensive nonlinear simulations. It simultaneously improved the engineering understanding of the governing preload retention mechanisms.

The overall workflow implemented throughout the study is illustrated schematically in Figure 3.1.

Material Cards + Experimental Friction Measurements
↓
Analytical Clamp Force and Contact Stress Modelling
↓
Stress-Normalized Creep Retention Modelling
↓
Evolutionary Genetic Algorithm Optimization
↓
Large-Scale Evolutionary DOE Generation
↓
Polynomial Response Surface Development
↓
Sensitivity Analysis and Design Interpretation
↓
Selection of Configurations for Nonlinear FEA and Experimental Validation

Figure 3.1: Overview of the computational optimization and surrogate modelling framework developed throughout the study.

3.3.1 Engineering Database Development

A dedicated engineering database was established within the Python environment. This database contained the investigated thermoplastic materials, fastener geometries, assembly parameters, and experimentally obtained friction coefficients. It functioned as the foundational input structure for all subsequent optimization, DOE generation, and surrogate modeling activities.

The material library housed multiple automotive-grade thermoplastic systems, specifically the evaluated PC-ABS, ABS, PP-T, and PP-GF material grades [1]. Each entry contained the constitutive parameters required for instantaneous preload evaluation and long-term creep retention prediction. The specific parameters included yield stress, elastic modulus, time-hardening creep coefficients, stress sensitivity exponents, and long-term viscoelastic retention factors.

The creep-related coefficients were extracted directly from supplier material cards. These were experimentally calibrated where applicable to improve correlation with the observed mechanical behavior. The framework evaluated the initial preload capability of each material system. It also assessed the ability to maintain clamp force during long-term loading exposure.

A dedicated friction database was established in parallel using the experimentally measured tightening behavior obtained during the physical assembly testing. The screws evaluated in these physical tests did not feature washers. Separate friction definitions were implemented for thread friction behavior, bearing friction behavior, treated fastener conditions, and untreated fastener conditions.

Integrating experimentally obtained friction behavior directly into the computational framework improved the physical realism of the analytical preload predictions. Preload generation in bolted thermoplastic joints reacts heavily to the frictional interaction at both the thread and bearing interfaces. Capturing this physical data was essential.

3.3.2 Analytical Clamp Force and Interface Stress Modelling

A physics-based analytical preload generation model was implemented. This allowed the exploration of large fastening design spaces before running detailed nonlinear finite element analysis.

The initial clamp force (F_{ax}) generated by the applied tightening torque was calculated analytically. This required rearranging the standard torque-preload relationship established in Equation 2.15 (Section 2.3.1) [12]. This analytical model estimated the clamping force across thousands of fastening combinations in seconds. It bypassed the need for repeated nonlinear finite element evaluations.

The calculated clamp force was converted into localized interface stress (σ) beneath the fastener flange or washer-supported contact region. The theoretical contact stress formulation defined in Equation 2.18 processed this conversion. The effective annular contact area (A) was determined according to Equation 2.19. This geometric approach accounted for the specific external bearing diameters and internal clearance hole dimensions across every evaluated configuration.

Thermoplastic bolted joints behave differently than purely elastic metallic fastening systems. Plastics commonly exhibit localized embedding and seating deformation beneath the fastener interface during assembly [1]. A controlled plasticity allowance was incorporated into the optimization methodology to capture this physical assembly behavior. Enforcing a strictly elastic stress limit produces overly conservative boundaries. The framework instead permitted localized stress exceedance up to $\sigma \leq 1.25\sigma_y$, where σ_y represents the material yield stress. This specific allowance captured realistic thermoplastic interface behavior. It safely penalized structurally unrealistic punch-through failure modes during optimization.

A minimum assembly torque constraint of $T \geq 4.5$ Nm was enforced throughout the optimization process. This constraint maintained industrially representative assembly conditions consistent with standard automotive fastening practices.

3.3.3 Stress-Normalized Viscoelastic Creep Retention Modelling

Long-term preload degradation drives most failures in thermoplastic fastening systems [3]. A creep-based retention formulation was integrated directly into the computational optimization framework to capture this physical decay. The methodology applied time-hardening viscoelastic material behavior derived from supplier data. It paired this with stress-dependent retention modeling to estimate clamp force degradation during extended loading.

Simplified analytical stress estimations often create unrealistic scaling sensitivity. A stress-normalized creep formulation solved this issue. The normalized stress ratio (σ_r) was defined precisely as established in Equation 2.20.

The creep coefficient (C) was evaluated next according to Equation 2.21. This step required the foundational material creep coefficient (A) and the stress sensitivity exponent (m). A time-hardening formulation then calculated the long-term preload retention ratio (R) according to Equation 2.22.

The retained clamp force after long-term exposure (F_{1000h}) was calculated using Equation 2.23.

Integrating creep retention modeling directly into the optimization framework enabled a multidimensional analysis. Initial preload capability, long-term structural stability, material-dependent retention performance, and thermomechanical sensitivity were all evaluated simultaneously. This approach substantially improved the engineering relevance of the methodology. Fastening configurations were judged on their initial preload generation alongside their ability to preserve that preload during extended service exposure.

3.3.4 Evolutionary Genetic Algorithm Optimization

An evolutionary Genetic Algorithm (GA) optimization strategy explored the nonlinear and multi-variable fastening design space. This was implemented using the Pymoo optimization framework [11]. The theoretical foundation of this algorithm follows the biological principles outlined in Section 2.5.3.

The optimization simultaneously evaluated material selection, fastener diameter, flange or washer geometry, tightening torque, and friction condition. The GA methodology provided extreme robustness when handling interacting nonlinear variables alongside discrete and continuous design parameters. Thermoplastic fastening behavior is governed entirely by coupled interactions between preload generation, local interface stress development, and long-term viscoelastic relaxation. A standard linear solver would fail under these conditions.

Several distinct optimization objectives were established. These included the maximization of allowable tightening torque, the maximization of long-term clamp force retention, and a balanced optimization targeting both preload generation and creep resistance. The active optimization routine processed a population size of 120 individuals evolving over 150 generations.

Constraint handling procedures operated directly inside the optimization loop. Any configuration exceeding the allowable thermoplastic stress limits received a heavy mathematical penalty. The algorithm automatically removed these failing designs from the feasible search space during the evolutionary iterations.

The optimization framework revealed a severe structural limitation regarding the smaller M5 fastener geometry. It exhibited insufficient capability relative to the larger M6 configurations, failing heavily in preload generation and interface stress stability. This early numerical finding explicitly motivated the total exclusion of M5 configurations from the subsequent detailed nonlinear finite element investigations.

3.3.5 Evolutionary Design of Experiments Generation

A computational Design of Experiments (DOE) dataset mapped the structural design boundaries of the investigated fastening systems following the initial optimization (Section 2.5.4) [10]. Conventional uniformly distributed or purely stochastic sampling techniques were abandoned. The DOE dataset was instead constructed dynamically. It extracted the cumulative search history generated throughout a broadened evolutionary optimization process.

The expanded DOE generation processed a population size of 400 individuals over 40 generations. This evolutionary methodology provided severe advantages over conventional random sampling strategies. It produced a dense population of structurally feasible solutions. It increased the sampling resolution directly around high-performance design regions. Physically unrealistic fastening combinations were completely eliminated. Computational efficiency improved significantly.

The cumulative historical solution arrays underwent strict filtering. Duplicate configurations were removed. Stress-violating designs were rejected. Only structurally feasible solutions remained. The resulting DOE database represented a physically admissible engineering design space. This filtered dataset provided the exact foundation required for surrogate modelling, sensitivity analysis, and generalized engineering interpretation.

3.3.6 Polynomial Response Surface and Surrogate Modelling

A second-order polynomial response surface model provided a rapid engineering prediction capability for broad parametric investigations. This model was developed via Ordinary Least Squares (OLS) regression using the Scikit-Learn framework [10]. Section 2.5.5 details the theoretical basis for this analytical approach.

The generated DOE dataset trained continuous analytical response surfaces. These surfaces predict long-term clamp force retention strictly as a function of tightening torque, fastener diameter, contact geometry, and friction behaviour. A second-order polynomial formulation captured the highly nonlinear interaction effects between preload generation and interface geometry. This specific formulation avoided the severe overfitting risks commonly associated with complex, higher-order surrogate models.

The active response surface followed the general quadratic form established in Equation 2.25. The predicted engineering response is Y. The active coefficients represent the explicit nonlinear interaction contributions of all investigated design variables.

The developed surrogate models required strict validation after fitting the data. The coefficient of determination (R^2), residual analysis, Root Mean Square Error (RMSE), and parity plot comparisons confirmed the model accuracy. The surrogate predictions aligned strongly with the generated DOE dataset. This response surface methodology enabled near-instantaneous prediction of complex fastening behaviour. It completely bypassed the need for repeated nonlinear optimization or heavy finite element simulation.

3.3.7 Sensitivity Analysis and Engineering Interpretation

A dedicated sensitivity analysis framework quantified the exact influence of individual design variables on long-term clamp force retention behaviour [10]. This methodology combined standardized regression coefficient analysis with perturbation-based sensitivity evaluation. It also incorporated direct correlation assessment and response surface visualization.

All input variables were normalized using standard scaling procedures to extract absolute regression coefficients from the surrogate model. This standardization established a clear hierarchical ranking. It exposed the relative physical importance of every investigated design variable.

A perturbation-based sensitivity methodology isolated specific interactions. Each design variable was individually bumped by 10 percent relative to its baseline value. The downstream percentage impact on clamp force retention behaviour was then recorded. This step directly quantified the governing preload retention parameters and mapped specific structural robustness regions. It highlighted the exact variables most sensitive to manufacturing variation.

3.3.8 Integration with Nonlinear Finite Element Analysis and Experimental Validation

The computational optimization framework functioned exclusively as an integrated component of the overall multi-scale engineering workflow. It was never intended as a standalone design methodology. The initial optimization, DOE investigations, and surrogate modelling activities actively guided the selection of promising fastening configurations. These specific configurations then advanced to detailed nonlinear finite element simulations and physical destructive validation testing.

The experimentally measured tightening behaviour and friction coefficients fed directly back into the computational framework. This strict feedback loop anchored the numerical data to reality. It significantly improved both the physical realism and the predictive capability of the entire methodology.

3.4 Finite Element Modelling Methodology

The finite element methodology replicates the complex nonlinear assembly mechanics of direct screw-fastened thermoplastic joints. It captures both the immediate assembly loading and the long-term viscoelastic exposure.

The numerical workflow relied on CATIA V5 and ANSA for geometry preparation. ANSA handled pre-processing and solver deck generation. Abaqus/Standard executed the nonlinear implicit solution procedures. META processed the final assembly-level contact evaluation.

3.4.1 Geometry Preparation and CAD Simplification

All CAD geometry preparation and assembly modifications took place in Dassault Systèmes-V5. The models were then imported into the ANSA pre-processing environment. Volvo Cars supplied the baseline A-pillar and IC-ramp assemblies. These models underwent systematic simplification. This improved meshing quality, contact robustness, and overall computational efficiency. The critical structural load-transfer features remained perfectly intact.

Non-essential geometric details trigger unstable element distortion. Features like embossed markings, distant mounting points, and microscopic surface intersections were completely removed. The surrounding metallic chassis structures were converted into midsurface representations. This specific step slashed computational cost. It preserved structural compatibility while heavily reducing the total degrees of freedom.

Localized geometric modifications accurately reproduced the physical validation matrix. The A-pillar geometry was physically expanded. This ensured appropriate clearance for captive washer configurations. Evaluating the parametric M5 configurations required another adjustment. The nominal clearance hole diameters within both the thermoplastic panels and the supporting structure dropped from 8.0 mm down to 7.0 mm.

Representative M6 washer-supported and flange-supported interface geometries appear in Figure 3.2 and Figure 3.3.

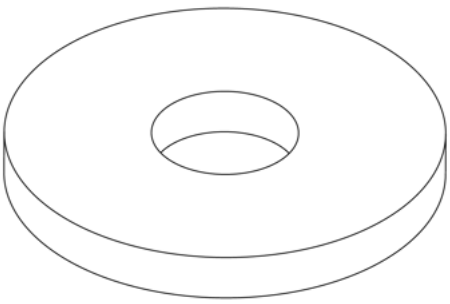

Figure 3.2: M6 washer-supported interface geometry.

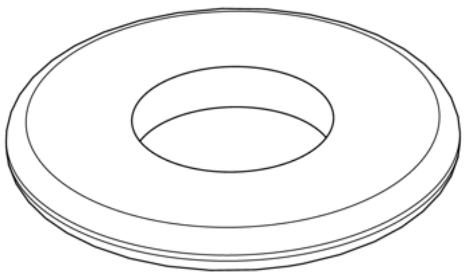

Figure 3.3: M6 flange-supported interface geometry.

Dedicated product assemblies were generated for every fastening configuration. This guaranteed strict consistency between the physical testing matrix and the numerical models. Additional parametric studies isolated the exact structural influence of oval versus circular clearance hole geometries.

3.4.2 Mesh Discretization Strategy

Second-order 10-node modified tetrahedral solid elements (C3D10M) discretized the thermoplastic components and metallic fastener interfaces. Section 2.4.1 previously outlined the theoretical basis for this choice. This modified higher-order formulation completely prevents volumetric locking. It drastically improves convergence robustness during localized compressive embedding.

A localized mesh refinement of 0.3 mm discretized the active bearing interfaces. This fine resolution captured the extreme stress gradients directly beneath the fastener head. A global target element length of 2.0 mm mapped the surrounding macroscopic structure. Strict limits controlled the mesh transition growth rate radiating outward from the fastener interfaces. This smooth physical transition stabilizes the nonlinear contact behaviour and prevents abrupt local stiffness spikes.

Reduced integration shell elements (S4R) mapped the surrounding metallic structures. This baseline mixed-dimensional mesh strategy remained completely locked across all simulations. This forced absolute, direct comparability between all tested configurations.

3.4.3 Material and Viscoelastic Modelling

Nine thermoplastic material systems were investigated. These included standard PC-ABS, ABS, PP-T, and PP-GF material grades. Supplier material cards provided the baseline definitions. Experimentally calibrated mechanical data from internal material databases refined these models.

Elastic-plastic behaviour models captured the permanent embedding directly beneath the fastener interface. Time-hardening viscoelastic creep formulations evaluated long-term structural durability. This numerical creep behaviour linked mathematically to the analytical retention framework developed in Section 2.5.2 (governed by Equation 2.22). This specific link enabled direct cross-validation between the surrogate predictions and the high-fidelity finite element simulations.

3.4.4 Contact Mechanics and Friction Formulation

Surface-to-surface contact formulations mapped all interacting interfaces. Metallic components acted as Master surfaces. The thermoplastic structures operated as Slave surfaces. This surface-to-surface methodology replaced conventional node-to-surface methods. It strictly prevents localized numerical stress spikes and forces smooth contact pressure continuity.

Finite sliding contact behaviour captured the localized relative motion during both preload application and extended creep exposure. The mathematical Penalty Method enforced all normal contact behaviour (Equation 2.17).

A Coulomb friction model with penalty-based linear enforcement defined the tangential behaviour. This approach permits minor reversible elastic slip long before macroscopic sliding occurs. It substantially improves convergence stability compared to strict Lagrange multiplier enforcement. The experimentally measured tightening tests supplied the exact friction coefficients applied here.

3.4.5 Fastener Representation and Preload Application

Only the physically relevant fastener contact regions survived within the ANSA environment. Importing complete, fully detailed screw CAD geometries introduces severe geometric intersection errors (Section 2.4.3). These errors destroy contact convergence.

The fasteners were represented solely by their flanged seating surfaces, washer contact interfaces, and simplified heads. They were modelled in strict M5 and M6 ISO metric sizes. The investigated concepts covered M6 flange-supported and M6 captive washer-supported systems. Initial optimization findings proved the M5 concepts lacked sufficient structural capability. The parametric M5 configurations were completely excluded from the detailed nonlinear creep investigations.

The target tightening torque converted mathematically into an equivalent physical preload. This calculation relied entirely on the experimentally calibrated torque-friction relationships established in Equation 2.15. The solver applied this exact load dynamically directly into the finite element model.

3.4.6 Boundary Conditions and Nonlinear Solution Strategy

Nonlinear implicit solution procedures executed the finite element analyses. Geometric nonlinearities remained active. This captured the heavily evolving contact conditions and large deformation behaviour.

Boundary conditions perfectly replicated the physical fixture setup from the experimental testing phase. The peripheral mounting interfaces were locked and fully constrained across all translational and rotational degrees of freedom ($U_x = U_y = U_z = UR_x = UR_y = UR_z = 0$).

The complete loading sequence executed in three distinct stages:
1. **Contact Stabilization Step:** A minor initial load eliminated rigid body motion and initialized the complex contact matrices.
2. **Preload Application Step:** The solver dynamically applied the fully calibrated preload.
3. **Viscoelastic Creep Exposure Step:** The fastener length locked mathematically at its deformed state. The thermoplastic matrix then relaxed under load for 1000 simulated hours.

3.4.7 Assembly-Level Retention Metrics

Average contact normal force (CNORMF) and average contact pressure (CPRESS) quantified the assembly-level preload preservation capability. The solver extracted these values directly from the active contact footprint beneath the fastener interface. Averaging these interface quantities over isolated nodal maxima eliminated mesh dependency. It blocked numerical singularities from skewing the physical results.

The retained clamp load and interface pressure metrics reflect simple percentages of their initial starting values. Post-processing explicitly evaluated these retention rates according to:

$$\text{Clamp Load Retention} = \frac{\text{CNORMF}_{1000h}}{\text{CNORMF}_0} \times 100 \tag{3.1}$$

$$\text{Contact Pressure Retention} = \frac{\text{CPRESS}_{1000h}}{\text{CPRESS}_0} \times 100 \tag{3.2}$$

3.4.8 Convergence Behaviour and Numerical Stability

The assemblies exhibit extreme nonlinear mechanical behaviour. Stabilization strategies were absolutely required to achieve a mathematical solution. These strategies included penalty-based friction, surface-to-surface discretization, controlled mesh transition refinement, and finite sliding tracking.

A large number of simulations evaluating thermoplastic systems at elevated temperatures failed to converge through the complete 1000-hour duration. These specific models used identical, previously validated procedures. This non-convergence represents a physically meaningful structural collapse driven by rapid viscoelastic softening. It is not a numerical failure.

3.5 Experimental Methodology

This section details the experimental methodology developed to characterize friction behaviour and structural failure in thermoplastic bolted joints [12].

Physical testing provided the realistic data needed to calibrate the computational models. This empirical baseline validated both the design optimization framework and the nonlinear finite element analyses. The campaign involved two complementary phases:
- Friction and initial preload relaxation characterization.
- Torque capacity and structural failure evaluation.

3.5.1 Test 1: Friction and Initial Viscoelastic Relaxation Characterization

The first phase quantified material-dependent friction behaviour and clamp force generation. It also captured immediate viscoelastic relaxation and measured the influence of fastener surface treatments. Preload generation reacts heavily to tribological interaction (Section 2.3.1). Obtaining true friction coefficients was absolutely necessary to establish physically representative analytical calculations and numerical contact definitions [12].

3.5.1.1 Specimen Preparation and Material Selection

Flat thermoplastic specimens isolated the material interaction behaviour from complex structural deformation effects. Standard pre-manufactured strips supplied the PP and ABS test samples. Equivalent standardized strips did not exist for the PC-ABS and PP-GF systems. Representative flat specimens were instead physically cut directly from low-curvature regions of molded production panels.

This approach preserved the actual surface textures and material processing effects generated during injection molding. A direct comparison between two extracted PP-T production strips evaluated how surface texture influences friction. One strip featured a smooth surface. The other featured a heavily molded, grained surface.

Testing evaluated an untreated M6 silver screw alongside a surface-treated M6 black screw. Neither fastener type used supplementary washers. This setup completely isolated the direct friction behaviour between the fastener head and the thermoplastic surface. Figure 3.4, Figure 3.5, and Figure 3.6 show representative examples of the prepared specimens and the test rig.

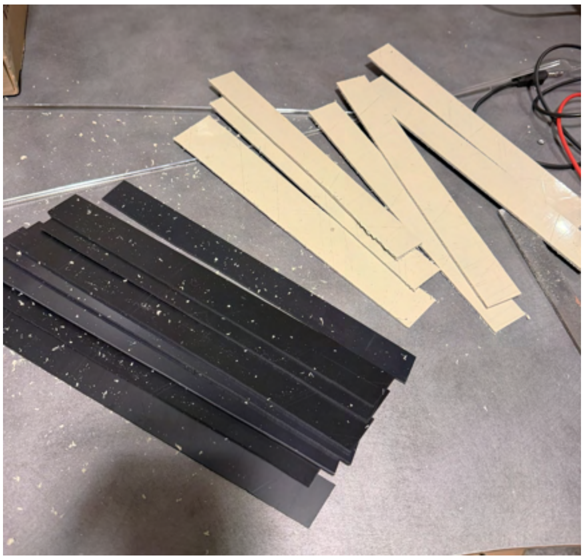

Figure 3.4: Standard ABS (left) and PP (right) thermoplastic strips prior to preparation.

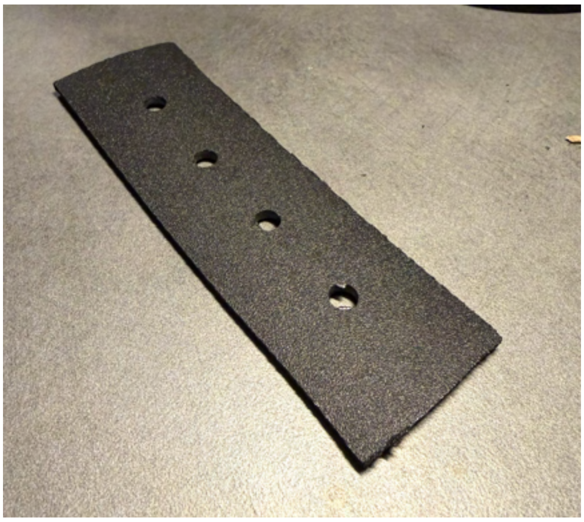

Figure 3.5: Grained PP production strip utilized for surface texture comparison.

Figure 3.6: Experimental rig utilized for friction and preload relaxation characterization.

The complete experimental matrix governing the friction characterization phase is summarized in Table 4.10.

Table 3.2: Experimental matrix for friction and initial preload relaxation characterization.

Test Number	Material System	Fastener Type
1	ABS (Generic Strip)	Treated Black Screw
2	ABS (Generic Strip)	Untreated Silver Screw
3	PP (Generic Strip)	Untreated Silver Screw
4	PC-ABS (Production Panel)	Untreated Silver Screw
5	PC-ABS (Production Panel)	Treated Black Screw
6	PP (Generic Strip)	Treated Black Screw
7	PP-GF (Production Panel)	Treated Black Screw
8	PP-GF (Production Panel)	Untreated Silver Screw
9	PP-T (Ungrained Production Panel)	Untreated Silver Screw
10	PP-T (Grained Production Panel)	Treated Black Screw

3.5.1.2 Experimental Procedure and Data Acquisition

A dedicated automated tightening rig executed all friction tests under controlled laboratory conditions. The testing procedure followed clearly defined steps to capture dynamic tightening data and static relaxation behaviour.

Each fastener was initially tightened to a strict 5.0 Nm target torque. An angle-controlled rotation of 720 degrees then established stable preload conditions. The test rig held the assembly locked in this position for exactly 60 seconds before unloading. This holding period captured the immediate viscoelastic stress relaxation occurring within the thermoplastic substrate.

Data extraction for the friction coefficients occurred at a clamp force corresponding to 75 percent of the proof load for M6 class 8.8 fasteners. This strictly followed ISO 16047 [8] and ISO 898-1 [9] standard procedures.

According to ISO 898-1, the stress area (A_s) for an M6 thread equals 20.11 mm^2. The proof stress (S_p) for a Class 8.8 fastener is 580 MPa. The nominal proof load (F_p) calculates directly as [9]:

$$F_p = S_p \cdot A_s = 580 \text{ MPa} \cdot 20 \text{ mm}^2 = 11660 \text{ N} \tag{3.3}$$

ISO 16047 mandates extracting the friction coefficients at 75 percent of this structural limit [8]. This establishes the exact target clamp force (F_{target}):

$$F_{target} = 0.75 \cdot F_p = 0.75 \cdot 11660 \text{ N} = 8750 \text{ N} \tag{3.4}$$

The test rig automatically decomposed the total tightening torque into separate physical contributions at this exact 8748 N threshold. These physical outputs matched the theoretical definitions of thread torque (M_g, Equation 2.13) and bearing torque (M_b, Equation 2.14) perfectly [12].

Measuring the physical contact region beneath the fastener head yielded an outer contact diameter (D_o) of 12.7 mm and an inner clearance diameter (D_i) of 6.7 mm. The analytical preload model required an effective mean bearing radius (r_m). These exact physical dimensions provided that value. Integrating this experimental friction and geometric data directly into the computational workflow anchored the finite element models to physical reality.

3.5.2 Test 2: Torque Capacity and Structural Failure Evaluation

The second phase evaluated the structural integrity and torque capacity of actual production components. This phase generated critical physical failure data. This data directly validates the predictive trends mapped by the optimization framework.

Testing evaluated between five and seven production components per configuration. Table 3.3 lists the specific parts alongside their assigned material grades.

Table 3.3: Production thermoplastic components evaluated during torque capacity and structural failure testing.

Descriptive ID	Classified Material
A-pillar 1	PC-ABS 3
Belt guide 1	ABS 1
A-pillar 2	PC-ABS 2
Belt guide 2	ABS 1
IC-ramp 1	PP-T 2
IC-ramp 2	PP-GF 1

3.5.2.1 Specimen Extraction and Fixture Development

The specific screw bosses were physically cut and extracted from the surrounding panel structures. This isolated the mechanical behaviour of the fastening interface while maintaining realistic local geometry. Figure 3.7 and Figure 3.8 illustrate this extraction. The process successfully preserved the local rib structures, boss reinforcements, and specific production molding features.

Custom steel fixtures represented an effectively rigid supporting structure. These fixtures incorporated welded M6 nuts to mimic the true production fastening interface. This perfectly matched the rigid boundary conditions enforced within the finite element simulations.

Figure 3.7: Intact A-Pillar panel prior to extraction of the fastening region.

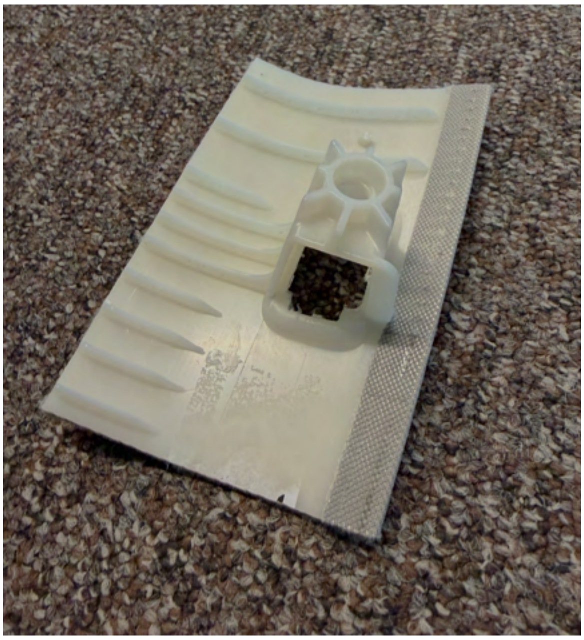

Figure 3.8: Isolated thermoplastic screw boss region utilized for structural testing.

3.5.2.2 Torque Capacity Testing Procedure

The extracted thermoplastic screw bosses were mounted to the custom steel fixtures using untreated M6 silver fasteners. The experiments directly compared different material grades, doghouse geometries (A-pillar versus IC-ramp), and fastener types. This generated a comprehensive, multi-variable dataset for computational validation.

A calibrated automated nutrunner tightened the fasteners (Figure 3.9). The equipment operated at rotational speeds exactly matched to the active production assembly conditions. Each specimen faced predefined target tightening torques ranging sequentially from 4.5 Nm up to 25 Nm.

Figure 3.9: Experimental torque capacity testing setup applying a calibrated automated nutrunner and rigid steel fixture system.

Loading the assemblies to these escalating torque levels systematically mapped the progression of macroscopic deformation and ultimate structural failure. A strict evaluation criterion governed this phase. The thermoplastic interface had to show absolutely zero visible macroscopic deformation to pass a specific torque level. Any physical yielding, permanent embedding, or structural damage observed upon disassembly constituted an absolute failure for that configuration.

The automated equipment recorded detailed torque versus time plots for each test cycle. These experimental deformation trends, failure mechanics, and torque profiles directly assessed the structural realism of the computational models. They provided the ultimate physical validation for the finite element simulations.

3.6 Internal Stakeholder Alignment and Problem Definition

Capturing the exact operational conflict between automotive design targets and established engineering standards required qualitative internal evaluations. Semi-structured discussions were executed with both the standard engineering department and the active interior design team.

Discussions with standard engineering provided the strict baseline requirements regarding production screws, captive washers, and the rigid mandate for metallic compression limiters in all plastic panels. Parallel discussions with the design team mapped the severe manufacturing and managerial constraints. Corporate management dictates strict cost reduction and enhanced recyclability targets, which directly demand the elimination of metallic inserts. Conversely, standard engineering enforces legacy safety rules that absolutely require those same inserts.

These cross-departmental evaluations identified the fundamental discrepancy. The legacy standard acts as a direct limiter to modern manufacturing goals. To validate the bridging of this gap, the methodology was structured specifically to generate the empirical data required. The intent was to physically demonstrate to standard engineering that a 10 Nm tightening torque is safely achievable without metal inserts, thereby forcing a data-driven dialogue between the two departments.

4

Results

This chapter presents the experimental data obtained from the physical testing phases, followed by the numerical results extracted from the Finite Element Analysis (FEA).

4.1 Computational Optimization and Surrogate Modelling Results

The computational framework established in this study rapidly evaluated thermoplastic fastening systems before detailed nonlinear finite element analysis. Integrating measured friction behaviour, analytical preload modelling, and creep estimation created a highly scalable methodology. This approach identified robust fastening configurations within a massive multidimensional design space.

The optimization process evaluated the combined influence of:

- Thermoplastic material selection
- Fastener diameter
- Washer-supported and flange-supported interfaces
- Tightening torque
- Experimentally measured friction conditions

Fastening performance depends entirely on the physical interaction between preload generation capability and localized contact stress distribution beneath the fastener interface.

4.1.1 Influence of Friction Behaviour

Friction behaviour between the fastener interfaces and the thermoplastic materials heavily influenced the optimization results.

Lower friction conditions directly generate much higher clamp forces at identical torque levels. This happens because reduced friction wastes far less energy during the tightening rotation. Treated fasteners naturally exhibited much higher preload efficiency than untreated interfaces.

Table 4.1 summarizes the experimentally measured friction coefficients applied throughout the computational framework.

Table 4.1: Experimentally measured friction coefficients implemented within the optimization framework.

Material Group	Condition	μ_b	μ_t
PC-ABS	Treated		0.11
PC-ABS	Untreated	0.21	0.11
ABS	Treated	0.13	0.10
ABS	Untreated	0.15	0.11
PP-T	Treated	0.19	0.09
PP-T	Untreated	0.19	0.10
PP-GF	Treated	0.18	0.11
PP-GF	Untreated	0.18	0.10

Experimentally derived friction data grounds the entire optimization framework in physical reality. It prevents the mathematical model from relying on idealized analytical assumptions. Experimental Test 1 provided these specific physical friction coefficients. The thread friction coefficients showed very little physical variation across all tests. An average value of $\mu_t = 0.11$ therefore drove the analytical preload modelling equations.

4.1.2 Optimization Results and Configuration Selection

The optimization framework evaluated physically feasible fastening combinations while strictly enforcing structural stress limits and long-term retention requirements.

The solver consistently converged toward washer-supported M6 fastening systems across the entire design space. These specific geometries distribute preload over a much larger effective bearing area. This drastically drops the localized contact stress beneath the fastener interface. It simultaneously permits much higher absolute clamp forces.

Table 4.2 summarizes the three highest-performing configurations identified by the genetic algorithm.

Table 4.2: Representative optimization results identified through the framework.

Objective	Material	Fastener	Cond.	Torque [Nm]	$\mathbf{F}_{init}$ [N]	Retention	$\mathbf{F}_{1000h}$ [N]
Max Torque	PC-ABS 2	M6 Washer	Treated	15.0	6010	0.94	5650
Balanced	ABS 2	M6 Washer	Treated	14.6	6800	0.99	6740
Least Creep	PP-GF 3	M6 Washer	Untred.	4.5	1830	0.99	1830

These selected configurations represent the absolute optimal balance between:
- High preload capability
- Acceptable localized contact stress
- Long-term clamp retention
- Structural feasibility under tightening

PP-GF and PP-T materials demonstrated exceptional retention values. However, their lower allowable tightening torque and reduced structural strength severely limited the maximum achievable clamp force. These highly compliant materials operate within a narrow, heavily restricted feasible design window.

The PC-ABS and ABS systems demonstrated superior structural robustness. They allow massive preload generation while remaining safely below the allowable stress constraints. These rigid systems maintain enormous retained clamp forces even after 1000 hours of simulated creep exposure.

4.1.3 Exclusion of M5 Configurations and Engineering Interpretation of Fastener Behaviour

Washer-supported M6 configurations provide the most mechanically robust fastening solution. The smaller M5 fastening systems exhibited severe structural limitations across the entire feasible design space.

Several interacting mechanical effects drive this improved M6 performance. First, the expanded bearing diameter of the washer distributes the preload across a massive contact area. This physical expansion directly reduces localized compressive stress. It lowers the risk of catastrophic material embedding and plastic deformation within the thermoplastic boss.

Second, the larger M6 fastener safely generates much higher preloads than the M5 configurations. This massive initial capacity improves total joint stability. It directly increases the absolute clamp force retained after long-term physical creep.

Third, the washer kills the stress concentration at the hole edge. This directly reduces creep-driven relaxation sensitivity within the polymer matrix. Fastening performance depends on an exact optimal balance between preload generation and stress distribution. It is never driven by preload magnitude alone.

The M5 configurations consistently exhibited:

- Lower achievable clamp force
- Higher localized contact stress
- Reduced structural robustness
- Increased sensitivity to creep-related preload loss

The small bearing area and limited preload capacity trapped the M5 systems in the absolute lowest-performance regions of the design space.

This optimization data justifies excluding the M5 concepts from all subsequent finite element simulations. Dropping these weak configurations drastically shrinks the computational design space. It forces the heavy nonlinear FEM investigations to focus exclusively on highly viable, mechanically robust fastening hardware.

4.1.4 Design Space Behaviour

The generated design space maps the exact physical relationships between tightening torque, clamp force capability, material strength, and long-term retention.

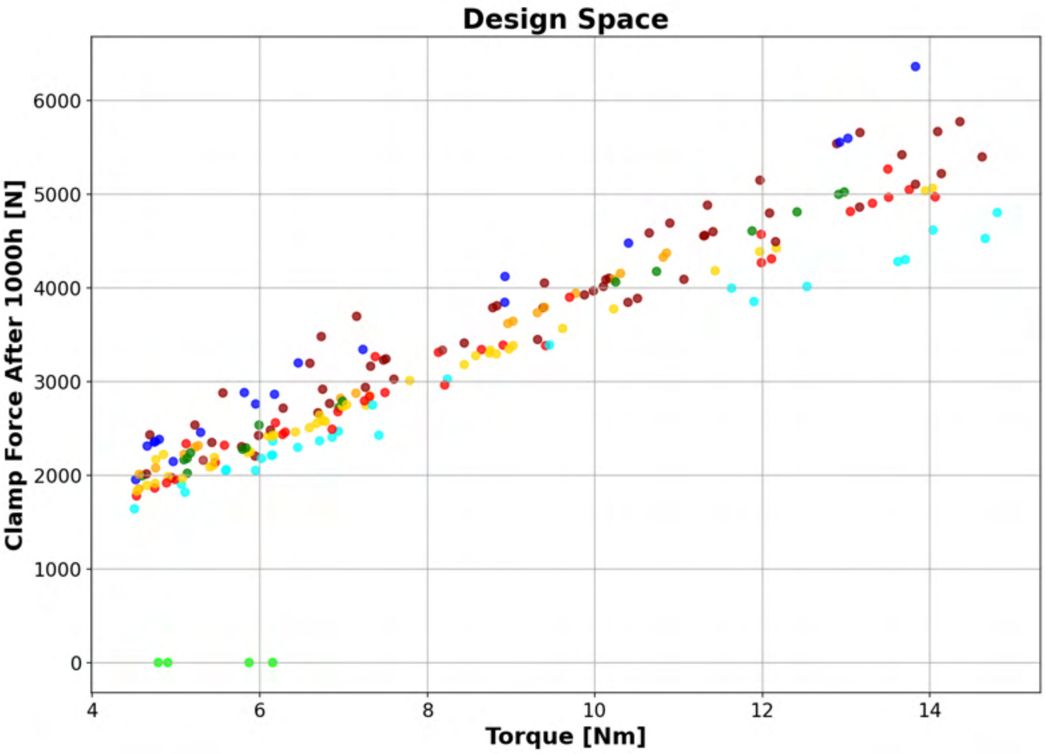

Figure 4.1: Optimization design space illustrating feasible fastening configurations.

Table 4.3: Colour representation used in the optimization design space plots.

Colour Tone	Material Category
Red tones	PC-ABS materials
Blue tones	ABS materials
Green tones	PP-T materials
Orange / Gold tones	PP-GF materials

Higher tightening torques generally increase the clamp force capability. The physical feasibility of any specific configuration depends entirely on the polymer's ability to withstand the resulting localized compressive stress.

Washer-supported M6 configurations consistently dominate the upper region of the feasible design space. They excel at stress distribution and provide unmatched structural robustness.

4.1.5 Retention Behaviour

Long-term clamp retention depends heavily on both the base material selection and the localized stress distribution.

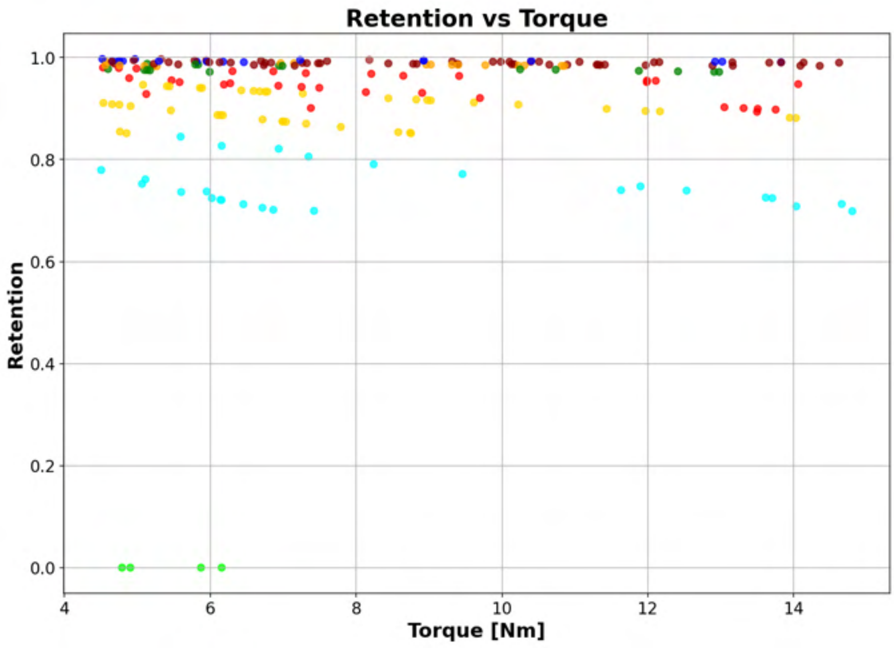

Figure 4.2: Retention versus tightening torque behaviour generated using the final optimization framework.

Several isolated configurations exhibit near-zero retention despite operating at relatively low tightening torques. These points most likely represent numerical outliers associated with thread stripping or sudden clamp force loss at torques below approximately 6.0 Nm. In these cases, the optimizer appears to have selected geometries where the fastener interface experiences catastrophic local failure rather than gradual viscoelastic preload decay. Such behaviour represents a known edge case within discrete design spaces and highlights the importance of satisfying both retention and structural integrity constraints simultaneously.

Elevated tightening torques increase initial preload capability. They simultaneously spike the localized stress directly beneath the fastener interface. This sharp stress spike rapidly accelerates creep sensitivity within the thermoplastic matrix.

PC-ABS systems deliver the highest overall performance. They combine massive initial preload generation with stable, highly reliable retention behaviour. PP-T and PP-GF systems only maintain high retention ratios because their weak structural limits force them to operate at very low absolute preload levels.

4.1.6 DOE Generation and Surrogate Model Development

A computational DOE framework generated a massive continuous engineering dataset for surrogate model development immediately after the optimization stage.

The initial optimization stage identified single best-case configurations. The DOE framework systematically mapped thousands of physically feasible fastening combinations across continuous parameter boundaries instead.

The DOE framework sampled combinations of:
- Tightening torque
- Bolt diameter

- Flange diameter
- Material selection
- Friction condition

This massive mapping algorithm applied the exact same physics-based preload and creep relationships established during optimization.

Applying the strict structural feasibility constraints filtered the generated database. The final DOE generation process produced exactly 7447 valid fastening configurations.

This massive output established a highly refined, physics-informed engineering database. It is perfectly suited for surrogate modelling and advanced sensitivity analysis.

4.1.7 Polynomial Response Surface Results

The DOE dataset trained multiple second-order polynomial response surface models. These surrogate models rapidly predict long-term clamp force behaviour. They transform the computationally heavy optimization workflow into a single simplified analytical equation. This specific math enables near-instantaneous engineering prediction.

The developed polynomial model followed the general form:

$$Y = a_0 + a_1 x_1 + a_2 x_2 + a_3 x_3 + a_{11} x_1^2 + a_{12} x_1 x_2 + \dots \tag{4.1}$$

where the independent variables represented tightening torque, bolt diameter, and flange diameter.

The final response surface model demonstrated highly accurate predictive capability:

$$R^2 = 0.9437 \tag{4.2}$$

and:

$$RMSE = 260 \text{ N} \tag{4.3}$$

The calculated RMSE remains very small compared to the absolute clamp force range. This metric confirms strong, reliable agreement between the surrogate model predictions and the raw DOE dataset.

The final polynomial response surface equation obtained from the DOE dataset was:

$$\begin{aligned} F_{1000h} &= 20800 + 700T - 9730d + 660D_o \\ &+ 21T^2 - 150Td + 7TD_o \\ &+ 970d^2 - 2D_o - 20D_o^2 \end{aligned} \tag{4.4}$$

where T represents tightening torque, d represents bolt diameter, and D_o represents flange diameter.

The response surface equation proves mathematically that tightening torque directly drives retained clamp force. The specific interaction terms expose the heavily coupled relationship between fastener diameter, contact geometry, and preload generation. Negative interaction terms absolutely dominate the bolt diameter variable. Simply increasing the fastener diameter fails to improve the retained clamp force. A larger bolt requires a simultaneous expansion of the contact area to safely redistribute the massive preload. This mathematical relationship completely reinforces the absolute structural necessity of washer-supported fastening geometries.

4.1.8 Response Surface Behaviour

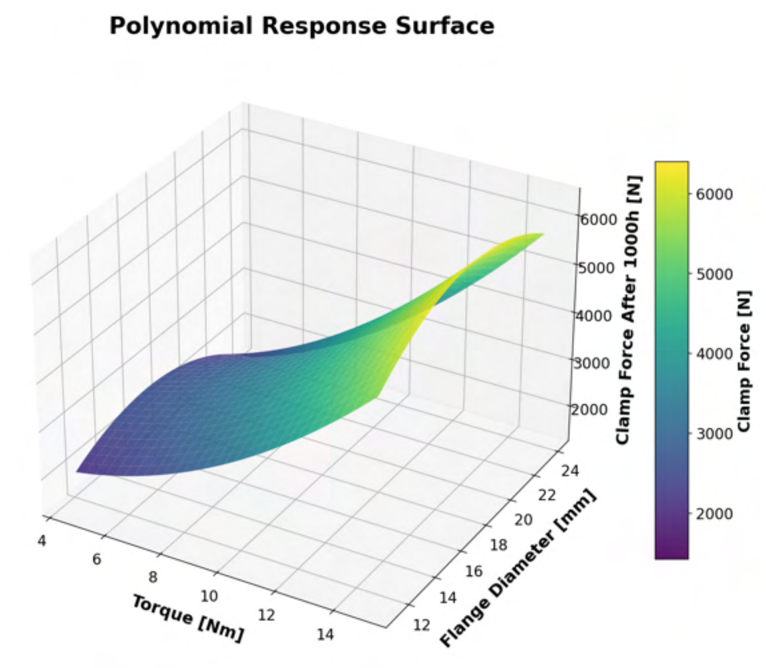

Figure 4.3: Polynomial response surface illustrating the combined influence of tightening torque and flange diameter on long-term clamp force behaviour.

Increasing the tightening torque massively improves clamp force capability. Expanding the flange diameter actively fights the resulting stress spike. The wider flange distributes the heavy preload over a much larger effective contact area. Pushing high torque through a small flange diameter triggers immediate failure. The localized stress concentrations under the fastener head rapidly exceed the structural limits of the plastic. Larger flange interfaces solve this bottleneck entirely. They safely absorb enormous preload levels while maintaining stable, acceptable stress states within the thermoplastic matrix.

The visual response surfaces confirm the absolute structural superiority of washer-supported systems. They perfectly illustrate the heavily coupled physics linking preload generation directly to stress redistribution.

4.1.9 Parity Plot Validation

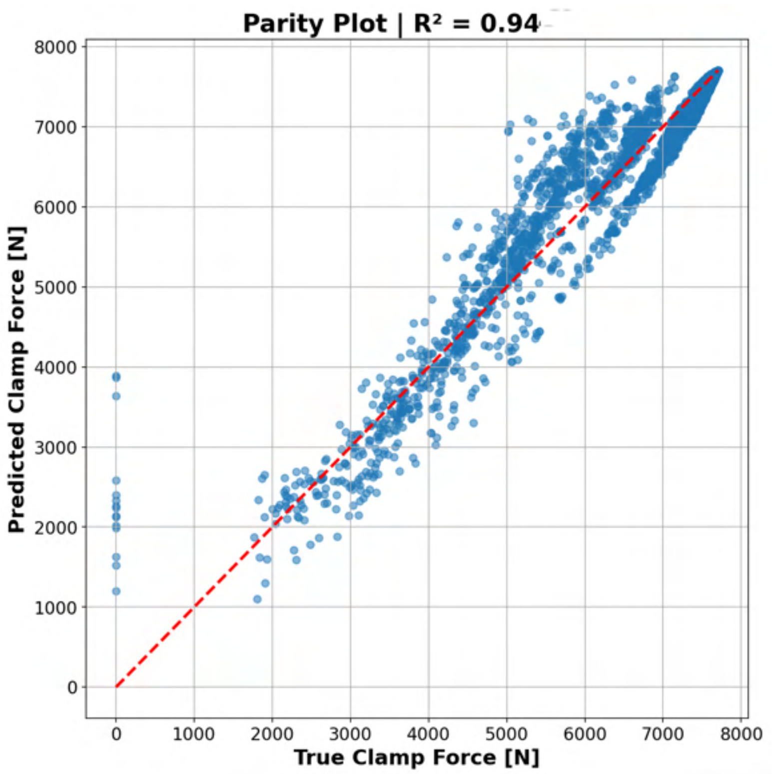

Figure 4.4: Parity plot comparing polynomial response surface predictions against the original DOE dataset results.

The parity plots verify strict agreement between the polynomial response surface predictions and the raw physics-based DOE dataset.

Nearly all prediction points cluster tightly along the ideal correlation line. The surrogate model successfully captures the complex structural physics governing thermoplastic fastening behaviour.

Minor deviations appear at the extreme upper clamp force limits. These originate from highly volatile nonlinear interactions between heavy tightening torques, contact geometry, and rapid creep retention decay.

The established accuracy validates the response surface model entirely. It provides a reliable, high-speed engineering prediction tool perfectly suited for comparative design assessments.

4.1.10 Sensitivity Analysis Results

A sensitivity analysis isolated the exact parameters governing long-term clamp force behaviour.

This analysis applied two distinct methodologies:

- Standardized polynomial coefficient analysis
- Perturbation sensitivity analysis

Table 4.4 summarizes the final influence rankings.

Table 4.4: Sensitivity ranking obtained from the polynomial response surface model.

Feature	Coefficient	Relative Influence [%]
Torque_Nm	1060	60
Bolt_d_mm	-440	25
Flange_Do_mm	-56	3
Bolt_d_mm^2	50	3
Torque_Nm × Bolt_d_mm	-50	3
Torque_Nm^2	50	3
Flange_Do_mm^2	-30	2
Torque_Nm × Flange_Do_mm	13	1

Tightening torque dictates the entire system. It governs exactly 60.7% of the total response surface behaviour.

Bolt diameter ranks second. It directly controls both the maximum preload generation capacity and the resulting localized contact stress.

Flange diameter registers a much smaller direct numerical contribution. However, its physical interaction with the tightening torque saves the joint from failure. The flange radically drops the localized compressive stress beneath the fastener interface.

Fastening performance relies entirely on heavily coupled parameter interactions. Independent geometric variables simply do not dictate joint survival.

4.1.11 Perturbation Sensitivity Behaviour

A separate perturbation analysis tested local stability. Each active design parameter was bumped by exactly 10%. The algorithm then recorded the resulting variation in the final retained clamp force.

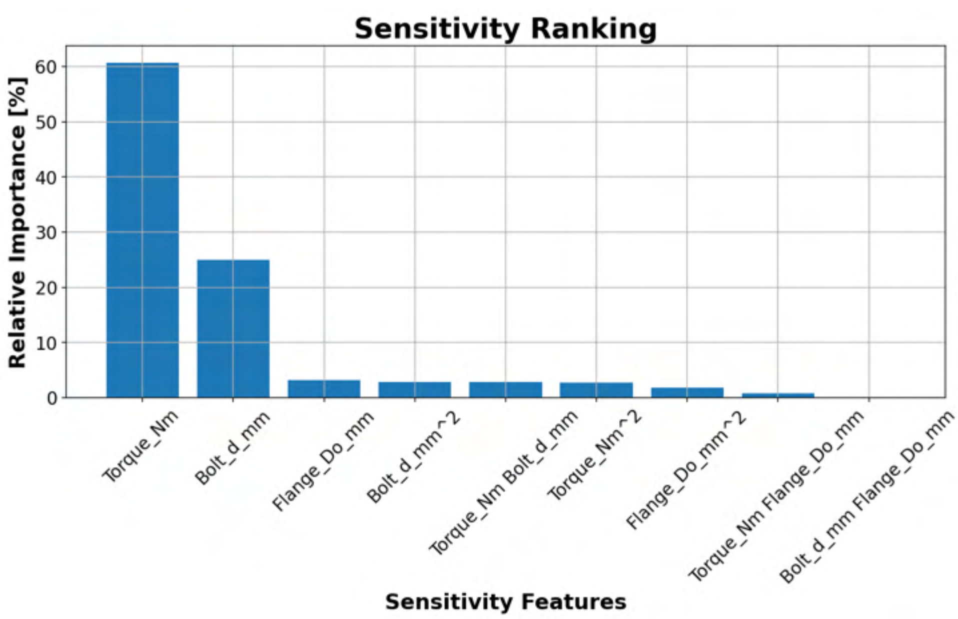

Figure 4.5: Perturbation sensitivity analysis illustrating the influence of primary fastening parameters on clamp force behaviour.

As reflected in the plot, model reduction followed a structured approach retaining the theoretically motivated RSM terms: the main effects of tightening torque and bolt diameter, their two-way interaction, and their second-

order curvature terms. Remaining factors, including flange outer diameter and its interactions, contributed less than 4% relative importance individually and were fixed at nominal levels, as their exclusion does not meaningfully affect the modelled response. This preserves a parsimonious yet physically interpretable model centered on the two dominant design variables.
The perturbation results highlight severe physical sensitivities:

- A 10% increase in tightening torque increased clamp force by approximately 15%
- Increasing bolt diameter reduced clamp force by approximately 10%
- Increasing flange diameter reduced clamp force by approximately 2%

Tightening torque acts as the absolute dominant engineering variable controlling final preload capacity.

The small direct sensitivity of the flange diameter completely masks its true engineering value. The flange actively prevents catastrophic failure. It redistributes the extreme stresses and kills the localized contact pressure spikes beneath the bolt head.

These physical perturbation results validate the absolute necessity of washer-supported fastening hardware.

4.1.12 Engineering Assumptions and Model Limitations

The computational framework relies on specific engineering assumptions. These assumptions make the rapid mathematical evaluation of massive design spaces possible.

The preload calculations use analytical torque-preload relationships. These equations assume perfectly uniform friction and axisymmetric load transfer beneath the fastener head. The optimization solver ignores microscopic thread deformation and hyper-local contact nonlinearities.

The contact stress models calculate average bearing pressures. They bypass complex mathematical stress singularities and ignore microscopic surface asperities beneath the fastener interface.

Standard ANSA thermoplastic material cards supplied the required creep parameters. The resulting long-term retention data functions strictly as a comparative engineering indicator. It does not provide a guaranteed absolute lifetime prediction.

The optimization loop ignores several dynamic operational hazards:

- Thermal cycling
- Hygrothermal ageing
- Fatigue loading
- Vibration-induced loosening
- Manufacturing tolerances

These mathematical simplifications allow the framework to run efficiently. The methodology delivers a highly accurate, physics-informed tool perfectly suited for the rapid early-stage optimization of thermoplastic joints.

4.1.13 Summary of Computational Findings

The computational framework establishes a fully scalable engineering methodology. It rapidly evaluates complex thermoplastic joints long before any expensive finite element analysis or physical testing occurs.

Washer-supported M6 fasteners completely dominate the performance metrics. They deliver superior load distribution, crush localized contact stresses, and preserve massive amounts of clamp force over time.

Tightening torque drives the entire fastening system. However, stable contact geometry and stiff thermoplastic materials actually dictate whether the joint survives long-term viscoelastic exposure.

The optimization data aggressively strips out weak design concepts. Discarding the M5 hardware instantly shrinks the computational design space. This forces the heavy nonlinear finite element models to focus exclusively on highly viable solutions.

Combining genetic optimization, massive DOE generation, and polynomial surrogate modelling creates a formidable engineering tool. This physics-driven workflow drastically accelerates the future development of structural thermoplastic fastening systems inside automotive applications.

4.2 Finite Element Analysis

4.2.1 Static FEM

4.2.1.1 Torque Scaling Investigation

Torque scaling studies evaluated how increasing preload conditions influence the nonlinear structural behavior of the thermoplastic assemblies. Assembly torque directly dictates clamp force. Increasing this torque improves preload retention. It simultaneously spikes localized contact pressure and creep susceptibility.

These simulation results and physical test outcomes provided the exact data needed to select standardized torque levels for the remaining comparative evaluations. All simulations in this section applied the baseline PC-ABS 1 material to maintain strict consistency.

Two representative automotive fastening configurations underwent evaluation:

- A-pillar doghouse geometry using an M6 flange screw.
- IC-ramp belt guide geometry applying an M6 captive washer-supported fastening concept.

4.2.1.1.1 A-Pillar Torque Progression The A-pillar simulations demonstrated heavily nonlinear deformation progression as the tightening torque increased. The localized deformation beneath the flange screw remained relatively stable at lower torque levels. This indicated functional load distribution within the screw boss.

Rapidly accelerating deformation growth occurred beneath the fastener once the torque exceeded approximately 6.0 Nm. The restricted contact area of the flange screw caused this physical behaviour. It concentrated the massive clamp force into a highly limited region. Figure 4.6 illustrates this progressive deformation evolution within the A-pillar geometry under increasing torque levels.

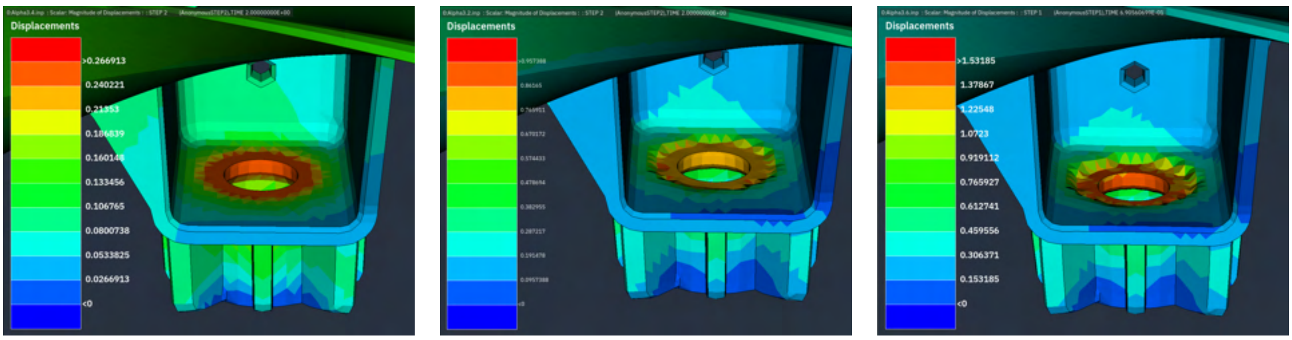

(a) 6 Nm load.　**(b)** 8 Nm load.　**(c)** 12 Nm load.

Figure 4.6: Deformation progression of the A-pillar doghouse under increasing torque levels.

The deformation behaviour revealed clear evidence of localized stiffness degradation at elevated preloads. The applied torque increased linearly. The resulting deformation growth became highly nonlinear. Table 4.5 summarizes this effect. The deformation increased from 0.2 mm at 6.0 Nm to 1.4 mm at 12.0 Nm. This represents a massive growth of over 470 percent. The excessive preload generated severe compressive yielding at these higher loads rather than effectively increasing the structural clamp capability.

Table 4.5: Load sensitivity analysis for the A-pillar with an M6 flange screw.

Torque Load	FEA Def. (mm)	Contact Force (N)
6.0 Nm	0.2	21.5
8.0 Nm	0.8	27.1
12.0 Nm	1.4	31.8

The simulations also revealed an asymmetric structural response within the underlying support ribs beyond the localized surface yielding. Figure 4.7 illustrates this effect. The closed side rib of the doghouse consistently experienced a significantly higher magnitude of stress compared to the open side. The continuous geometry of the closed side provides much higher structural stiffness. This stiffer geometry draws and concentrates a disproportionately larger share of the compressive axial load transferred from the fastener.

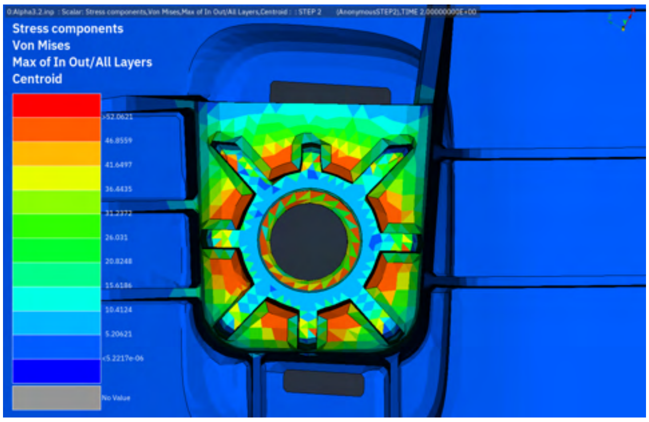

Figure 4.7: Simulated stress distribution within the A-pillar doghouse, demonstrating higher stress concentrations along the closed side rib.

4.2.1.1.2 IC-Ramp Torque Progression The IC-ramp component recorded a much more stable response relative to the A-pillar due to the captive washer. The wider contact area redistributed the clamp load uniformly across the plastic interface. This reduced localized force concentration and maintained high structural stiffness at elevated torque levels. Figure 4.8 presents the specific deformation evolution observed for the IC-ramp fastening system.

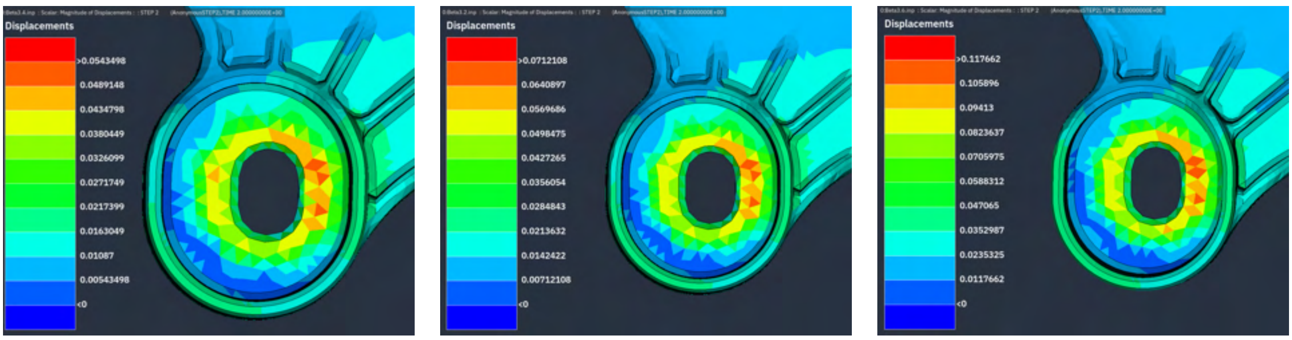

(a) 6.0 Nm load. **(b)** 8.0 Nm load. **(c)** 12.0 Nm load.

Figure 4.8: Deformation progression of the IC-ramp doghouse under increasing torque levels.

The captive washer yielded far lower deformation concentration throughout the entire loading range compared to the flange screw. Table 4.6 details this physical response. The macroscopic deformation only grew from 0.04 mm at 6.0 Nm to 0.11 mm at 12.0 Nm.

Table 4.6: Load sensitivity analysis for the IC-ramp with an M6 captive washer.

Torque Load	FEA Def. (mm)	Contact Force (N)
6.0 Nm	0.04	28.3
8.0 Nm	0.06	37.7
10.0 Nm	0.06	38.9
12.0 Nm	0.11	56.8

The contact force naturally increased with the escalating preload. The captive washer geometry successfully delayed the onset of localized instability. Designing thermoplastic joints for elevated clamp forces absolutely requires maximizing the effective contact area.

4.2.1.2 Material Behaviour Investigation

Material comparison studies evaluated how the specific material grades influence deformation resistance and structural stability under equivalent preload conditions.

The tested materials possess completely different combinations of stiffness, ductility, and yield behaviour. These physical variations produced substantial differences in fastening response throughout the simulation matrix.

4.2.1.2.1 A-Pillar Material Ranking The A-pillar material comparison proved that the PC-ABS materials consistently exhibited a more stable response under flange screw loading conditions. Figure 4.9 presents the comparative deformation response mapped across the investigated material configurations.

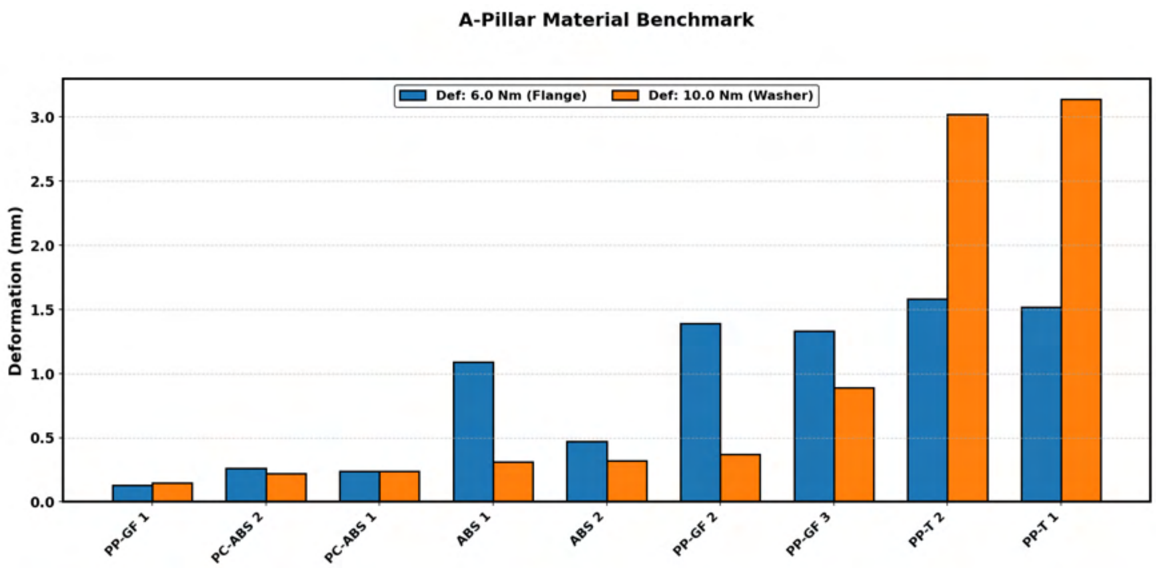

Figure 4.9: Comparative deformation ranking of polymer grades on the A-pillar geometry.

The PC-ABS materials demonstrated high resistance to localized compressive yielding. PC-ABS 1 limited macroscopic deformation to 0.24 mm. PC-ABS 2 recorded a nearly identical displacement of only 0.26 mm. These specific materials produced the absolute lowest deformation levels while maintaining excellent functional load distribution.

The PP-T materials exhibited severe sensitivity to the applied load beneath the flange interface. PP-T 1 and PP-T 2 recorded extreme localized deformation values exceeding 1.50 mm. High compressive compliance drove this physical failure.

Increased material stiffness does not fully eliminate structural sensitivity. Highly localized contact pressure concentrations still developed at elevated preloads even for the rigid PC-ABS configurations. The limited geometric contact area beneath the standard flange fastener interface dictates this physical limitation.

4.2.1.2.2 IC-Ramp Material Ranking The IC-ramp material investigations recorded similar material-dependent behaviour. The captive washer fastening concept substantially reduced the overall deformation sensitivity between the evaluated polymer systems.

Figure 4.10 illustrates the comparative deformation response observed for the tested materials under the 10.0 Nm captive washer loading condition.

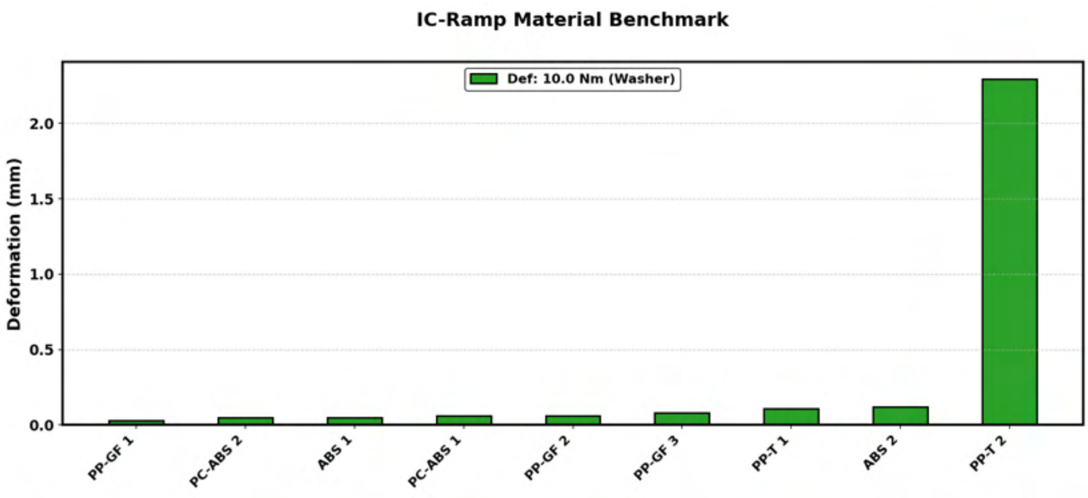

Figure 4.10: Comparative deformation ranking of polymer grades on the IC-ramp geometry at 10.0 Nm.

The improved load redistribution generated by the washer geometry heavily reduced localized displacement. This physical shift decreased the structural sensitivity to material stiffness variation. The PP-GF 1 material recorded the highest structural stability. It yielded a minimal 0.03 mm of deformation. The PP-T 2 material recorded the highest sensitivity. It suffered a massive 2.30 mm of macroscopic displacement under the exact same load.

These results confirm a critical engineering principle. Fastening geometry optimization partially compensates for material limitations by improving the efficiency of the contact pressure redistribution mechanism.

4.2.1.2.3 Cross-Component Material Consistency: A-Pillar vs. IC-Ramp Comparing the material rankings between the A-pillar and the IC-ramp reveals a highly consistent relative hierarchy. The fundamentally different macro-geometries of the two components did not alter this order. The PC-ABS and PP-GF materials systematically exhibited the highest resistance to compressive yielding across both applications. The PP-T grades consistently ranked at the bottom. They demonstrated critical sensitivity to elevated preloads regardless of the supporting component shape.

4.2.1.3 A-Pillar Fastening Interface: Flange vs. Captive Washer Comparison

The baseline A-pillar doghouse was modified to accommodate an 18.0 mm captive washer. This isolated the explicit structural influence of the bearing geometry. Finite element simulations then benchmarked its deformation behaviour directly against the standard M6 flange screw configuration.

Figure 4.11 provides a direct visual comparison of the localized yielding and macroscopic displacement generated by the two geometries under an identical 6.0 Nm target torque.

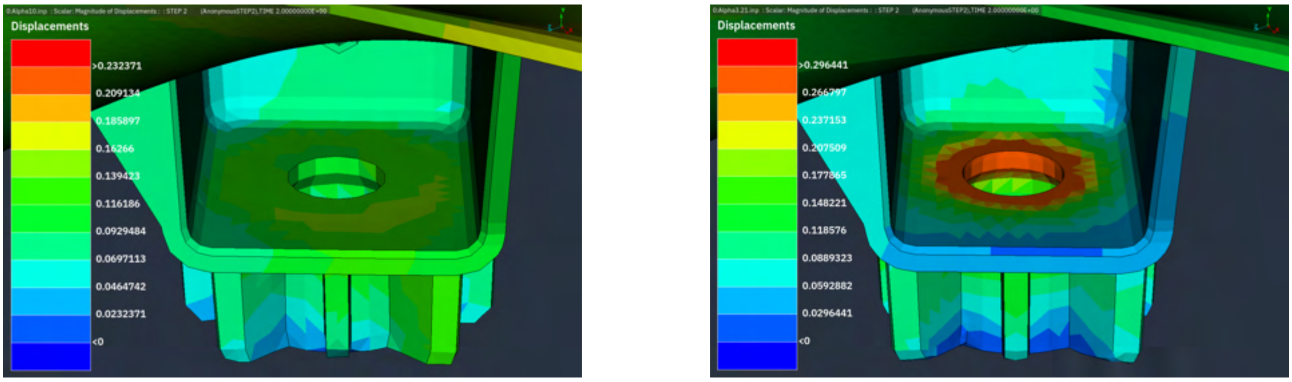

(a) Deformation contour: M6 Flange (6.0 Nm).

(b) Deformation contour: M6 Washer (6.0 Nm).

Figure 4.11: Simulated macroscopic deformation on the A-pillar fastening interface.

Figure 4.12 summarizes the displacement results across the entire material matrix and quantifies the structural transition. The simulated values were extracted directly from the untreated friction models. This evaluated the 6.0 Nm flange baseline, the 6.0 Nm washer optimization, and the washer at an elevated 10.0 Nm load.

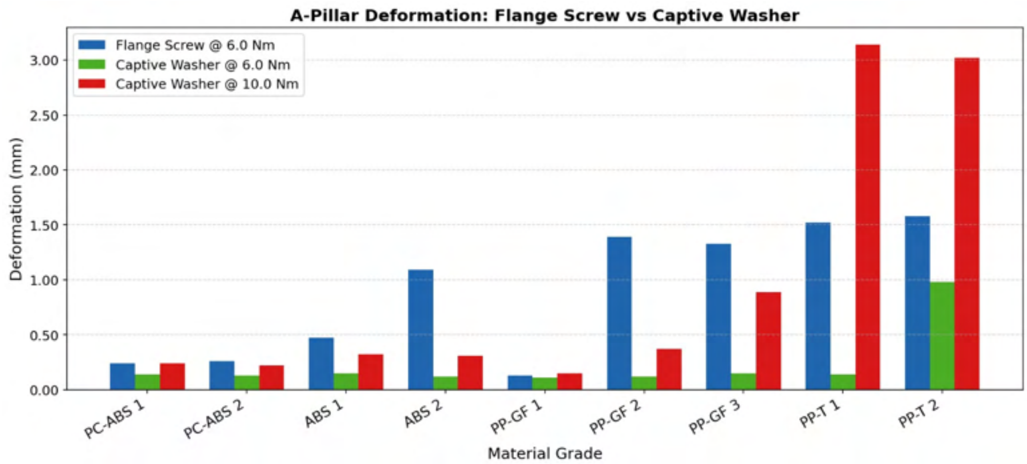

Figure 4.12: Comparison of simulated deformation for the flange screw and captive washer configurations at 6.0 Nm and 10.0 Nm.

The numerical data reveals a drastic improvement in structural stability when transitioning to the captive washer. The expanded footprint of the washer reduced macroscopic deformation by an average of 64 percent across the evaluated matrix at the standard 6.0 Nm assembly torque. Figure 4.12 summarizes this trend visually.

Contact mechanics govern this behaviour entirely. The standard flange screw acts as a high-stress point-load. It concentrates the entire clamping force onto a narrow 13.6 mm annular ring. This localized pressure easily exceeds the compressive yield limit of the softer matrices (such as ABS 2 and PP-GF 2). The screw head rapidly embeds or punches through the surface. The captive washer fundamentally transforms this load path by expanding the bearing diameter to 18.0 mm. It distributes the identical clamping force over a substantially larger surface area. This drops the localized contact pressure well below the critical yield threshold of the polymer.

The most compelling engineering trend emerges when pushing the joint to higher limits. The washer optimizes the load redistribution so effectively that the assembly torque was safely increased to 10.0 Nm. Figure 4.12 illustrates this outcome. The resulting displacement for nearly all materials remained lower or equal to the damage caused by the flange screw at only 6.0 Nm, even after increasing the applied torque by 66 percent.

The highly compliant PP-T matrices provide the only isolated exceptions to this trend. The elevated 10.0 Nm compressive load physically overwhelmed the bulk shear strength of the plastic doghouse itself for these specific grades. This led to severe structural yielding (exceeding 3.00 mm) regardless of the washer's surface support. The data confirms a clear conclusion for all other engineering grades. Applying a captive washer provides the exact structural ceiling needed to safely achieve standard industrial torques without requiring metal compression limiters.

4.2.1.4 Clearance Hole Geometry Optimization

Transitioning from a standard oval clearance hole to a modified circular hole consistently reduced macroscopic deformation. It improved contact force generation across all evaluated materials. The baseline oval geometry creates incomplete annular contact beneath the fastener head. This missing support destroys the effective load-bearing area and generates severe localized pressure concentrations.

Figure 4.13(a) maps the contact normal force distribution for the standard oval clearance hole. The extracted force contours highlight a severe physical imbalance. The structural sections along the elongated sides of the oval hole absorb a disproportionately massive share of the normal contact forces. This severe load distribution directly motivated the transition to a smaller, circular clearance hole (Figure 4.13(b)). The circular geometry maximizes continuous annular contact. This structural change forces a perfectly uniform distribution of the compressive load across the entire bearing surface.

Table 4.7 summarizes the numerical response comparing these two geometries at a 10.0 Nm captive washer load.

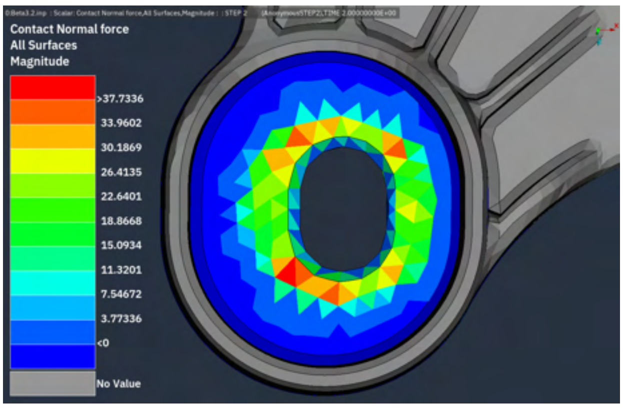

(a) Contact normal force distribution: Standard oval hole.

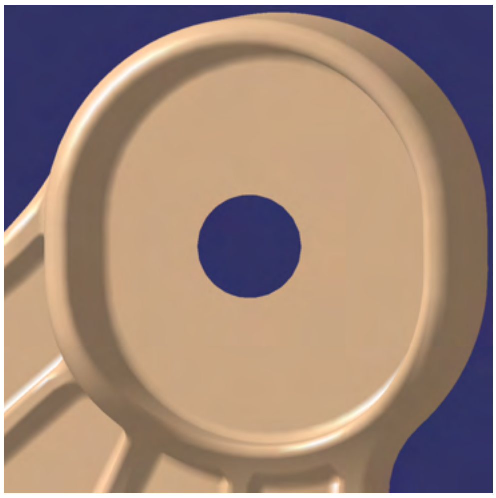

(b) Modified circular clearance hole geometry.

Figure 4.13: Geometric and contact force comparison of the IC-ramp fastening interface.

Table 4.7: Numerical results comparing simulated deformation and contact force between standard oval and modified circular clearance holes at a 10.0 Nm target torque.

	Oval Hole		**Circular Hole**	
Material	**Def. (mm)**	**Contact Force (N)**	**Def. (mm)**	**Contact Force (N)**
PC-ABS 1	0.06	38.9	0.04	40.8
PC-ABS 2	0.05	39.1	0.04	41.0
ABS 1	0.05	49.4	0.04	56.8
ABS 2	0.12	46.0	0.06	53.0
PP-GF 1	0.03	43.6	0.02	48.8
PP-GF 2	0.06	43.2	0.03	46.9
PP-GF 3	0.08	43.1	0.05	45.9
PP-T 1	0.11	42.3	0.04	43.6
PP-T 2	2.29	43.4	0.21	38.0

The numerical data quantifies the absolute structural necessity of continuous annular contact. Rigid grades (PC-ABS and ABS 1) recorded an average deformation reduction of approximately 24 percent. Materials possessing intermediate stiffness (ABS 2 and PP-GF grades) recorded more substantial displacement reductions ranging between 37 and 50 percent.

The highly compliant PP-T 2 matrix isolated the greatest structural benefit. The incomplete contact of the oval hole triggered massive localized matrix collapse under the 10.0 Nm load. It generated 2.29 mm of displacement. Transitioning to the circular hole completely resolved this instability. The absolute deformation dropped to 0.21 mm. Geometric optimization of the bearing surface alone delivered an incredible 91 percent reduction in macroscopic displacement.

4.2.2 Dynamic FEM: Viscoelastic Creep and Long-Term Thermal Stability

Viscoelastic creep in thermoplastic joints dictates the progressive relaxation of internal stresses and the direct loss of clamp load. Assembly-level contact mechanics extracted directly from the active fastener interface quantified this long-term stability.

Average contact normal force (CNORMF) and average contact pressure (CPRESS) replaced discrete nodal maxima. This eliminated mesh dependency and avoided localized numerical spikes. Comparing the initial tightening condition (0 hours) to the relaxed state after 1000 hours evaluated the structural retention for all converged simulations.

The retained clamp load and contact pressure metrics reflect simple percentages of their initial starting values. Post-processing explicitly evaluated these retention rates according to:

$$\text{Clamp Load Retention} = \left(\frac{\text{CNORMF}_{1000h}}{\text{CNORMF}_0} \right) \cdot 100 \tag{4.5}$$

$$\text{Contact Pressure Retention} = \left(\frac{\text{CPRESS}_{1000h}}{\text{CPRESS}_0} \right) \cdot 100 \tag{4.6}$$

Figure 4.14 maps the quantitative retention behaviour for the A-pillar geometry across the investigated thermal conditions (-10°C, 23°C, and 60°C).

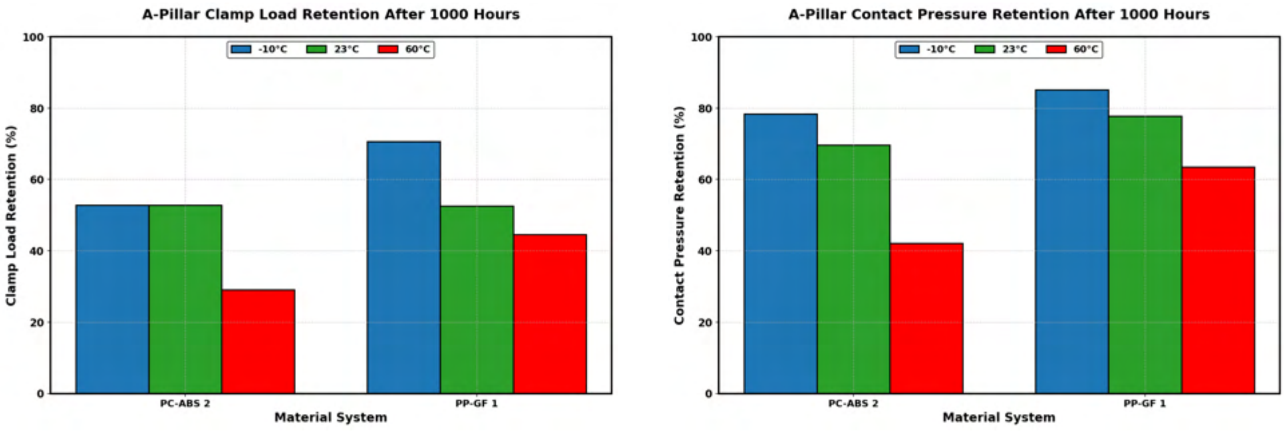

(a) Clamp load retention.

(b) Contact pressure retention.

Figure 4.14: A-pillar (flange screw) viscoelastic retention metrics after 1000 hours.

4.2.2.1 Engineering Interpretation of Creep Mechanics

The extracted numerical data from the A-pillar flange interface yields three primary engineering conclusions regarding long-term fastener durability:

1. Direct Correlation Between Load and Interface Pressure
Clamp load retention and contact pressure retention demonstrate nearly identical parity across all evaluated materials. This mechanical alignment confirms a fundamental reality. Microscopic pressure relaxation directly beneath the fastener head entirely governs macroscopic preload loss. The data dictates a strict 1:1 structural relationship. The localized polymer interface yields and redistributes pressure under the narrow flange footprint. The global axial clamp force decays at a functionally identical rate.

2. Thermal Sensitivity and Material Architecture
The PC-ABS matrices exhibit acceptable stability under flange loading at standard operating temperatures (23°C). They retain approximately half of their initial clamp force. These exact systems record severe thermal sensitivity at elevated environments (60°C). Thermal softening accelerates viscoelastic flow and heavily degrades the retention capacity. The PP-GF systems demonstrate superior thermal stability. The rigid internal glass architecture mechanically constrains the polymer matrix. It heavily resists localized embedding. This locks the contact pressure in place beneath the flange screw even at elevated temperatures.

3. Physical Significance of Non-Convergence
Simulations failing to converge through the 1000-hour duration do not represent numerical anomalies. These exact aborts document total physical interface collapse. Viscoelastic softening generates rapid local compliance growth under the sustained compressive stress of the flange screw. Runaway localized yielding and unstable pressure redistribution follow immediately. Total structural failure of the boss geometry occurs well before the 1000-hour threshold.

The simulations confirm a rigid engineering baseline. Long-term bolt retention for standard flange configurations strictly requires a highly rigid initial matrix at room temperature or an architecture capable of arresting thermal-mechanical flow at elevated temperatures. Anything less guarantees catastrophic preload loss.

4.2.3 Validation of FEA against Physical Tests

Numerical simulations evaluated directly against the physical laboratory outcomes established a firm engineering correlation. This validation compares the observable physical outcomes of the tested components against the structural response calculated by the FEA model. The validation applies identical component geometries, material classifications, and fastener types across both the physical laboratory and the virtual environment.

4.2.3.1 A-Pillar Validation

Physical torque testing of the A-pillar doghouses with a standard M6 flange screw recorded explicit structural limits. Table 4.8 aligns the physical observations of the PC-ABS 2 variant with the corresponding FEA simulation.

Table 4.8: Direct correlation for A-pillar components using PC-ABS 2.

Component	Physical Test	Obs.	FEA Load	Def. (mm)	Stress (MPa)
A-pillar (PC-ABS 2)	5.0 Nm Flange	OK	5.0 Nm Flange	0.18	46.7

The computational models proved accurate. The numerical data aligns with the physical test outcomes.

4.2.3.2 IC-Ramp Validation

Physical testing of the IC-ramp geometry explicitly evaluated captive washer applications. Table 4.9 presents the simulated data for the PP-GF 1 material alongside the physical observations for the 10.0 Nm washer configurations.

Table 4.9: Direct correlation for the IC-ramp using PP-GF 1 under captive washer loads.

Component	Physical Test	Obs.	FEA Load	Def. (mm)	Stress (MPa)
IC-ramp (PP-GF 1)	10.0 Nm Washer	OK	10.0 Nm Washer	0.03	59.8

The physical tests recorded absolutely zero macroscopic joint failure for the PP-GF 1 material at the 10.0 Nm captive washer application. The simulation calculates a matching stable response. It yields a minimal localized deformation of 0.03 mm and a functional internal stress of 59.8 MPa.

4.2.4 Engineering Interpretation of the Parametric FEM Investigations

The combined finite element investigations redefine the structural approach to direct screw-fastened thermoplastic joints. Relying on elevated tightening torques inherently generates massive localized stress concentrations and heavily accelerates viscoelastic yielding. Contact pressure redistribution fundamentally dictates the effectiveness of the entire fastening system.

Integrating the captive washer represents the most impactful structural optimization identified in the study. The captive washer explicitly decouples high clamp forces from localized matrix yielding by expanding the bearing footprint to 18.0 mm. This specific configuration uniformly redistributes the axial load. It yields substantially lower macroscopic deformation across all evaluated engineering materials. The simulations confirm that applying a captive washer operates as a strict design requirement for achieving a stable response and maximizing clamp retention. The narrow profile of the standard flange screw remains structurally insufficient for high-load thermoplastic applications.

This reliance on bearing area extends directly to the clearance hole geometry. Transitioning from an elongated oval hole to a minimized circular clearance hole guarantees continuous annular contact beneath the fastener head. Eliminating geometric voids in the bearing surface prevents localized pressure spikes. This stabilizes the joint and yields a measurable reduction in overall displacement. The data dictates that pairing a captive washer with a minimized circular clearance hole establishes the absolute optimal geometric hierarchy for joint stability.

The material evaluations and viscoelastic creep studies establish definitive operational boundaries for the polymer matrices. The PC-ABS and PP-GF 1 materials provide the necessary initial stiffness to resist immediate compressive yielding. The dynamic long-term data isolates severe thermal sensitivity as a hidden failure mode. PC-ABS materials maintain high clamp retention at 23°C. Elevated environments (60°C) push the matrix straight toward its thermal softening point. This yields rapid and severe clamp load loss.

The creep data records an important physical divergence. The PP-GF materials successfully prevent visual macroscopic geometric distortion. The underlying matrix still experiences intense microscopic relaxation. This yields a hidden internal drop in clamp force even when the physical component appears structurally intact.

Direct validation against the physical laboratory tests confirms the precise accuracy of the computational models. The integrated findings mandate a specific engineering hierarchy for automotive thermoplastic fastening. Geometric optimization of the bearing interface supersedes basic material substitution. Integrating captive washers and ensuring continuous annular contact remains the absolute most effective method for generating high clamp retention and guaranteeing long-term structural integrity.

4.3 Physical Experiments

4.3.1 Friction and Initial Relaxation

The initial test phase extracted the governing friction coefficients. It also evaluated the immediate viscoelastic relaxation of the thermoplastic joints. Table 4.10 outlines the specific combinations of materials and screw types tested during this phase.

Table 4.10: Overview of performed friction and relaxation tests.

Test Number	Material	Screw Type
1	ABS (Generic)	Treated Black Screw
2	ABS (Generic)	Untreated Silver Screw
3	PP (Generic)	Untreated Silver Screw
4	PC-ABS (Production Panel)	Untreated Silver Screw
5	PC-ABS (Production Panel)	Treated Black Screw
6	PP (Generic)	Treated Black Screw
7	PP-GF (Production Panel)	Treated Black Screw
8	PP-GF (Production Panel)	Untreated Silver Screw
9	PP (Production Panel)	Untreated Silver Screw
10	PP (Production Panel)	Untreated Silver Screw

4.3.1.1 Extracted Friction Coefficients

Physical measurements defined the true contact area between the underside of the screw head and the mating plastic surface (Figure 4.15). This isolated the exact bearing friction (μ_b). The effective contact zone yielded an outer diameter (D_o) of 12.7 mm and an inner clearance diameter (D_i) of 6.7 mm. Equation 2.16 applied these physical dimensions to calculate the mean bearing radius (r_m). The torque-preload mathematical model (Equation 2.15) then extracted the specific friction coefficients.

Internal thread friction (μ_g) between the steel fastener and the steel nut remained highly consistent across all test cycles. An average calculation established a constant thread friction coefficient of $\mu_g = 0.108$. This constant drove all theoretical analyses.

Figure 4.15 illustrates the physical condition of the thermoplastic test specimens after the friction evaluation. It displays clear, distinct contact wear patterns.

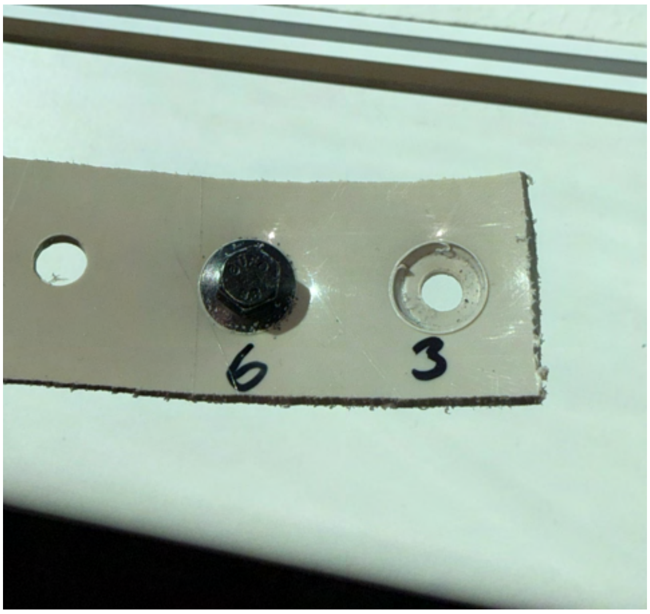

Figure 4.15: Surface condition of the plastic strips post-friction testing, showing the localized bearing contact area under the screw head.

Table 4.11 summarizes the calculated bearing friction coefficients for each material and surface treatment combination evaluated at 75 percent of the fastener proof load.

Table 4.11: Extracted bearing friction coefficients (μ_b) by material and screw treatment.

Material	Untreated Silver Screw	Treated Black Screw
ABS		0.14
PP	0.19	0.19
PC-ABS	0.21	0.19
PP-GF	0.19	0.19

The black surface treatment reduced the overall average friction coefficient by 5.6 percent. The ABS and PC-ABS matrices primarily drove this decrease. They recorded massive friction drops. The friction coefficients for the PP and PP-GF matrices remained largely unaffected. Some even increased slightly under the treated screw condition.

4.3.1.2 Initial Clamping Force Relaxation

Generated axial preload does not remain static. Thermoplastics possess an inherently viscoelastic nature. The material undergoes immediate localized yielding and creep under the screw head right after the final tightening torque hits the target. This triggers a rapid decay of the initial clamping force.

The test rig held the joints in their fully tightened position for exactly 60 seconds while sensors continuously monitored the internal tension. Figure 4.16 displays the clamping force retention over this hold period across all evaluated plastics.

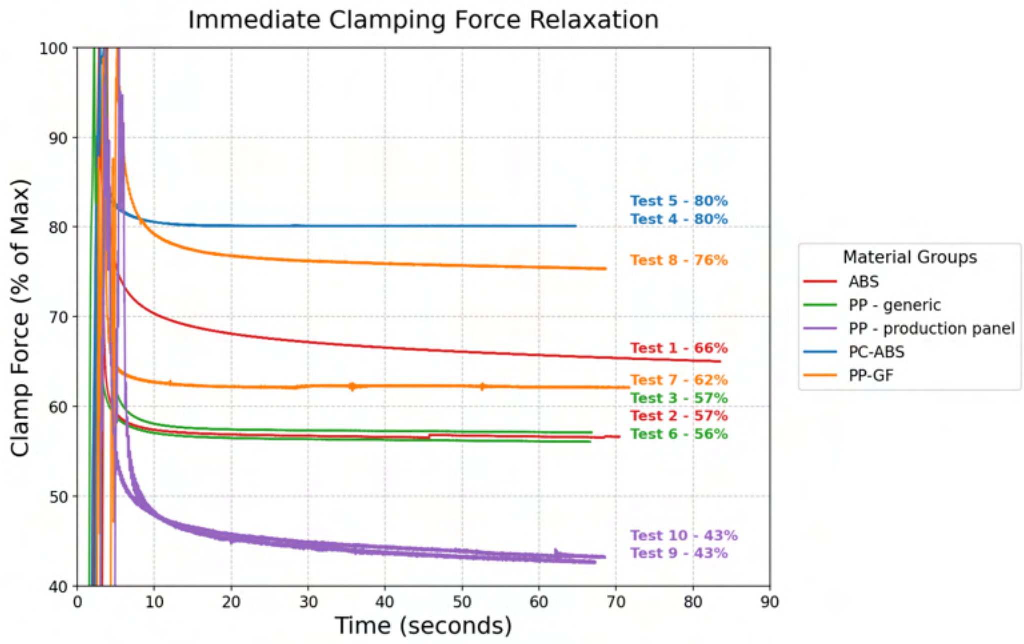

Figure 4.16: Comparison of clamping force decay across different thermoplastic materials over a 60-second hold period.

A massive portion of the clamping force disappears within one single minute. The plastic panels yield under high localized compressive stress. This causes immediate viscoelastic relaxation and drives the rapid force decay. This initial relaxation reacts aggressively to the specific polymer architecture. Different parts produce drastically different load retention profiles.

PC-ABS demonstrated the highest structural stability. It relaxed the least and safely retained roughly 80 percent of its initial clamping force. Intermediate materials, heavily featuring ABS and PP-GF configurations, clustered tightly together. They retained between 57 and 76 percent of their initial load.

PP materials suffered the most severe force decay. Generic PP test strips retained approximately 57 percent of their initial clamping force. PP strips cut directly from actual production panels performed much worse. Their retention collapsed to 43 percent. This extreme variation confirms a hard engineering reality. The specific material grade and component geometry strictly dictate joint loosening rates even within the exact same polymer family.

4.3.1.3 Effect of Surface Graining on Friction Coefficient

An additional physical test compared the friction coefficients between the grained side and the shiny, ungrained side of a PP plastic strip. This isolated the explicit influence of surface texture on joint mechanics. Figure 4.17 plots the bearing friction coefficient against the clamping force for both physical surface conditions.

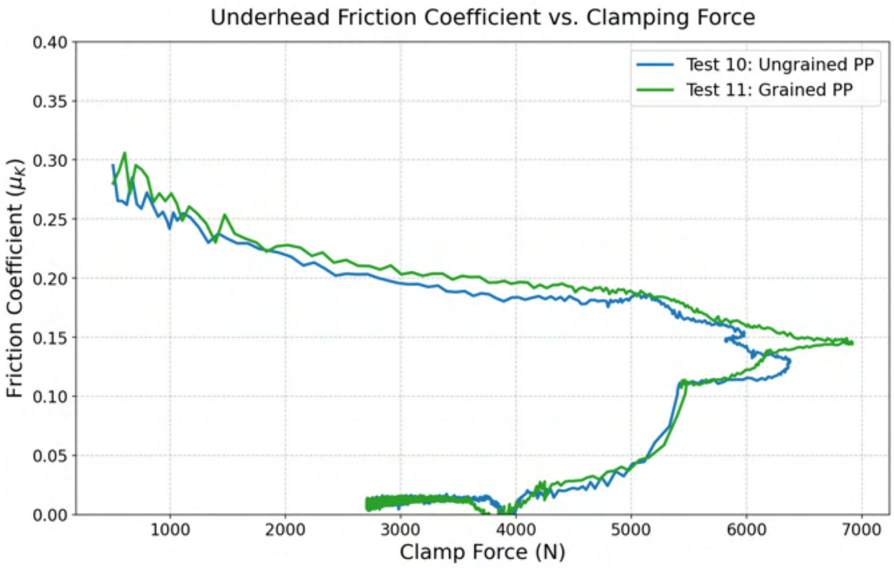

Figure 4.17: Comparison of bearing friction coefficients versus clamp force for grained and shiny PP surfaces.

The grained surface exhibits a slightly higher friction coefficient than the shiny surface. This minor variation falls perfectly within the expected normal spread for mechanical friction testing. Evaluating a single physical specimen for each condition restricts the statistical power of the test. The primary physical observation remains clear despite the small sample size. Surface graining does not drastically alter the core friction characteristics compared to a completely ungrained surface.

4.3.2 Torque Capacity Test

This section details physical failure modes and maximum torque capacities for each tested thermoplastic component. Applying structural loads up to and beyond the standard 10 Nm assembly target directly compares standard flange screws against captive washer configurations. Analyzing the localized yielding and ultimate failure points identifies the exact mechanical limits of each joint.

4.3.2.1 ABS

ABS 2 (Belt guide 2)
Tests 1, 3, and 5 evaluated an M6 flange screw without a washer.

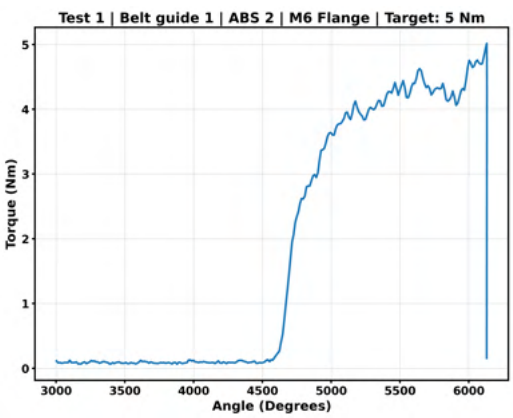

(a) Torque vs. Time plot.

(b) Close-up of physical joint.

Figure 4.18: Test 1: ABS 2 (Belt guide 2), M6 screw without washer. Target torque: 5.0 Nm.

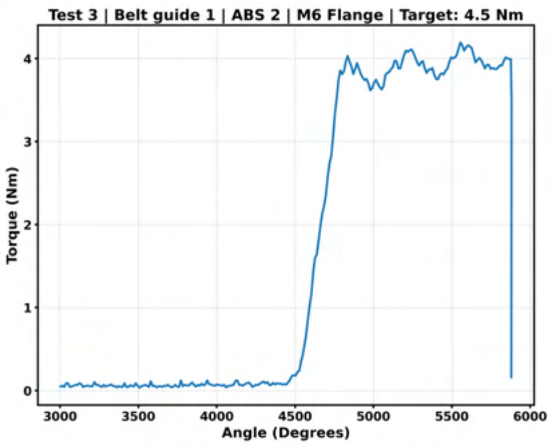

(a) Torque vs. Time plot.

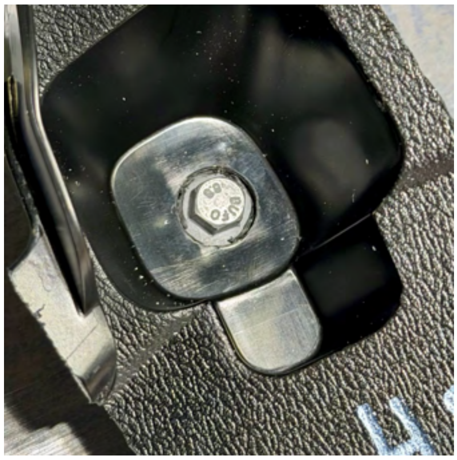

(b) Close-up of physical joint.

Figure 4.19: Test 3: ABS 2 (Belt guide 2), M6 screw without washer. Target torque: 4.5 Nm.

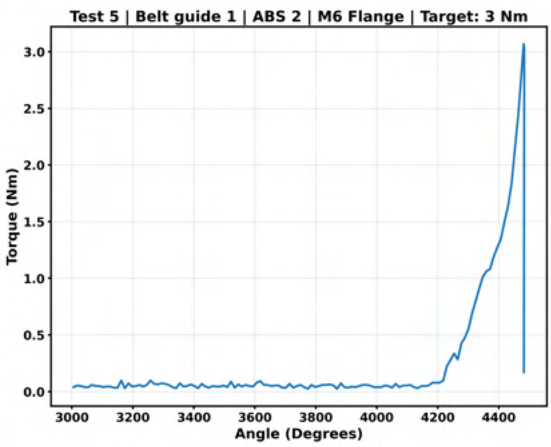

(a) Torque vs. Time plot.

(b) Close-up of physical joint.

Figure 4.20: Test 5: ABS 2 (Belt guide 2), M6 screw without washer. Target torque: 3.0 Nm.

Tests 1 and 3 failed at target torques of 5.0 Nm and 4.5 Nm. The screw head penetrated and completely deformed the material. The torque plots confirm plastic deformation initiates around 3.8 to 4.0 Nm. Test 5 targeted 3.0 Nm and passed successfully. The physical close-up shows zero visible deformation. The stable torque plot verifies this result.

Tests 2, 4, and 6 evaluated an M6 screw equipped with a captive washer.

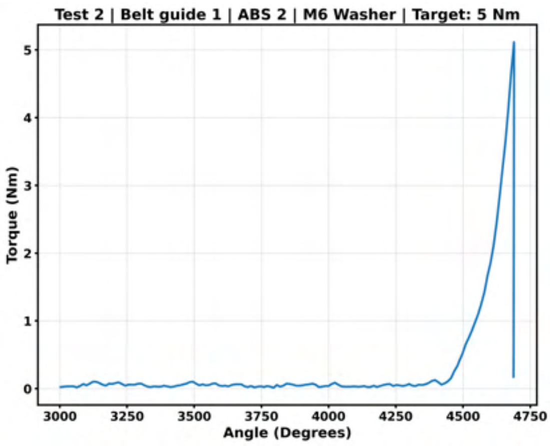

(a) Torque vs. Time plot.

(b) Close-up of physical joint.

Figure 4.21: Test 2: ABS 2 (Belt guide 2), M6 screw with washer. Target torque: 5.0 Nm.

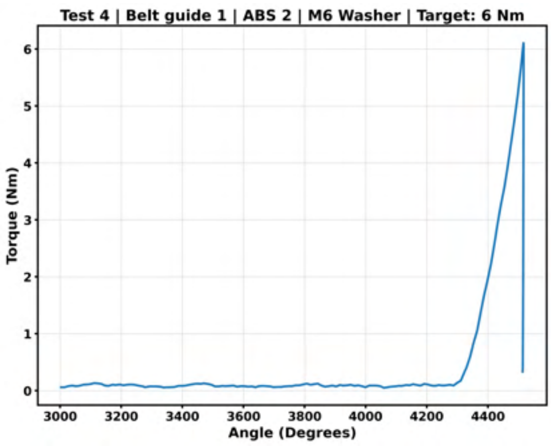

(a) Torque vs. Time plot.

(b) Close-up of physical joint.

Figure 4.22: Test 4: ABS 2 (Belt guide 2), M6 screw with washer. Target torque: 6.0 Nm.

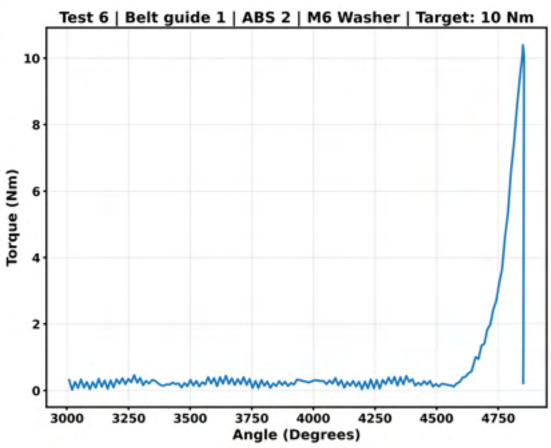

(a) Torque vs. Time plot.

(b) Close-up of physical joint.

Figure 4.23: Test 6: ABS 2 (Belt guide 2), M6 screw with washer. Target torque: 10.0 Nm.

Test 6 applied a maximum 10.0 Nm target torque. The joint safely withstood the load. Neither the physical inspection nor the torque curves show any visible deformation. The material limits remained completely unbroken during these specific cycles.

ABS 2 (Belt guide 1)

Tests 7, 9, and 10 evaluated an M6 flange screw without a washer.

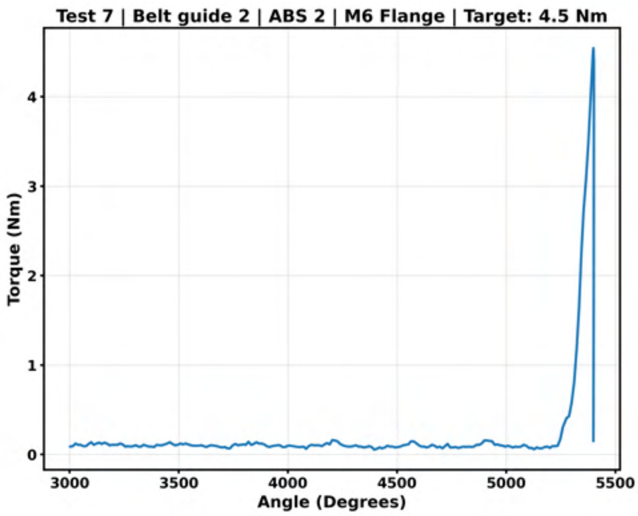

(a) Torque vs. Time plot.

(b) Close-up of physical joint.

Figure 4.24: Test 7: ABS 2 (Belt guide 1), M6 screw without washer. Target torque: 4.5 Nm.

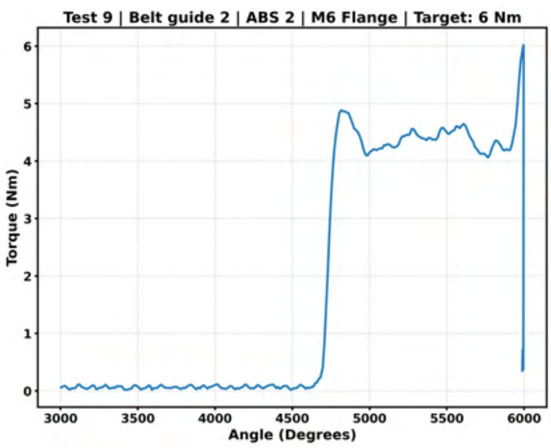

(a) Torque vs. Time plot.

(b) Close-up of physical joint.

Figure 4.25: Test 9: ABS 2 (Belt guide 1), M6 screw without washer. Target torque: 6.0 Nm.

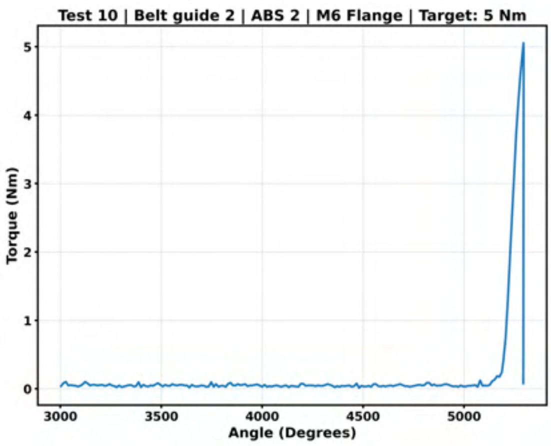

(a) Torque vs. Time plot.

(b) Close-up of physical joint.

Figure 4.26: Test 10: ABS 2 (Belt guide 1), M6 screw without washer. Target torque: 5.0 Nm.

Test 7 (4.5 Nm) yielded acceptable results. The close-up and torque plot show zero visible deformation. Test 9 (6.0 Nm) resulted in total failure. The screw fully deformed the plastic matrix. The torque plot indicates deformation begins around 4.8 to 4.9 Nm. Test 10 targeted 5.0 Nm and passed without visible deformation. This clean result slightly contradicts the 4.8 to 4.9 Nm yield point observed in Test 9.

Comparison of Component Geometries (Belt guide 1 vs. Belt guide 2)

Belt guide 1 and Belt guide 2 consist of the exact same ABS 2 material grade. The variation in their test outcomes isolates the massive influence of local component geometry. The flange screw tests show Belt guide 1 safely sustaining 5.0 Nm loads. Belt guide 2 yielded at 4.5 Nm. The structural design and local stiffness of Belt guide 1 provide far better mechanical support under identical standard fastening conditions.

Local geometry heavily dictates the failure point under flange screw loading. Introducing a captive washer entirely neutralizes these geometric weaknesses. Applying a washer to either belt guide design massively increased the overall torque capacity. Both joints easily supported 10.0 Nm loads. The washer effectively overwrote the local structural discrepancies.

Tests 8 and 11 evaluated an M6 screw equipped with a captive washer.

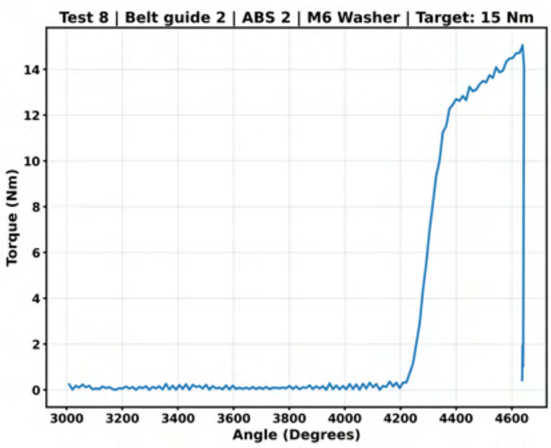

(a) Torque vs. Time plot.

(b) Close-up of physical joint.

Figure 4.27: Test 8: ABS 2 (Belt guide 1), M6 screw with washer. Target torque: 15.0 Nm.

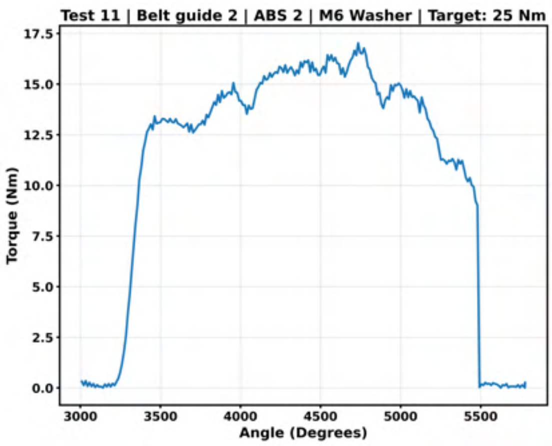

(a) Torque vs. Time plot.

(b) Close-up of physical joint.

Figure 4.28: Test 11: ABS 2 (Belt guide 1), M6 screw with washer. Target torque: 25.0 Nm.

Physical inspection of Test 8 (15.0 Nm target) reveals no macroscopic surface deformation. The recorded torque data contradicts this visual assessment. Yield initiation begins at approximately 12.5 Nm. This corresponds to roughly 250 degrees of screw rotation (from 4400° to 4650°). An M6 screw features a standard 1.0 mm thread pitch. One full 360° rotation equals 1.0 mm of axial travel. The axial deformation depth calculates exactly as:

$$\text{Distance} = \text{Pitch} \cdot \left(\frac{\text{Degrees}}{360^\circ}\right) = 1.0 \text{ mm} \cdot \left(\frac{250^\circ}{360^\circ}\right) \approx 0.69 \text{ mm} \tag{4.7}$$

A 0.69 mm indentation represents minimal structural movement. This explains why the deformation remains virtually imperceptible in the physical close-up without dismantling the joint. Test 11 confirms this specific behaviour. Deformation initiates precisely at the 12.5 Nm threshold. The ultimate torque reaches 17.0 Nm before the steel fastener begins to fail. It eventually fractures completely. The physical evidence proves the screw does not pull through the material. It shears entirely from torsional overload.

4.3.2.2 PC-ABS

PC-ABS 1 (A-pillar 1)

Tests 12, 13, 14, and 15 evaluated an M6 flange screw without a washer.

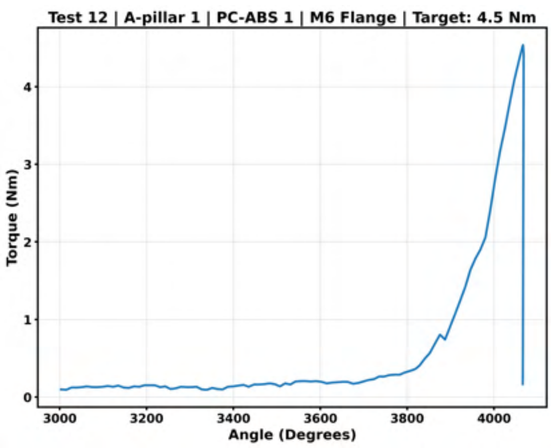

(a) Torque vs. Time plot.

(b) Close-up of physical joint.

Figure 4.29: Test 12: PC-ABS 1 (A-pillar 1), M6 screw without washer. Target torque: 4.5 Nm.

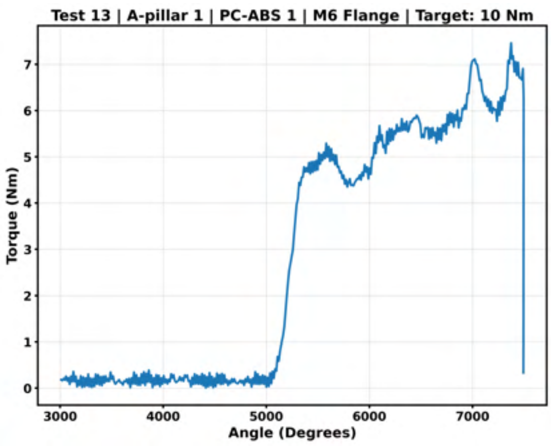

(a) Torque vs. Time plot.

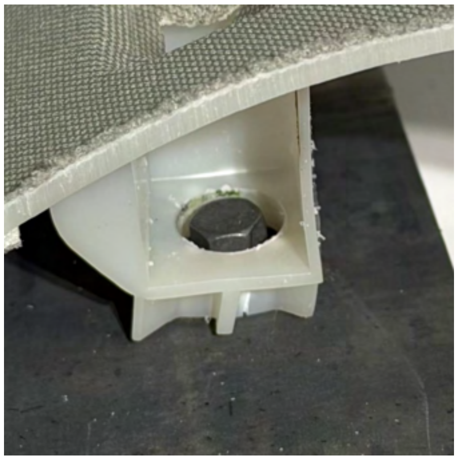

(b) Close-up of physical joint.

Figure 4.30: Test 13: PC-ABS 1 (A-pillar 1), M6 screw without washer. Target torque: 10.0 Nm.

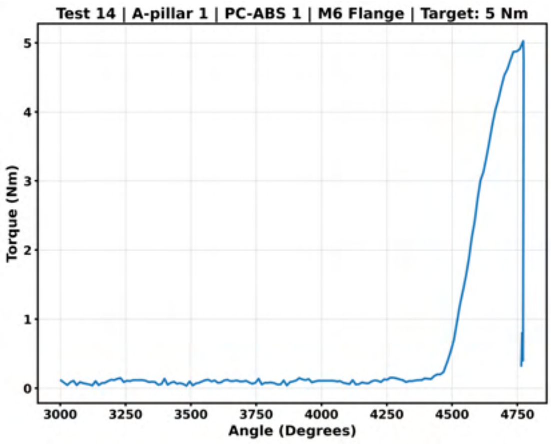

(a) Torque vs. Time plot.

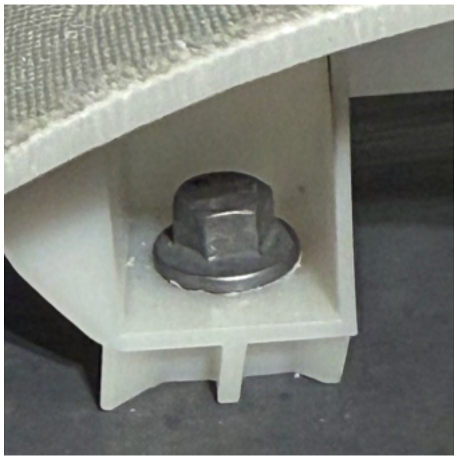

(b) Close-up of physical joint.

Figure 4.31: Test 14: PC-ABS 1 (A-pillar 1), M6 screw without washer. Target torque: 5.0 Nm.

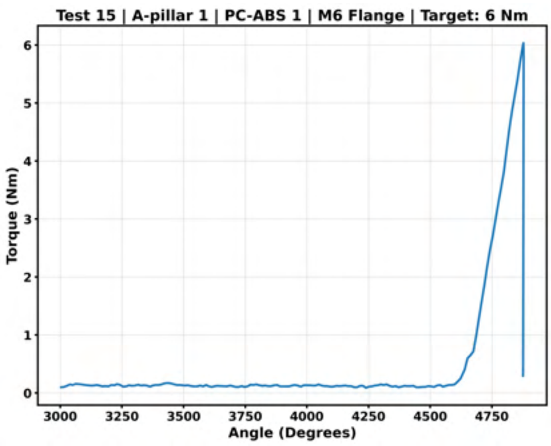

(a) Torque vs. Time plot.

(b) Close-up of physical joint.

Figure 4.32: Test 15: PC-ABS 1 (A-pillar 1), M6 screw without washer. Target torque: 6.0 Nm.

Tests 12, 14, and 15 prove the A-pillar 1 component handles flange screw torques of 4.5, 5.0, and 6.0 Nm perfectly. Zero visible deformation occurs. Test 13 targeted 10.0 Nm. The torque plot flags deformation initiation around 5.0 Nm. The maximum torque reaches 7.0 Nm. The screw then punches completely through the material and terminates the test.

PC-ABS 2 (A-pillar 2)

Tests 21, 22, and 23 evaluated an M6 flange screw without a washer.

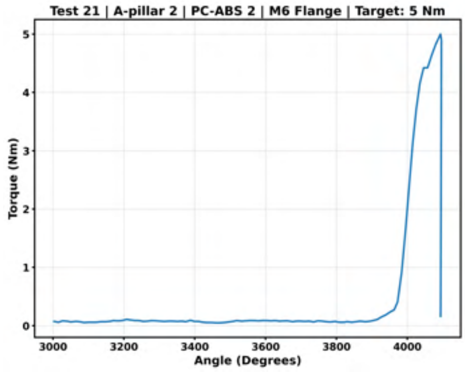

(a) Torque vs. Time plot.

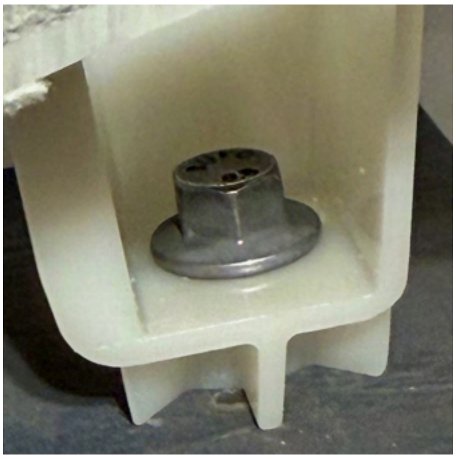

(b) Close-up of physical joint.

Figure 4.33: Test 21: PC-ABS 2 (A-pillar 2), M6 screw without washer. Target torque: 5.0 Nm.

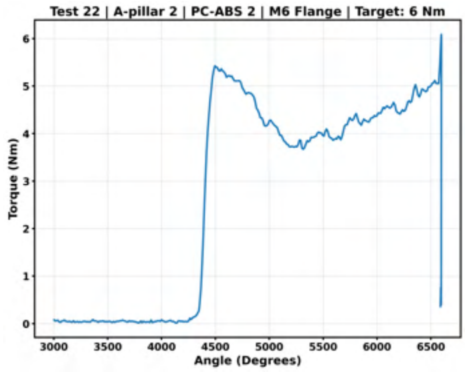

(a) Torque vs. Time plot.

(b) Close-up of physical joint.

Figure 4.34: Test 22: PC-ABS 2 (A-pillar 2), M6 screw without washer. Target torque: 6.0 Nm.

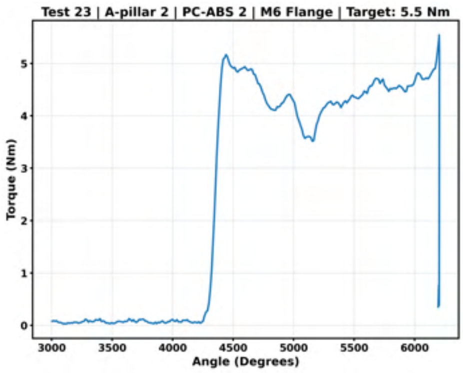

(a) Torque vs. Time plot.

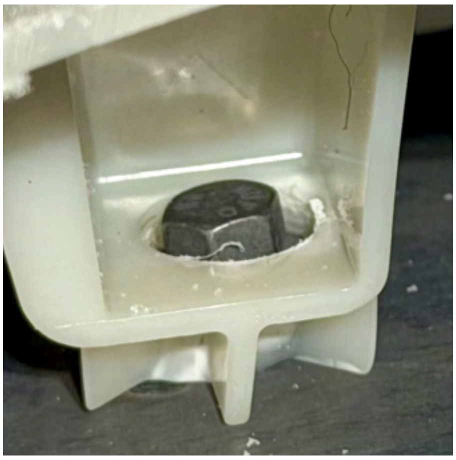

(b) Close-up of physical joint.

Figure 4.35: Test 23: PC-ABS 2 (A-pillar 2), M6 screw without washer. Target torque: 5.5 Nm.

Tests 21, 22, and 23 evaluated the A-pillar 2 doghouse structure against 5.0, 6.0, and 5.5 Nm targets. Test 21 passes cleanly with zero visible deformation. The 5.5 Nm and 6.0 Nm tests both fail. The screw completely breaches the material. Both failure plots map deformation initiation at exactly 5.1 to 5.2 Nm.

Comparison of PC-ABS Grades (PC-ABS 1 vs. PC-ABS 2)

PC-ABS 1 provides higher torque capacity. It safely sustains an applied 6.0 Nm load. PC-ABS 2 hits a hard structural limit at 5.0 Nm.

4.3.2.3 PP

PP-T 2 (IC-ramp 1)

Tests 17, 18, and 19 evaluated an M6 flange screw without a washer.

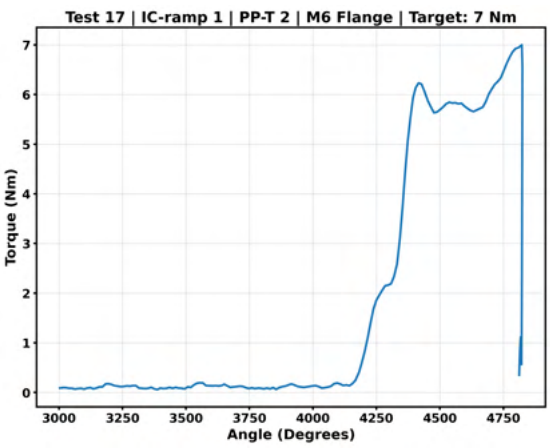

(a) Torque vs. Time plot.

(b) Close-up of physical joint.

Figure 4.36: Test 17: PP-T 2 (IC-ramp 1), M6 screw without washer. Target torque: 7.0 Nm.

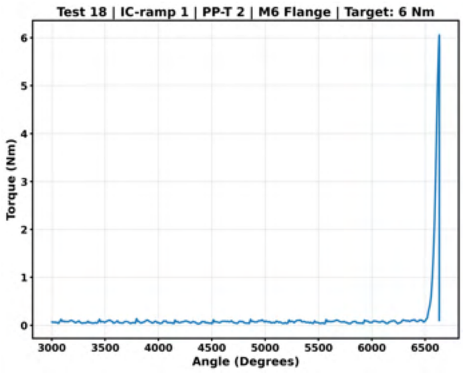

(a) Torque vs. Time plot.

(b) Close-up of physical joint.

Figure 4.37: Test 18: PP-T 2 (IC-ramp 1), M6 screw without washer. Target torque: 6.0 Nm.

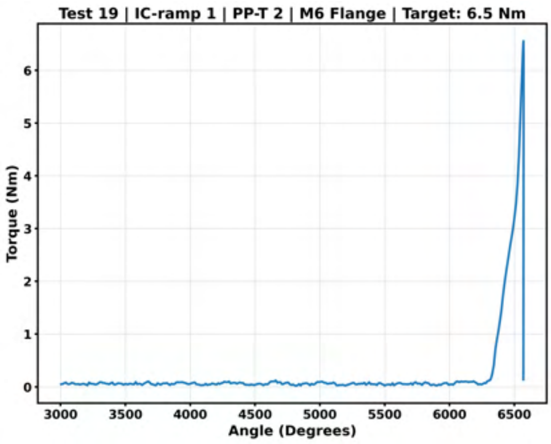

(a) Torque vs. Time plot.

(b) Close-up of physical joint.

Figure 4.38: Test 19: PP-T 2 (IC-ramp 1), M6 screw without washer. Target torque: 6.5 Nm.

Tests 17, 18, and 19 targeted 7.0, 6.0, and 6.5 Nm loads. Test 17 displays obvious visual deformation in the close-up. The torque plot corroborates this physical damage, logging initial deformation around 6.2 Nm. Tests 18 and 19 both pass with zero visible deformation. The clean result of Test 19 at 6.5 Nm slightly contradicts the 6.2 Nm yield point captured during Test 17.

Tests 16 and 20 evaluated an M6 screw equipped with a captive washer.

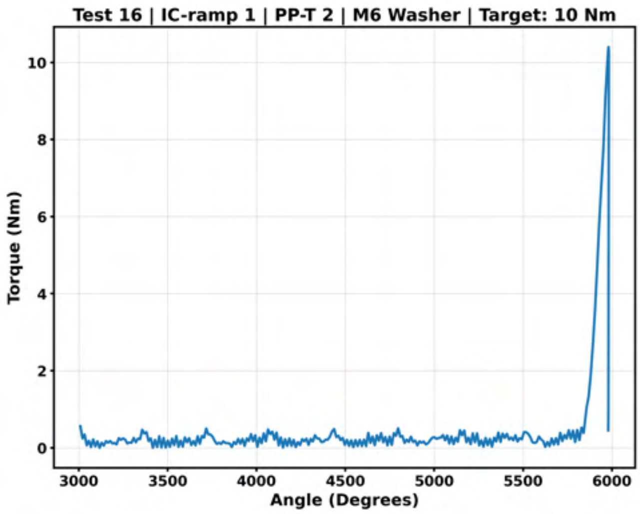

(a) Torque vs. Time plot.

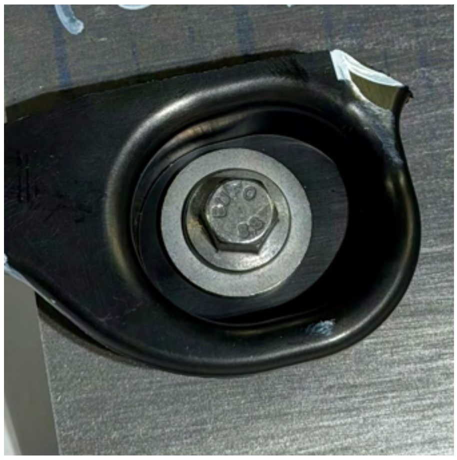

(b) Close-up of physical joint.

Figure 4.39: Test 16: PP-T 2 (IC-ramp 1), M6 screw with washer. Target torque: 10.0 Nm.

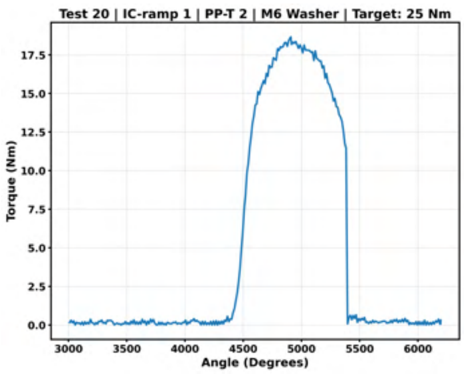

(a) Torque vs. Time plot.

(b) Close-up of physical joint.

Figure 4.40: Test 20: PP-T 2 (IC-ramp 1), M6 screw with washer. Target torque: 25.0 Nm.

Tests 16 and 20 targeted extreme 10.0 and 25.0 Nm loads. Test 16 returned acceptable results completely free of visual deformation. This proves the washer dynamically increases the absolute load-bearing capability. The fastener in Test 20 suffered a massive torsional fracture at approximately 18.0 Nm. The close-up picture clearly highlights the intense localized deformation generated at this extreme torque level right before the fastener snapped.

4.3.2.4 PP-GF

PP-GF 1 (IC-ramp 2)

Test 24 evaluated an M6 screw equipped with a captive washer.

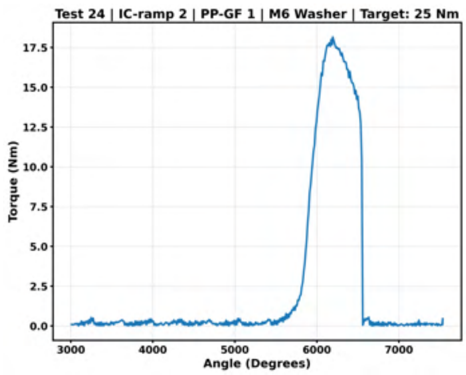

(a) Torque vs. Time plot.

(b) Close-up of physical joint.

Figure 4.41: Test 24: PP-GF 1 (IC-ramp 2), M6 screw with washer. Target torque: 25.0 Nm.

Test 24 targeted a massive 25.0 Nm load. The solid steel fastener fractured near 18.0 Nm. The physical inspection reveals incredible structural stability. The PP-GF material shows minimal deformation despite the total fastener failure.

4.3.2.5 Summary of Torque Capacity Results

The captive washer delivers a massive, definitive structural advantage throughout all physical testing. Every single component tested with a washer achieved a dramatic increase in ultimate torque capacity. The material grade, underlying doghouse design, internal rib structure, and clearance hole geometry did not matter. Introducing a washer universally elevated the structural limits beyond 15.0 Nm. All washer-equipped configurations effortlessly passed the strict 10.0 Nm Volvo internal standard. They did so without triggering any macroscopic yielding or failure. Standard flange screws consistently failed to reach this structural threshold. The narrow flange heads routinely caused severe material penetration between 4.0 Nm and 7.0 Nm.

Table 4.12 compiles the exhaustive physical joint data. It presents the exact target torques, specific hardware configurations, and ultimate physical outcomes across all tested components.

Table 4.12: Comprehensive summary of physical torque testing outcomes highlighting the structural benefits of captive washers.

Test	Component (ID)	Material Designation	Screw Type	Target (Nm)	Status / Result
1	Belt guide 2	ABS 2	Flange	5.0	NOK (Failed at 3.8:4.0 Nm)
3	Belt guide 2	ABS 2	Flange	4.5	NOK (Failed at 3.8:4.0 Nm)
5	Belt guide 2	ABS 2	Flange	3.0	OK
2	Belt guide 2	ABS 2	Washer	5.0	OK
4	Belt guide 2	ABS 2	Washer	6.0	OK
6	Belt guide 2	ABS 2	Washer	10.0	OK
7	Belt guide 1	ABS 2	Flange	4.5	OK
9	Belt guide 1	ABS 2	Flange	6.0	NOK (Failed at 4.8:4.9 Nm)
10	Belt guide 1	ABS 2	Flange	5.0	OK
8	Belt guide 1	ABS 2	Washer	15.0	OK (Yield initiated at 12.5 Nm)
11	Belt guide 1	ABS 2	Washer	25.0	NOK (Fastener shear at 17.0 Nm)
12	A-pillar 1	PC-ABS 1	Flange	4.5	OK
14	A-pillar 1	PC-ABS 1	Flange	5.0	OK
15	A-pillar 1	PC-ABS 1	Flange	6.0	OK
13	A-pillar 1	PC-ABS 1	Flange	10.0	NOK (Failed at 7.0 Nm)
21	A-pillar 2	PC-ABS 2	Flange	5.0	OK
23	A-pillar 2	PC-ABS 2	Flange	5.5	NOK (Failed at 5.1 Nm)
22	A-pillar 2	PC-ABS 2	Flange	6.0	NOK (Failed at 5.1 Nm)
18	IC-ramp 1	PP-T 2	Flange	6.0	OK
19	IC-ramp 1	PP-T 2	Flange	6.5	OK
17	IC-ramp 1	PP-T 2	Flange	7.0	NOK (Failed at 6.2 Nm)
16	IC-ramp 1	PP-T 2	Washer	10.0	OK
20	IC-ramp 1	PP-T 2	Washer	25.0	NOK (Fastener shear at 18.0 Nm)
24	IC-ramp 2	PP-GF 1	Washer	25.0	OK (Fastener shear at 18.0 Nm)

4.3.2.6 Influence of Clearance Hole Sizing and Geometry

The tested components predominantly featured circular and oval clearance hole designs. The specific geometry varied heavily among the oval designs. Some featured tight corner radii. Others used much larger radii. This created a highly elongated opening and severely reduced the available contact surface.

Figure 4.42 illustrates the primary hole variations observed across the tested production parts.

(a) Circular hole. **(b)** Oval (small radii). **(c)** Oval (large radii).

Figure 4.42: Comparison of the characteristic clearance hole geometries present in the tested thermoplastic components.

Contact continuity operates as the absolute dominant factor in generating high clamp retention. The empirical results confirm a hard engineering rule. Minimizing the clearance hole size directly increases structural capacity.

Small circular geometries heavily outperform elongated oval or rectangular shapes. This physical observation perfectly matches the specific trends identified in the finite element method (FEM) simulations. Small, circular clearance holes distribute contact pressure smoothly and evenly. They drastically drop localized deformation and allow the joint to withstand massive torque loads.

The physical evaluation of the IC-ramp 1 geometry explicitly isolates this structural reliance on available bearing area. The PP-T 2 matrix possesses a severely lower inherent structural stiffness compared to the ABS and PC-ABS grades. Despite this material weakness, the IC-ramp 1 recorded the highest absolute load capacity of all flange screw evaluations. The PP-T 2 component safely sustained a 7.0 Nm flange screw load without any macroscopic failure.

Its specific fastening interface generates this elevated physical capacity. It features a minimized 8.0 mm circular clearance hole. This hole pairs perfectly with a completely flat rear bearing surface entirely free of internal ribs. The continuous annular contact of the circular hole combines directly with the uniform structural support of the flat rear side. This geometric pairing mechanically compensates for the weak bulk material stiffness of the PP-T 2 matrix.

Figure 4.43 details the structural configuration of the IC-ramp 1 fastening interface.

(a) Front interface featuring an 8.0 mm circular clearance hole.

(b) Rear bearing surface featuring a flat, continuous profile without internal ribs.

Figure 4.43: Geometric configuration of the IC-ramp 1 fastening interface.

Ensuring a minimized, circular clearance hole represents an absolute design requirement. It maximizes exact load capacity and aggressively prevents premature localized yielding under concentrated flange screw loads.

5
Discussion

This chapter evaluates the integrated findings from computational optimization, nonlinear finite element simulations, and physical experiments. The text defines the specific physical mechanisms governing thermoplastic joint stability. It addresses methodological limitations. It concludes with a direct engineering assessment regarding the elimination of metallic compression limiters across future vehicle architectures.

5.1 Bridging Design and Standard Engineering

Eliminating metallic compression limiters creates a fundamental conflict between theoretical design guidelines and practical assembly requirements. The experimental results confirmed an absolute engineering reality: optimized captive washers allow direct plastic fastening to safely achieve a standard 10 Nm tightening torque. The target torque was reached, and the joint survived without immediate catastrophic damage.

This physical success exposes a severe corporate engineering dilemma: Achieving the standard assembly torque directly on bare plastic perfectly satisfies managerial cost and recyclability demands, yet executing this design explicitly violates established legacy safety standards. Corporate fastening guidelines strictly advise against applying high metallic torque levels directly to softer polymer interfaces without inserts. The underlying physical mechanics proven in this study directly contradict the conservative theoretical limits set by traditional bolted joint standards.

By generating hard empirical data, this thesis actively forced a direct dialogue between the design team and the standard engineering department. This is the absolute primary value of the investigation. Both sides have now convened to discuss this gap issue using verified mechanical facts rather than theoretical assumptions. A mutual understanding now exists regarding the absolute structural capabilities of optimized polymer joints.

Reconciling this gap requires a massive shift in how automotive organizations classify thermoplastic joints. Standard engineering guidelines must evolve to recognize contact pressure redistribution as a valid structural strategy. The ongoing cross-departmental discussions present massive future possibilities, primarily the potential drafting of a completely new fastening standard. If standard engineering formally accepts these optimized geometries as structurally sound, this insert-free strategy can cascade across multiple other departments at Volvo Cars. Removing metal inserts globally across the vehicle architecture will unlock exponential financial savings and drastically elevate corporate sustainability and recyclability metrics.

5.2 The Dominance of Contact Area Geometry

The effective bearing contact area dictates joint stability entirely. This parameter dominated the design of experiments (DOE), finite element analyses, and physical testing. Thermoplastic polymers possess inherently low compressive stiffness and yield limits. Maximizing the contact area prevents localized stress from exceeding the structural capacity of the material under standard automotive assembly torques.

The physical torque capacity tests explicitly demonstrated this behaviour. Assemblies successfully withstood the 10 Nm target torque without visible macroscopic deformation when fitted with captive washers. Exploratory tests pushed washer-supported joints to 15 Nm while maintaining absolute structural integrity. Fastener fracture eventually occurred at approximately 18 Nm during destructive testing. The PP-GF materials exhibited minimal deformation under these ultimate loads. Softer PP and ABS grades yielded. They successfully avoided the complete punch-through failure modes observed with standard flange screws at merely 4 to 6 Nm. The expanded contact area of the washer shifts the physical failure mode completely. It transitions from localized surface penetration to bulk material compression.

5.2.1 Case Study: Clearance Hole Geometry and Interface Flatness

The physical evaluation of the IC-ramp components isolated the exact relationship between contact area and joint stability. The tested IC-ramp component consisted of PP-T 2. This specific material grade consistently demonstrated the lowest structural stiffness and highest deformation vulnerability across all numerical evaluations.

The physical PP-T 2 IC-ramp component successfully passed the 10 Nm load with a captive washer despite this severe material compliance. It even supported 6.5 Nm without a washer. Analyzing this unexpected physical performance identified two distinct geometric features on this specific production part. It featured a minimized circular clearance hole. It also possessed a completely flat rear support surface.

This physical observation heavily supports the finite element clearance hole evaluations mapped in Section 4.2.1.4. Numerical simulations proved that transitioning the baseline IC-ramp component from an oval hole to a modified circular hole reduced deformation within the PP-T 2 material from 2.29 mm down to 0.21 mm. This represents a massive 91% reduction in macroscopic displacement achieved purely through geometric optimization.

This raises a critical engineering question. Did the small circular hole or the flat rear support surface contribute more to the structural stability of the physical component? Component availability limitations restricted the physical investigation to the specific A-pillar and IC-ramp CAD variants provided. Additional physical testing could not exhaustively isolate this specific interaction between a flat rear surface, a small hole, and a highly compliant material. The combined physical and numerical data delivers a conclusive verdict regardless. Optimizing the clearance geometry to maximize continuous bearing area allows even the weakest polymer matrices to withstand elevated assembly torques safely.

5.2.2 Influence of Surface Graining on Friction Behaviour

Surface texture directly manipulates friction mechanics. The experimental phase compared grained and ungrained surfaces on PP test strips. The results indicated no measurable difference in the bearing friction coefficient between the two surface conditions.

High localized contact pressure drives this physical response. The PP material yields instantly during assembly. The rotating steel screw head polishes and flattens the surface graining as it tightens. This crushing action rapidly erases all initial textural differences.

A stiffer matrix alters this behaviour entirely. Materials possessing higher surface hardness and yield strength, such as PC-ABS or PP-GF grades, heavily resist this physical polishing effect. Preserving the surface texture under heavy load effectively increases the bearing friction coefficient of the entire joint.

Manipulating this surface friction provides a powerful engineering tool. Intentionally increasing bearing friction through durable surface graining demands a higher assembly torque to generate the exact same axial clamping force. This physical relationship establishes a hidden structural safety buffer. The joint safely reaches much higher target torques. This satisfies strict internal automotive assembly standards without generating excessive clamping forces. It physically prevents the overload conditions that destroy the plastic screw boss.

5.3 Methodological Limitations

Certain methodological constraints restrict the absolute scope of this investigation. The limited statistical sample size available during the physical testing campaign acts as a primary limitation.

The friction coefficient evaluations relied on singular tests for each specific configuration. Friction reacts violently to minor tribological variations. A professional technician wearing gloves conducted the testing. Microscopic surface contamination, such as residual manufacturing oils or handling transfer, cannot be entirely prevented.

This introduces potential variance into the calculated thread and bearing friction coefficients driving the analytical models.

Component availability restricted the experimental matrix during the physical torque capacity testing. The necessity of testing available production parts hindered direct material comparisons. The available A-pillar components consisted of two different PC-ABS grades. The IC-ramp components featured fundamentally different macro-geometries and entirely different material classes (PP versus PP-GF). This provided a broad spectrum of geometric assembly data. A larger inventory of identical geometries molded in varying materials would have enabled stricter statistical isolation of specific material performance parameters.

5.4 Future Work

As explicitly stated in the initial delimitations (Section 1.4), the original project scope intended to capture a massive spectrum of variables. Strict project timeframes restricted the final execution. The following intended investigations must therefore transition directly into future work.

Several research avenues must address the existing limitations and refine the predictive frameworks. Future investigations must prioritize massive experimental sample sizes across uniform test geometries. This establishes absolute statistical confidence in the tribological and structural behaviour.

The physical testing campaign demands dynamic and environmental evaluation. Subjecting the washer-supported thermoplastic assemblies to thermal cycling, extended physical creep testing, and severe vibration profiles is absolutely critical. This provides the necessary physical validation to back up the 1000-hour numerical retention models.

Specific material data significantly improves the accuracy and predictive capabilities of the finite element and computational optimization models. Extracting non-linear creep data directly from dedicated physical component tests heavily enhances the fidelity of the numerical predictions. Standardized supplier material cards often lack this highly specialized nonlinear data.

Future optimization frameworks must integrate component economics. The current computational methodology evaluated materials strictly based on structural performance and preload retention. Adding cost into the optimization equation changes everything. A lower-performing, inexpensive PP material equipped with a captive washer represents a highly cost-effective solution compared to a premium PC-ABS material engineered to survive without a washer. Factoring piece price, material volume, and hardware costs into the objective functions establishes a comprehensive engineering metric. This financial integration will likely flip the recommended material rankings entirely for high-volume automotive applications.

Finally, mapping the exact procedure to safely implement these findings across a global automotive organization represents a massive undertaking. Validating this entirely new standard framework and proving to the standard engineering board exactly how to classify, test, and approve insert-free joints is easily large enough to constitute an independent Master's thesis on its own.

6
Conclusion

This thesis establishes the exact mechanical and organizational frameworks required to safely eliminate metallic compression limiters from automotive thermoplastic assemblies. Through an integrated execution of computational optimization, surrogate modelling, nonlinear finite element analysis, and physical validation testing, the research provides a definitive understanding of the physics governing insert-free polymer fastening.

Technical

The findings demonstrate that joint stability and preload retention depend fundamentally on fastening interface geometry rather than bulk material stiffness alone. Across all design of experiments matrices, finite element simulations, and destructive torque-to-failure testing, a clear physical law emerged. Increasing the effective bearing area through optimized captive washers significantly mitigates localized contact pressure, stabilizes load distribution, and maximizes structural capacity. Minimizing clearance hole dimensions and maximizing flat bearing interfaces act as mandatory geometric constraints to restrict viscoelastic material flow. When supported by these precise geometric parameters, the bare thermoplastic assemblies safely withstand the rigid Volvo Cars assembly target of 10 Nm without inducing macroscopic deformation or catastrophic yield.

Engineering Infrastructure

The implications of this work extend far beyond structural physics, directly transforming the corporate engineering infrastructure. Achieving high metallic torque levels on bare polymer joints requires a complete re-evaluation of long-standing design practices, validation methodologies, and risk assessment assumptions. By introducing hard empirical facts and predictive models into a historically conservative domain, this thesis successfully bridges the critical operational gap between interior design engineers and standard engineering boards. Proposing verified geometric alternatives to legacy metal components has initiated a direct, fact-based cooperation between departments that previously operated under conflicting mandates.

Overall

The overall conclusion is absolute. Insert-free thermoplastic joints easily satisfy the 10 Nm fastening requirement when supported by optimized fastening geometry. This thesis provides the exact scientific framework required for corporate boards to safely transition away from rigid, blanket insert requirements. This establishes a permanent, data-driven pathway for future standardization, unlocking massive cost reductions, weight optimization, and enhanced vehicle recyclability across future automotive platforms.

Bibliography

[1] Ashby, M. F., Shercliff, H., Cebon, D. (2018). *Materials: Engineering, Science, Processing and Design* (4th ed.). Butterworth-Heinemann.

[2] Dassault Systèmes. (2022). *Abaqus Analysis User's Guide*. Dassault Systèmes Simulia Corp.

[3] EWI. *Polymer Creep and Stress Relaxation Analysis*. Available at: https://ewi.org/polymer-creep-and-stress-relaxation-in-medtech-devices/

[4] Evertsson, M., Mägi, M., Melkersson, K. (2017). *Maskinelement* (1st ed.). Studentlitteratur.

[5] Gokhale, N. S., Deshpande, S. S., Bedekar, S. V., Thite, A. N. (2008). *Practical Finite Element Analysis*. Finite to Infinite.

[6] Gustaver, M. (2020). *A Chalmers University of Technology Master's thesis template for LaTeX*. Unpublished.

[7] ISO 898-1:2013. *Mechanical properties of fasteners made of carbon steel and alloy steel, Part 1: Bolts, screws and studs with specified property classes*. International Organization for Standardization.

[8] ISO 16047:2005. *Fasteners, Torque/clamp force testing*. International Organization for Standardization.

[9] International Organization for Standardization. (2013). *ISO 898-1:2013 Mechanical properties of fasteners made of carbon steel and alloy steel - Part 1: Bolts, screws and studs with specified property classes - Coarse thread and fine pitch thread*. Geneva, Switzerland: ISO.

[10] Pedregosa, F., et al. (2011). Scikit-learn: Machine Learning in Python. *Journal of Machine Learning Research*, 12, 2825-2830.

[11] Blank, J., Deb, K. (2020). Pymoo: Multi-objective Optimization in Python. *IEEE Access*, 8, 89497-89509.

[12] Svenska Nätverket för Skruvförband (SFN). *Handbok*.

[13] Sherex Fastening Solutions. *What are Compression Limiters?* Available at: https://www.sherex.com/blog/what-are-compression-limiters/

[14] Spirol International Corporation. *How to Maintain Joint Integrity When Converting from Metal to Plastic*. Available at: https://uk.spirol.com/assets/files/ins-wp-how-to-maintain-joint-integrity-when-converting-from-metal-to-plastic-us.pdf

[15] Van Rossum, G., Drake, F. L. (2009). *Python 3 Reference Manual*. CreateSpace.

[16] VDI-Gesellschaft Produkt- und Prozessgestaltung. (2015). *VDI 2230 Part 1: Systematic Calculation of High Duty Bolted Joints: Joints with One Cylindrical Bolt*. Verein Deutscher Ingenieure.

[17] Wikipedia contributors. (n.d.). *Arrhenius equation*. Wikipedia, The Free Encyclopedia. Retrieved from https://en.wikipedia.org/wiki/Arrhenius$_equation$

[18] Wikipedia contributors. (n.d.). *Constitutive equation*. Wikipedia, The Free Encyclopedia. Retrieved from https://en.wikipedia.org/wiki/Constitutive$_equation$

[19] Wikipedia contributors. (n.d.). *Creep (deformation)*. Wikipedia, The Free Encyclopedia. Retrieved from https://en.wikipedia.org/wiki/Creep$_(deformation)$

[20] Wikipedia contributors. (n.d.). *Crystallinity*. Wikipedia, The Free Encyclopedia. Retrieved from https://en.wikipedia.org/wiki/Crystallinity

[21] Wikipedia contributors. (2026). *Hooke's law*. Wikipedia, The Free Encyclopedia. Available at: `https://en.wikipedia.org/wiki/Hooke%27s_law` (Accessed: 9 June 2026).

[22] Wikipedia contributors. (n.d.). *Viscoelasticity*. Wikipedia, The Free Encyclopedia. Retrieved from https://en.wikipedia.org/wiki/Viscoelasticity

[23] Wriggers, P. (2006). *Computational Contact Mechanics* (2nd ed.). Springer.

[24] Zienkiewicz, O. C., Taylor, R. L., Zhu, J. Z. (2005). *The Finite Element Method: Its Basis and Fundamentals* (6th ed.). Butterworth-Heinemann.

A
Appendix A

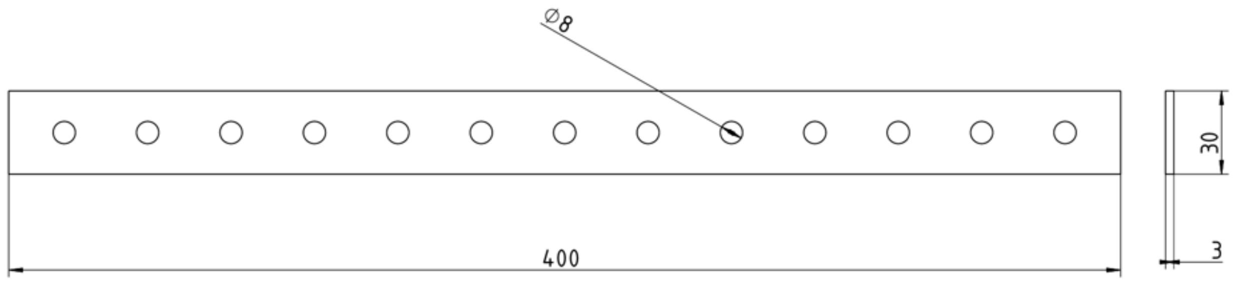

Figure A.1: Plastic strip CAD design

Quantity	Part Number
1	Steelplate
4	M6 Weldnut

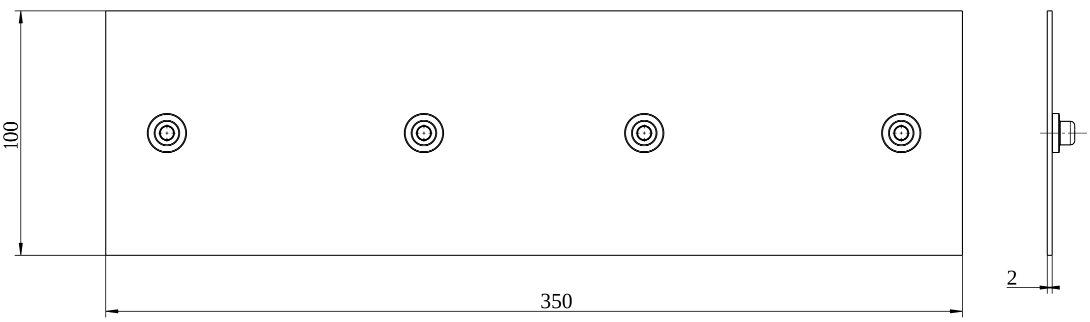

Figure A.2: Custom made steel plate with 4 M6 welding nuts

DEPARTMENT OF INDUSTRY AND MATERIALS SCIENCE
CHALMERS UNIVERSITY OF TECHNOLOGY
Gothenburg, Sweden
www.chalmers.se

CHALMERS
UNIVERSITY OF TECHNOLOGY